**UNIVERSITY OF IOANNINA**
**SCHOOL OF HEALTH SCIENCES**
**FACULTY OF MEDICINE**

SECTOR OF SURGERY
CARDIOVASCULAR SURGERY DEPARTMENT

# NUMERICAL SIMULATIONS OF BLOOD FLOW EFFECTS UNDER THE PRESENCE OF ABDOMINAL AORTIC ANEURYSM

**ANASTASIOS A. RAPTIS**
MECHANICAL ENGINEER

PhD THESIS

**IOANNINA 2016**

**UNIVERSITY OF IOANNINA**
**SCHOOL OF HEALTH SCIENCES**
**FACULTY OF MEDICINE**

SECTOR OF SURGERY
CARDIOVASCULAR SURGERY DEPARTMENT

# NUMERICAL SIMULATIONS OF BLOOD FLOW EFFECTS UNDER THE PRESENCE OF ABDOMINAL AORTIC ANEURYSM

**ANASTASIOS A. RAPTIS**
MECHANICAL ENGINEER

PhD THESIS

**IOANNINA 2016**

«Η έγκριση της διδακτορικής διατριβής από το Τμήμα Ιατρικής του Πανεπιστημίου Ιωαννίνων δεν υποδηλώνει αποδοχή των γνωμών του συγγραφέα. Ν.5343/32, άρθρο 202, παράγραφος 2 (νομική κατοχύρωση του Ιατρικού Τμήματος)».

**Ημερομηνία αίτησης του κ. Ράπτη Αναστασίου**: 21-3-2012

**Ημερομηνία ορισμού Τριμελούς Συμβουλευτικής Επιτροπής**: 733α/3-4-2012

**Μέλη Τριμελούς Συμβουλευτικής Επιτροπής**:

Επιβλέπων

Ματσάγκας Μιλτιάδης, Αναπληρωτής Καθηγητής Αγγειοχειρουργικής

Μέλη

Ματίκας Θεόδωρος, Καθηγητής Μηχανικών Επιστήμης Υλικών Παν/μιο Ιωαννίνων

Ξένος Μιχαήλ, Επίκουρος Καθηγητής Τμήματος Μαθηματικών, Τομέας Εφαρμοσμένων Μαθηματικών και Μηχανικής Έρευνας, Παν/μιο Ιωαννίνων

**Ανασύσταση Τριμελούς Συμβουλευτικής Επιτροπής:** Αριθμ Συνεδρ. 788α/31-5-2016

Επιβλέπων

Αποστολάκης Ευστράτιος, Καθηγητής Καρδιοχειρουργικής

Μέλη

Ματσάγκας Μιλτιάδης, Καθηγητής Αγγειοχειρουργικής του Τμήματος Ιατρικής του Παν/μίου Θεσσαλίας

Ξένος Μιχαήλ Επίκουρος Καθηγητής του Τμήματος Μαθηματικών του Παν/μίου Ιωαννίνων

**Ημερομηνία ορισμού θέματος**: 2-5-2012

*«Προσομοίωση και αριθμητική επίλυση της αιματικής ροής και των επιδράσεων της με την παρουσία ανευρύσματος στην κοιλιακή αορτή»*

**ΟΡΙΣΜΟΣ ΕΠΤΑΜΕΛΟΥΣ ΕΞΕΤΑΣΤΙΚΗΣ ΕΠΙΤΡΟΠΗΣ : 790α/1-7-2016**

1. Αποστολάκης Ευστράτιος, Καθηγητής Καρδιοχειρουργικής, του Τμήματος Ιατρικής του Παν/μίου Ιωαννίνων
2. Γουδέβενος Ιωάννης, Καθηγητής Παθολογίας-Καρδιολογίας, του Τμήματος Ιατρικής του Παν/μίου Ιωαννίνων
3. Ματσάγκας Μιλτιάδης, Καθηγητής Αγγειοχειρουργικής, του Τμήματος Ιατρικής του Παν/μίου Θεσσαλίας
4. Παπαδόπουλος Γεώργιος Καθηγητής Αναισθησιολογίας του Τμήματος Ιατρικής του Παν/μίου Ιωαννίνων
5. Συμινελάκης Σταύρος Αναπληρωτής Καθηγητής Καρδιοχειρουργικής, του Τμήματος Ιατρικής του Παν/μίου Ιωαννίνων
6. Αρναούτογλου Ελένη Αναπληρώτρια Καθηγήτρια Αναισθησιολογίας του Τμήματος Ιατρικής του Παν/μίου Ιωαννίνων

7. Ξένος Μιχαήλ, Επίκουρος Καθηγητής Τμήματος Μαθηματικών, Τομέας Εφαρμοσμένων Μαθηματικών και Μηχανικής Έρευνας, Παν/μιο Ιωαννίνων

Έγκριση Διδακτορικής Διατριβής με βαθμό **«ΑΡΙΣΤΑ»** στις **4-7-2016**

**ΠΡΟΕΔΡΟΣ ΤΟΥ ΤΜΗΜΑΤΟΣ ΙΑΤΡΙΚΗΣ**
**Πασχόπουλος Μηνάς**
Καθηγητής Μαιευτικής-Γυναικολογίας

**Η Γραμματέας του Τμήματος**
ΚΑΠΠΟΠΟΥΛΟΥ ΜΑΡΙΑ

***To my parents…***

*Without the inspiration, drive and support you gave me, I would not be the person I am today*

***To my teachers…***

*You have opened my eyes to a whole new world*

*My appreciation is beyond expression*

**Acknowledgements**

Firstly, I would like to express my sincere gratitude to my supervisor Professor Miltiadis Matsagkas for indicating the subject of the thesis and offering continuous support. His dedication to research inspired me values that will accompany the rest of my course. It is an honor to have made the first scientific steps alongside an inspirational Professor like him.

I am also extremely grateful for the assistance of Professor Efstratios Apostolakis, who supported me in the last stages of the thesis. We collaborated for a small period of time and it would be my honor if our collaboration was continued in the future.

Besides my advisors, I would like to thank the rest of the thesis committee and especially Assistant Professor Michalis Xenos. He shared his knowledge and experience and encouraged me in difficult occasions. He was always open to hear and discuss my concerns and his valuable advice will be a compass for me in the future.

The thesis would not be completed without the support of the Institute of Vascular Diseases. I would like to thank all of its members and especially its President, Professor Athanasios Giannoukas, for his willingness to invest in my research. It was highly motivating to be part of an institute that has vision of the future, playing leading role in the research of vascular diseases.

Last but not least, I would like to thank the Department of Mathematics, University of Ioannina, that provided the necessary room and resources to conclude my research and embraced me in its everyday life.

# TABLE OF CONTENTS

# INTRODUCTION

## Abdominal Aortic Aneurysms

### *Definition*

Abdominal aortic aneurysms (AAAs) are defined as a localized dilatation of the abdominal aorta featuring diameter at least 50% larger than the normal one. We accept "normal" diameter to be approximately 20mm, and therefore an abdominal aorta wider than 30mm, is labeled as aneurysmal. In practical terms, "normal" diameter refers to the non-aneurysmal adjacent abdominal aortic segment.[1] The dilatation involves all the layers of the arterial wall, e.g. intima, media and adventitia.

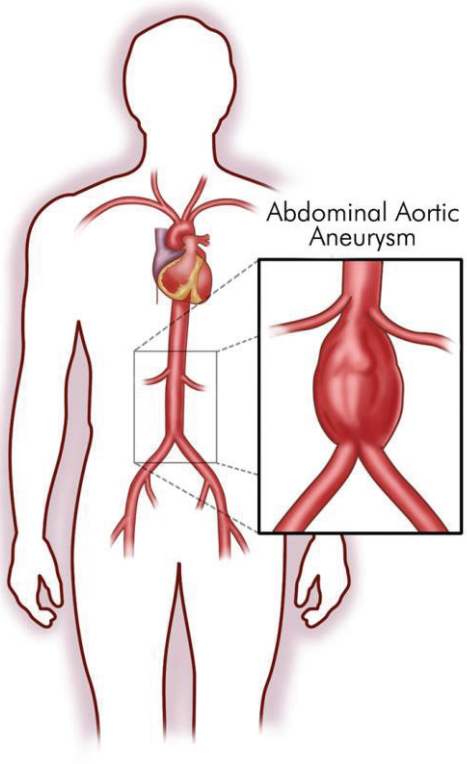


*Figure 1. Infrarenal abdominal aortic aneurysm.*

### *Prevalence*

According to population screening studies, the prevalence of AAA increases with age, occurring in 7–8% of men over 65 years.[2,3] The AAA is typically a disease of the male population, with six times higher prevalence in men than in women.[4] In a more general sense, 5% of the over-60 population will have an AAA, and at the age of 67, a man is ten times more likely to die from a ruptured AAA than a woman. Recent data suggest that the incidence of AAAs is declining. Between 1997 and 2009, there has been a reduction in age-adjusted mortality from 40.4 to 25.7 per 100.000 population in England and from 30.1 to 20.8 per 100.000 population in Scotland.[5]

### *Pathogenesis*

Despite extensive research, the exact mechanisms underlying aneurysm pathogenesis remain unclear. It appears that the process is multifactorial, involving biochemistry, immunological, mechanical, and genetic components of variable importance.[6] Much of our understanding

derives from the work performed on the abdominal aorta, and it is assumed that non-aortic aneurysmal disease results from a similar pathological sequence of events.

The aneurysmal disease ultimately results following gradual proteolytic degradation of arterial vessel walls. The structural integrity of arterial wall is dependent on adequate functional connective tissue elements including elastin and collagen. Loss of these elements weakens the vessel wall and thus predisposes to aneurysm formation. Research into AAAs has discovered locally increased levels of matrix metalloproteinases (MMPs) that result in this observed connective tissue breakdown. Four MMP subtypes are thought to be of importance in this process: gelatinases (MMP-2 and MMP-9), matrilysin (MMP-7), and macrophage elastase (MMP-12). In addition to this increased local expression, altered levels of circulating proteases may play a role, and research continues into the contributions to aneurysmal disease from various plasminogen activators, serine elastases, and cysteine proteases (cathepsins S and K). Abnormally low levels of protease inhibitors are suggested to exert the same pathogenic effects, and this has also been the focus of much recent work. Preliminary research into the most abundant serine protease inhibitor cystatin c has confirmed that in patients with aneurysmal disease corresponding levels of this protein are indeed lower than normal.[1]

Chronic inflammation plays a significant role in aneurysmal disease. Much of the vessel wall destruction is undoubtedly mediated by the inflammatory infiltrate composed of T cells, macrophages, B lymphocytes, and plasma cells, but the antecedent trigger for this cellular migration remains unclear. It has been suggested that aneurysmal disease is, in fact, an antigen-driven immune disease. Proposed antigenic activators to subsequent inflammation include elastin, interstitial collagen, oxidized low-density lipoprotein, cytomegalovirus, and artery-specific antigenic proteins such as AAAP-40. Following T-cell antigen recognition, the inflammatory cascade begins, ultimately resulting in vessel wall degradation and progression to aneurysmal disease.[1]

Arterial wall biomechanical stress is also accepted as being of considerable importance in both aneurysm progression and rupture. Model analysis of wall stress variation in different anatomical locations implies that altered hemodynamic profiles may explain the varying susceptibility of an arterial wall to become aneurysmal (e.g., increased disease incidence in abdominal as opposed to the thoracic aorta). It is suggested that mechanical failure from excessive stress initiates and promotes aneurysmal pathogenesis first by the aggregation of humoral factors, and then by a consequent focal inflammatory response and finally wall

breakdown.[1]

### *Risk factors*

Etiological factors include increasing age, male sex, ethnic origin, family history, smoking, hypercholesterolaemia, hypertension and prior vascular disease. Among the risk factors, male sex and smoking are the most important, increasing the chances of AAA development by 4.5 and 5.6 times, respectively.[7]

### *Clinical features*

The majority of AAAs grow asymptomatically, a lethal characteristic of the disease. If the patient is lucky enough, clinicians will detect the AAA during clinical examinations undertaken for an unrelated reason. Otherwise, the AAA will continue growing until possibly the occurrence of rupture, a life-threatening event, which induces severe abdominal and/or back pain and eventual collapse of the circulatory. Approximately 75% of patients with ruptured AAAs die before reaching the hospital. Lower mortality rates, i.e. 40-50 %, have been reported for the patients who are transported to a hospital in time. Aortic aneurysm rupture is ranked as the thirteenth commonest cause of death in the western world, leading to approximately 15.000 deaths each year in the US.[8]

The AAA diameter is currently considered to be the most reliable determinant of rupture risk. The diameter threshold of 5.5 cm is what clinicians use to distinguish small AAAs from big AAAs. The threshold size, if crossed, escalates the risk of AAA being ruptured before the patient takes the proper treatment. Rapid expansion (>1 cm/year) or the development of symptoms such as abdominal pain, tenderness and back pain usually suggest urgent hospitalization and prompt surgical intervention, irrespective of size.[9] However, studies highlight that AAAs with insusceptible diameter size, are also possible to end up rupturing. As the threshold diameter size doesn't seem to warrant the safety of the patient, there is need for additional indicators of AAA rupture potential.

## Endovascular Aneurysm Repair

Since the first case of endovascular aneurysm repair (EVAR) was reported by Parodi et al. in 1991, this minimally invasive technique has become increasingly popular among physicians and patients.[10] The idea behind EVAR is simple: prevention of further aneurysm expansion. It is achieved with the deployment of a preoperatively sized stent-graft, which is implanted transfemorally to the diseased site with a catheter, guided by fluoroscopy and

deployed by either balloon or self-expanding mechanism (Figure 2).[11] EVAR is a minimally-invasive procedure with significantly reduced perioperative mortality, decreased hospital stay and prompt recovery. EVAR is leading in short- term outcomes over open surgery repair while mid-term outcomes are similar in both techniques.[12]

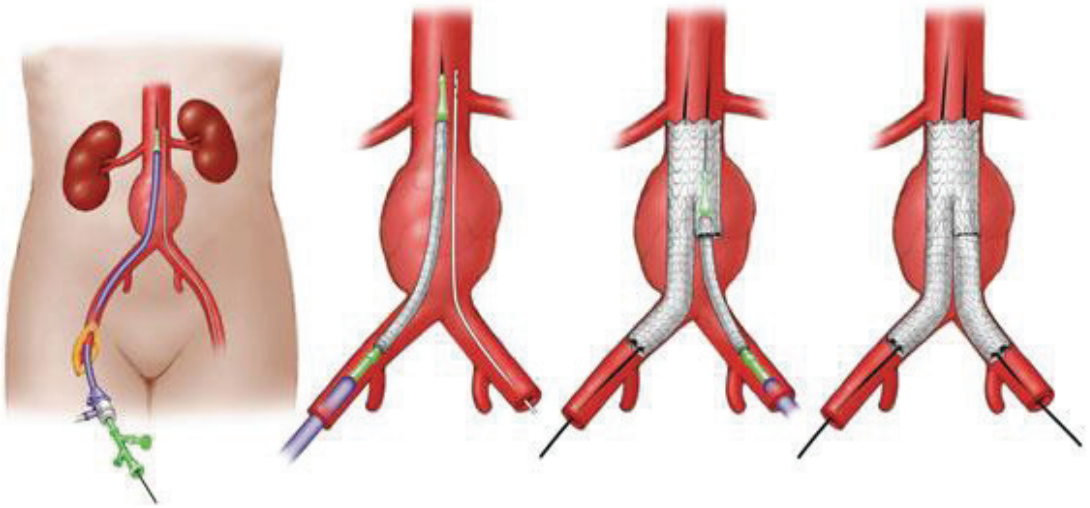

*Figure 2. Schematic representation of EVAR. A prosthetic graft supported by a metallic wire-frame called stent, is implanted transfemorally to the diseased site with a catheter, guided by fluoroscopy and deployed by either balloon or self-expanding mechanism.*

### *Evaluation of the patient with known AAA*

Currently, available evidence supports elective surgical intervention for the treatment of asymptomatic AAAs of 5.5 cm diameter or greater, subject to evaluation of the patient's general health and fitness for surgery. The aims of evaluation of patients diagnosed with an AAA are threefold: 1) to identify patients in whom the balance of risk favors operative intervention; 2) to reduce perioperative morbidity and mortality by identifying patients who may require further investigation or treatment of comorbidity prior to surgery; 3) to assess the anatomical suitability of the aneurysm for open or endovascular repair. Accurate clinical assessment is imperative as it is recognized that perioperative mortality is related to the pre-existing physiological status of the patient.[13] The majority of early deaths following AAA repair are related to cardiac events and if pre-existing cardiac abnormalities are detected and treated before surgery, a substantial improvement in survival rates can potentially be achieved.[14] The risk of perioperative renal failure is increased in those with pre-existing renal disease, diabetes or coexisting cardiac disease, and in those aged over 60 years.

### *Procedural imaging*

Ultrasound is useful for the initial detection and outpatient surveillance of an AAA. Preoperatively, virtually all elective patients now undergo more detailed cross-sectional imaging with contrast-enhanced computed tomography (CT). With thin slice acquisition of data, multidetector row scanners provide excellent three-dimensional images from which to plan endovascular repair.[15]

### *Indications and eligibility of EVAR*

Originally developed as a treatment option for those where existing comorbidity prohibited open surgical repair, the current indications for EVAR are less clear. The approach may well be preferable in cases of a hostile abdomen (e.g. peritoneal adhesions, intestinal stomas) and also where the risk of iatrogenic injury is significant.

Contrary to open AAA repair, EVAR suitability depends not only on patient fitness but also aneurysmal morphology. Limitations of contemporary endografts and their delivery platforms continue to preclude EVAR in many patients, with current elective eligibility rates quoted between 55% and 74%.[16,17] Features promoting EVAR suitability include a healthy proximal neck with limited angulation, at least 15 mm in length, no more than 30 mm in diameter and with smooth, parallel, endoluminal surfaces without significant mural thrombus. In addition, the iliac arteries should be of sufficient calibre, at least 7 mm for most devices, to facilitate the passage of the delivery apparatus into the abdominal aorta. Short ectatic common iliac arteries represent relatively unfavorable anatomy for EVAR given the need for a reliable distal seal.[18]

## Endovascular devices

### *Basic design*

*Figure 3. Basic design of a tubular graft supported by a metallic frame, a stent.*

A stent graft is an artificial flexible blood conduit, designed to act as a false lumen at the site of an aneurysm. It consists of a tubular graft supported by a foldable metallic frame, called stent (Figure 3). Over the last two decades, EVAR has emerged as the treatment of choice for morphologically suitable AAAs and the demand for

efficient stent-grafts has increased. The collaboration of clinicians and bioengineers has boosted the innovation of stent-graft designs with varying stent material, graft fabric, fixation, deployment precision, ease of use, delivery sheath size, and flexibility.[19]

The material of the stent-graft is subject to the pulsatile arterial blood flow. Polyethylene terephthalate (PET; e.g., Dacron) and polytetrafluoroethylene (PTFE; e.g., Teflon) are high strength, resilient, and lightweight polymers, of which most aortic stent-grafts are typically constructed. For the stent skeleton, stainless steel, nitinol (a nickel and titanium alloy), or cobalt chromium alloys are the options that depend on the graft material as well. In general, the stent cage must balance strength, conformability, and compressibility to maximize aneurysm repair durability and device deliverability through challenging aortic and iliac artery anatomy. Similarly, the stent-grafts apply varying techniques to achieve fixation to the aortic wall, typically involving hooks, barbs, anchors, or staples that embed into the aortic wall, or by letting the stent-graft rest on the aortic bifurcation.[20]

Four distinct generic schemes are typically dominant in EVAR of infrarenal AAAs: straight aorto-aortic tube endografts, bifurcated systems, aorto-mono-iliac systems and combined bifurcated and iliac branched stent grafts. All devices form their proximal seal within the infrarenal aortic segment, but differences exist in the location of the distal 'landing site'. Bifurcated systems offer a reliable solution by providing the potential for distal fixation beyond the vascular segments that most likely suffer further aneurysmal expansion in the long term, while maintaining normal anatomical relations. The currently available standard bifurcated devices may be appropriate for use in up to 50% of patients. As newer devices become available for the treatment of short and angulated proximal necks, more patients will be eligible.[21]

***Current devices***

*Endurant*

The Endurant is a modular device made of multifilament polyester fabric and electropolished Nitinol stents (Figure 4). Proximally, it has a suprarenal fixation system made of a one- piece laser-cut Nitinol stent with anchoring pins. The first sealing stent is M-shaped, intended to provide good neck conformability. The remaining stent structure of the body and limbs was engineered to provide flexibility in tortuous anatomy. The suprarenal stent remains constrained with a tip capture mechanism until the desired position of the proximal fabric is reached, and is then released gradually with a wheel at the end of the delivery system. Radio-opaque markers are provided at all levels to facilitate fluoroscopic imaging and accurate placement. The main bifurcated components are provided with proximal diameters ranging from 23 to 36 mm and packed in an 18 or 20 French delivery catheter. They are intended to seal inaortic necks measuring 19 to 32 mm in diameter. The limbs come in 10 to 28 mm diameters for iliac sealing and are packaged in a 14 or 16 French carrier. The treatment range in the iliac arteries is 8 to 25 mm. The single-use delivery catheter for each component is covered with a hydrophilic coating to improve delivery in diseased iliac arteries.[22]

*Figure 4. Endurant stent-graft system.*

*Excluder*

The Gore Excluder is a modular bifurcated stent-graft (W.L. Gore and Associates, Flagstaff, AZ, USA) with documented efficacy, safety, and durability.[23] It is composed of expanded polytetrafluoroethylene (PTFE) combined with a thin, non-permeable layer of fluorinated ethylene propylene, attached to a nitinol stent frame. Its main body has a single docking limb that supports an assortment of iliac limbs and proximal extensions to fit a range of aneurysmal morphologies. The fixation of Gore Excluder is achieved with the use of nitinol barbs at the proximal neck of the main body. The Excluder device is currently approved to treat infrarenal aortic neck diameters ranging from 19 to 29 mm with a minimum aortic neck

length of 15 mm and a proximal aortic neck angulation lower than 60°. The diameter of iliac arteries must lie between 8 to 25 mm and distal iliac vessel seal zone length must be at least 10 mm to ensure safe delivery and sufficient seal.[24]

*Endologix AFX*

The AFX Endovascular AAA System (Endologix, Inc., Irvine, CA, USA) is the only device that takes advantage of the native aortic bifurcation to achieve fixation (Figure 5). Another unique feature is that the graft is attached to the exterior of the cage with polypropylene sutures only proximally and distally. The graft material, low-porosity ePTFE, is consequently allowed to move independently from the stent cage providing enhanced seal, termed as ActiveSeal with STRATA™. The multilayer processing and bonding of approximately 20 layers of ePTFE, deemed as Strata graft technology, offers exceptional strength, conformability and impermeability. To accommodate the aneurysmal morphology, limb extensions can be attached to the stent-graft system. The AFX delivery system consists of a 17-French hydrophilic introducer sheath with a hemostatic valve and a 9-French contralateral percutaneous access and is applicable to aneurysms with 15mm neck length and less than 60-degree neck angulation.[20]

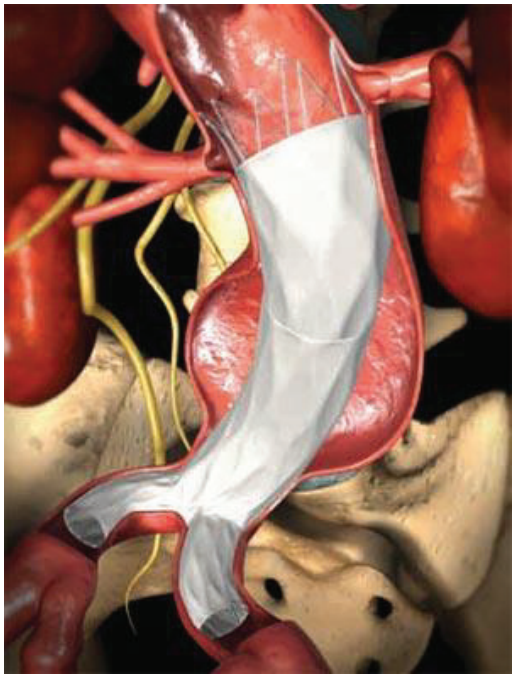

*Figure 5. The AFX Endovascular AAA System.*

*Endologix Nellix*

Endologix Nellix endoprosthesis (Endologix, Inc., Irvine, CA, USA) is a new endovascular device, which is designed to treat aorto-iliac aneurysms by obliterating the aneurysm sac, thus eliminating the endoleak space, while maintaining normal flow to the lower extremities. The system consists of dual, balloon-expandable, endoframes, each of which is surrounded by an endobag that is filled with an in situ curing polymer (polyethylene glycol) as displayed in the graphical simplification of Figure 6.[25] The endoframe stenting material is cobalt chromium and delivered via 17-French sheaths. Each endoframe is surrounded by PTFE and supports the blood flow lumen through the aneurysm sac to the iliac arteries without the need

for proximal and distal fixation. The polymer- containing endobags surround the flow lumen and fill the aneurysm sac providing anatomical fixation.[26]

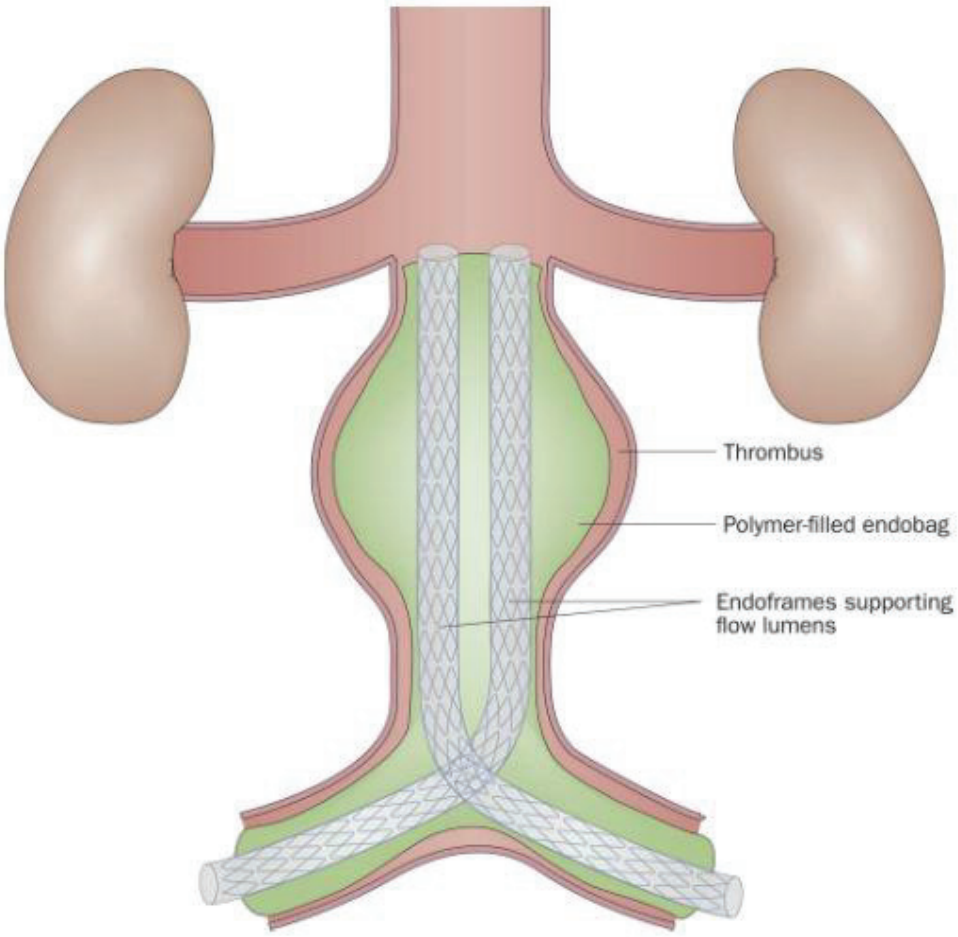


*Figure 6. The sac-anchoring system, consisting of two femorally inserted stent grafts with polymer-filled endobags on the outside of the stent. The polymer-filled endobags enlarge to a pressure preset to support the stents within the aneurysm sac. The technology eliminates the endoleak space via obliteration of the aortic aneurysm sac.*

### *EVAR-related complications and device failure*

*Endoleaks*

Endoleak refers to the persistence of arterial flow of blood into the "excluded" aneurysm sac but outside the lumen of the deployed stent graft. It represents one or more of the following processes: incomplete sealing of the proximal or distal landing sites (type I); continued blood flow into the sac by collateral and lumbar vessels (type II); an incomplete seal at junctions of overlapping graft components or ruptured graft fabric (type III); or leakage of blood through a porous graft membrane (type IV), Figure 7. [19] The incidence of endoleak is approximately 20% and may be further classified as immediate, early, or late. Without

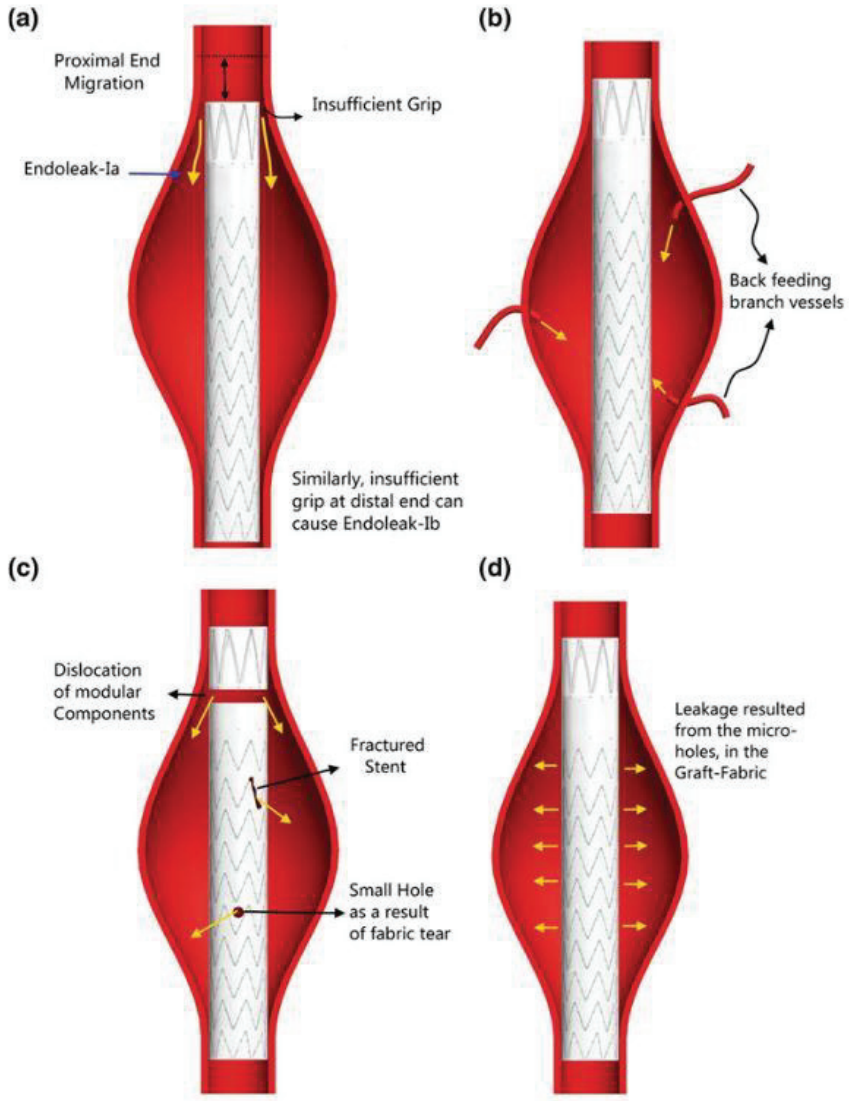


*Figure 7. Different types of endoleaks. a) Type I—Proximal leak, b) Type II—Leak through branch vessels, c) Type III—Mechanical failure, d) Type IV—Leakage due to graft porosity.*

treatment, the aneurysm may continue to expand, thus carrying the risk of rupture, although most cases seal spontaneously with thrombosis. Bearing this in mind, the majority of vascular surgeons initially manage an endoleak with simple observation. If, after a prescribed time period, the endoleak persists or rapid aneurysm expansion is observed, further interventions such as endoluminal graft extension deployment, band ligation of the aortic aneurysmal neck, or even open repair may be indicated.[1]

*Migration*

As part of the circulation (a passage for blood), the endografts are subjected to fluctuating displacements. If their magnitude increases unexpectedly, an irreversible dislocation of the endograft might take place. The seals fail to allow blood to flow in the previously excluded aneurysmal sac. The application of systemic pressure to the aneurysmal sac is an immediate consequence of migration. The distal movement of the stent-graft at the proximal fixation site is met in most cases. However, the proximal movement of the distal limbs in the iliac arteries is not impossible. Late migration (1 year after implantation) is the main reason for reinterventions.[27]

The excessive oversizing of an endograft is frequently associated with migration phenomena, as reported by Sternberph et al.[28] To prevent migration, the device should be placed correctly. Even miniscule deviation from the lower renal artery, increases the risk of migration by 5.8% for the AneuRx stent-graft system, according to Zarins et al.[29] The exclusion of the aneurysmal sac succeeds only if adequate proximal fixation is achieved. Accordingly, the iliac fixation length is a migration-preventing factor as well as the endograft takes greater support.[30,31] Higher migration resistance is associated with balloon-expandable stent-based grafts, which are attached to the internal elastic lamina stronger than self-expanding stent-based grafts.[32] After the promising outcomes, the development of balloon-expandable stents has accelerated.

*Kinks, Thrombosis, and Limb Occlusions*

Occlusion of stent-graft limbs due to kinks or thrombosis is a relatively infrequent but nonetheless important problem that occurs as a delayed event in 2.2% to 3.9% of patients.[33,34] Hobo et al.[35] found that the use of iliac extensions during the endovascular procedure was related to the development of kinks in the stent-graft. It would seem reasonable to conclude that preventing stent-graft kinks relies on satisfactory distal fixation. It is likely that patients

who have iliac aneurysms are more vulnerable to stent-graft kinks than patients with healthy iliac arteries.

Morphological changes in the aneurysm that cause geometric changes in the stent-graft are another major cause of stent-graft kinks.[36] Blood flow through a kinked stent-graft may be irregular and could lead to localized thrombosis and stent-graft occlusion. Hypothetically, kinks or occlusions that inhibit the flow of blood through the stent- graft substantially increase drag force, possibly causing migration of the graft. Fransen et al.[37] reported that kinks were significantly associated with type I endoleak, but they were unable to pinpoint whether the migration and subsequent failure of the proximal seal was a result of the kinks or the kinks were a result of the migrated graft.

*Endotension*

This term refers to continued pressurization and expansion of the aneurysm sac after EVAR when no endoleak can be identified on computed tomography (CT). Endotension, which occurs in up to 15% of patients, can cause significant increase in aneurysm diameter and increase the risk of rupture. Endotension usually requires secondary intervention.[38]

Several theories have been put forward to explain endotension, including the transfer of pressure through a thrombotic seal at the attachment sites, very low flow endoleak, and graft fabric tears sealed with thrombus. Lin et al.[39] stated that aneurysm enlargement cannot occur without expansion of intrasac volume and hypothesized that this in turn means continued thrombus generation from endoleak, supporting the low flow theory. Another possible explanation is that blood components could transude through the walls of the stent-grafts and be responsible for this phenomenon.[39] Endotension is more frequently associated with stent-grafts that are fabricated from expanded polytetrafluoroethylene (ePTFE).

Until recently, noninvasive monitoring of excluded aneurysm sac pressures had not been possible. Sonesson et al.[40] described a catheter-based method that could identify aneurysms subjected to high pressure when no endoleak is visible on the completion angiogram. Using this method, they concluded that successful EVAR reduced sac pressure to 20% of systemic pressure. They also utilized this method to investigate the difference in sac pressures in shrinking, unchanged, and expanding aneurysms. In patients without endoleaks, the investigators found that the mean pressure index (MPI: percentage of mean aneurysm pressure relative to mean systemic pressure) for shrinking aneurysms was 19% versus 59% for expanding aneurysms. In aneurysms that did not change in size, they identified two (2)

groups: patients with an MPI similar to the expanding-aneurysm group, who subsequently showed expansion of their aneurysm, and patients with lower MPIs, who displayed shrinking aneurysms.[41] This method of aneurysm pressure measurement has been validated in vivo and in vitro; it is repeatable and could be an invaluable tool in deciding the best course of action for aneurysms that remain unchanged in diameter or expand after EVAR.[42]

Recently, a wireless AAA pressure sensor that can monitor sac pressures over the life of the stent-graft was made available. This device may produce completely noninvasive measurements similar to Sonesson et al.[40] and Dias et al.[41] and could lead to a more in-depth understanding of the endotension enigma, facilitating corrective action prior to the aneurysm being at risk of rupture.[43] These methods measure pressure locally and then assume it as the global pressure inside the aneurysm sac. Unfortunately, pressure distribution in the thrombus within the excluded aneurysm sac may not be uniform, which could lead to underestimating the intrasac pressure and the rupture risk of certain aneurysms.[44] These pressure differences are most likely due to the microstructure of the intraluminal thrombus (ILT).

## Computational approaches

### *AAA modeling*

The AAAs have several aspects that have not been explored exhaustively due to the complexity of the disease. The use of computational modeling facilitates the research for the mechanical factors related to the genesis, growth and rupture of AAAs. The computational approach has several advantages. It is by nature non-invasive and demands limited resources. In contrast to experiments, computational simulations feature increased flexibility and are certainly less time-consuming. The numerical techniques also offer higher resolution than imaging modalities and can capture phenomena unobservable by cardiac-gated imaging sequences.[45]

The AAA modeling has mainly two branches: the arterial wall mechanics (solid mechanics) and the blood flow properties and patterns (fluid mechanics). Recent technological advancements have enabled simulations that combine blood flow and arterial wall in a single fluid-solid interaction model.[46]

### *Solid mechanics*

Three basic types of information are needed to solve any problem in continuum mechanics: geometry, material properties, and applied loads/boundary conditions. Advances in medical

imaging, particularly CT and MRI, provide precise information on patient-specific geometries. Applied loads arise primarily from three sources: the hemodynamic loads that act on the luminal surface, the perivascular tissue that acts on the outer surface, and an inherent pre-stretch that stresses the aorta axially. Whereas hemodynamic loads (i.e., components of the traction vector normal and tangential to the lumen) can be estimated from computational studies, perivascular effects remain difficult to assess.[47] In vivo residual and axial pre-stresses and material properties are similarly difficult to assess on a patient-specific basis, particularly when seeking to include changes due to aging, co-morbidities, and the evolution of the lesion.[48,49]

*Figure 8. Velocity streamlines in an anatomical model derived from reconstruction of computed tomography data.*

*Mechanical properties*

Despite universal recognition of the importance of wall mechanics in the natural history of AAAs, there have been few detailed studies of the mechanical properties.[50,51] Early studies focused on gross measures of structural stiffness, which are useful for clinical correlations but not biomechanical analyses.[49] The most complete data on both the (biaxial) mechanical behavior of aging aorta and AAAs comes from vande Geest et al.[52,53] Ferruzzi et al.[54] report quantifications of these data using a single nonlinear constitutive relation and both Labrosse et al.[55] and Haskett et al.[56] compared them to other aortic locations. Nevertheless, we must account better for the different compositions and properties of the intima, media, and adventitia within the aorta and how they contribute to lesion enlargement.[57] There have also been limited studies on the mechanical properties of ILT, the most complete of which include vande Geest et al.[58] and Tong et al.[59]

*Finite element analysis*

Stress analyses have appropriately improved from early estimates based on Laplace's equation, axisymmetric membrane solutions, and linear elastic FEA such that most studies

now use geometrically and materially nonlinear FEA. Moreover, many other inappropriate assumptions (e.g., idealized geometries, isotropic properties, and stress-free diastolic reference configurations) have given way to more sophisticated studies, which can include the presence of calcifications and/or an ILT.[60-65] Nonetheless, most studies continue to assume an isotropic constitutive behavior despite clear evidence to the contrary.[53,66] Moreover, nearly all prior studies assumed uniform wall thickness and all prior studies assumed material homogeneity, both of which are unlikely based on available mechanical and histological data and growth and remodeling computations.[67,68] There is clearly a need for improved computational modeling.[49]

***Fluid mechanics***

Computational fluid dynamics (CFD) has been used for several years to identify mechanical risk factors associated with aneurysmal evolution and rupture as well as to understand flow characteristics before and after surgical treatments to help the clinical decision-making process. The flow conditions that might promote the development of ILT are under extensive research as well. The latest breakthrough was the coupling of CFD with anatomical models featuring patient-specific morphologies of AAAs, deporting gradually from idealized geometries designed in computer-aided design (CAD) software.

CFD can provide a list of informative flow properties such as flow and pressure fields, principal and shear stresses - in variations involving spatial and time averages throughout the cardiac cycle - or the helicity index that combines velocity and vorticity. With so many hemodynamic data being available in a patient-specific manner, the progress in identifying the clinical implications of pathological blood flow was rapid.

Studies into AAA hemodynamics have helped reveal possible biomechanical mechanisms underlying AAA pathogenesis and progression.[69,70] Early studies started from idealized models, e.g., to track the formation and propagation of vortices, and to determine regions of high shear stresses at the proximal and distal ends of an aneurysm. Finol et al.[71] and Deplanoa et al.[72] studied common asymmetry in AAA, reporting the appearance of asymmetric vortices, and a relative higher shearing of the posterior wall of the aneurysm, which is the most prevalent location of rupture. Peattie et al.[73] and Salsac et al.[74] demonstrated changes to the flow patterns based on bulge diameter, and Egelhoff et al.[75] considered the effects of exercise.

In vivo flow conditions can be far more complicated than flow in simplified aneurysm

models. Patient-specific computational models have been used to predict possible in vivo flow patterns and wall shear stress in AAA (Figure 8).[76] Patient-specific AAA models have also been used in studies of fluid-structure interaction,[77,78] ILT particle,[79-81] image velocimetry,[82] and validation of image-based flow modeling.[83] Vessel morphology has a wide variability in AAA and the geometry of the aneurysm and surrounding vasculature is critical in determining the hemodynamics. Les et al.[45] compared different Eulerian-based flow measures in multiple patient-specific computational models, and Suh et al.[84,85] investigated AAA flow using a Lagrangian-based particle residence time (PRT) measure the effects of exercise.

Despite all these advances many authors point out that several issues remain regarding the consistency and reliability of computational results and the mechanical variables used to characterize the hemodynamic environment, as well as to the analysis of relatively small clinical datasets. Therefore, challenges such as reproducibility and sensitivities of flow parameters due to diverse pre-processing inputs like geometries, grid resolution, inflow and outflow boundary conditions, blood rheology, wall compliance, and solution methods need to be addressed before CFD is qualified for clinical and industrial use.[86]

**Post-EVAR Numerical Simulations**

Endovascular devices are being designed currently by trial and error involving animal testing and human clinical trials to determine their efficiency. Despite the remarkable advances over the past 15 years, there are persistent concerns regarding the long-term durability of endovascular devices. This may be due to deficiencies in device design, which has lagged behind other industries in adopting computational methods that are now routinely used to design, develop, and test new aircraft and automobiles. Similar computational design and failure mode simulations that evaluate performance under stress conditions have not been widely applied in the development of endovascular devices.[87]

Advances in medical imaging and computational modeling now allow simulation of physiological conditions in patient-specific 3-dimensional vascular models, which can provide a framework to design and test the next generation of endovascular devices. This type of modeling will allow the prospective design of devices such that it can withstand the force variations in the cardiovascular system that occur during bending, coughing, and varying degrees of exercise, as well as the extremes encountered during sudden impact in contact sports. Utilization of computational design methodology that takes into

consideration the physiology of the cardiovascular system will improve future endovascular devices so that they are safer and more efficient and durable.[87]

The persistence of complications, despite the technological advancements, urged researchers to search for novel ways to understand the reasons behind their occurrence.[24] The ultimate goal is to design complication-free endografts, taking into account the mechanical challenge of their deployment. The impact of EG implantation on blood flow can be studied by computational means. [87-90] To this end, researchers have managed to quantify post-EVAR effects harnessing the power of computational methods.[91] The migration of an EG and the occlusion of its limbs are multifactorial events, with unambiguous biomechanical aspects.[92-94] The mismatch of EG and arterial wall compliance is considered to promote pressure wave reflections.[95] Morris et al.[96] claimed that excessive hemodynamic variations after EVAR could trigger a catastrophic sequence of events for the vascular system, based on computational and experimental results. Exploiting the plasticity of computational models, Molony et al.[97] proposed geometrical enhancements for the aortic EGs. The fatigue performance of different EG materials is a valuable piece of information for the medical community and industry.[98] Being able to predict deformations during EVAR is an achievement that might inspire the development of future EG generations.[99] Despite that computational studies are promising, the medical community is skeptical about their validation. There are studies nevertheless showing that experiments and numerical simulations are in good agreement.[100,101]

## MOTIVATION AND AIMS

Endovascular aneurysm repair (EVAR) is a reliable method for the treatment of abdominal aortic aneurysms (AAA) with suitable morphology. EVAR has a lead in favorable short-term outcomes over open surgery, but both techniques have similar long-term survival.[12] Meanwhile, the stent-graft technology is evolving. The improvements already benefit more and more patients with anatomically challenging aneurysms. However, there are issues related to EVAR that have not been explored. The motivation of the thesis relies on the following points:

- After EVAR, the endograft establishes a hemodynamic environment that blood is experiencing periodically in every cardiac cycle.
- The literature states that the installation of an endograft alters the hemodynamics with adverse effects possibly perturbing the functionality of the device itself.
- The frequency of postoperative adverse events is variable among the available endografts (EGs).[102,103]
- There are endovascular devices for the treatment of infrarenal AAAs with varying specifications in terms of design and material. It is unknown if the hemodynamic characteristics are different among the various endografts.
- There is a lack of a methodology that can capture the hemodynamic flow within the endografts, after their implantation, therefore accounting for the positioning of the endografts in the aneurysmal sac.
- Computational studies pursuing the endograft hemodynamics mainly involve limited number of medical cases. Computational studies are slowly following the example of clinical studies that employ larger clinical datasets.

Based on the above, the aims of the thesis were the following:

- Establish a computational framework that is driven by medical imaging data and can provide patient-specific hemodynamic analytics. The workflow includes briefly the reconstruction of medical imaging data, development of anatomical models, grid generation, numerical simulations and data post-processing.
- Fit the computational framework in the context of EVAR thus adjusted to account for the positioning of the endografts in the aneurysmal sac.

- Apply the workflow in an extended number of patients introducing statistics into computationally acquired hemodynamic datasets.
- Acquire control data by performing simulations in physiological cases.
- Resolve the hemodynamic performance of 4 commercially available endografts: Endurant, Excluder, AFX and Nellix. Estimate the efficiency of those endograft in terms of restoring the hemodynamic properties to the physiological levels.
- Identify potential hemodynamic differences between the endografts that have similar designs, Endurant and Excluder.
- Estimate the clinical significance of an endograft inducing hemodynamic variations.

The previous aims are pursued by Chapters 2,3 and 4. Chapter 1 is focused on the effects of intraluminal thrombus (ILT) on aneurysmal blood flow. Specifically, we introduce a methodology for the modeling of ILT, which is different from the traditional simulation of the ILT as an elastic structure. ILT is modeled as a porous medium with gradually smaller permeability following studies that provide histological analysis of the ILT structure and report permeability and porosity values throughout the ILT thickening procedure.

# CHAPTER 1

## Effect of Intraluminal Thrombus on AAA Hemodynamics

Intraluminal thrombus (ILT) is found in most AAAs.[104] There is a global debate regarding its role in the growth of AAA and whether it offers protection from rupture or vice versa.[105] The ILT structure and its evolving biological and mechanical properties pose a challenge for developing reasonable mathematical models describing the complex nature of such lesion and its progression.

The formation of ILT is based on the activation, coagulation and clotting of platelets and other blood constituents. Tong et al.[59], based on preliminary studies, proposed a four-phase thrombus gradual formation during which the percentage of erythrocytes and leucocytes or thrombocytes is gradually increasing sustaining a thick fibrin mesh. As ILT is becoming denser, the erythrocytes disrupt until the complete loss of elastic fibers and myocytes. The growth of blood clots, like ILT, is regulated by the interstitial blood flow according to Wufsus et al.[106] They assumed that a clot generally can be modeled as a porous medium. They calculated the hydraulic permeability based on the Darcy's law with known fibrin and platelet densities and they suggested that hydraulic permeability can vary up to five orders of magnitude.

Beyond biological models describing the hemostasis/thrombosis, many computational studies have been developed to simulate thrombus progression. These simulations demonstrate the gradual thrombus formation in space and time. The more complicated part is to include in the model the sub-processes during the blood clotting, like the generation of thrombin on the surface of a platelet, which is taking place in a nanoscale and simultaneously predict the blood flow in the vessel in the macroscale.[107] In a characteristic study by Leiderman and Fogelson, the two-way interaction between the blood flow and the growing platelet mass is modeled by a spatial-temporal mathematical model in terms of fluid dynamics, coagulation biochemistry and chemical activation of blood platelets.[108] The blood flow was described by a modified version of Navier-Stokes equations in which the Brinkman term is added to represent the frictional resistance due to bound platelets.

Realistic modeling of ILT is a standard challenge among researchers developing hemodynamic models of AAAs. The uniaxial tensile properties of ILT were measured and used for modeling it as a linear isotropic material.[109] A hyperelastic isotropic constitutive relation for the ILT which also resulted from uniaxial tensile test indicated the heterogeneity

of the ILT-composed of three distinct layers with different mechanical properties.[110] More recent work has shown that the luminal layer of ILT behaves as an isotropic material.[109-111] Researchers have also proposed models utilizing theory of poro-elasticity or proposed coupled porohyperelastic mass transport models to describe the impact of ILT on wall stresses.[112-115] Others treated ILT as a structural component with typical solid mechanical properties.[116]

The current Chapter details the application of porous media theory to study the effects of ILT on the blood flow in an idealized fusiform AAA with aortic bifurcation.[117] Porosity and permeability of a building-up ILT structure varies as indicated by literature histological data. We demonstrate the disturbed blood flow patterns in the AAA bulge, which possibly trigger the formation of the ILT, through different stages between its onset and its final, more compact form.[118] Modeling ILT as a porous medium offers a representative description of the lesion from a mechanical point of view.

***Methods***

*Mathematical Analysis*

We designed a two-dimensional idealized aneurysmal geometry as shown in Figure 9. Since ILT was experimentally proved to be permeable to fluids, its mechanical behavior is simulated by a porous medium; i.e. a material consisting of a solid matrix with an interconnected void space.[116,119] The fibrous nanostructure of the ILT is part of the solid phase and blood flows within the void space. Porosity, $\phi$, of a porous medium is defined as the fraction of the total volume of the medium that is occupied by the void space.[120] The steady incompressible blood flow within a porous medium of porosity, $\phi$, is governed by the Brinkman-Forchheimer equation accompanied by the continuity equation.[121] In vector form, we get the following equations:

Continuity equation

$$\vec{\nabla}\cdot\vec{u'}=0 \tag{1}$$

Momentum equation

$$\frac{\rho}{\phi^2}\left(\vec{u'}\cdot\vec{\nabla}\right)\vec{u'}=-\vec{\nabla}p'+\mu_e\vec{\nabla}^2\vec{u'}-\frac{\mu}{K_s}\vec{u'}-\frac{c_f\rho}{\sqrt{K_s}}\left|\vec{u'}\right|\vec{u'}. \tag{2}$$

Blood is modeled as an incompressible fluid, of a given density $\rho$. $\vec{u'}$ is the Darcy velocity, $|\vec{u'}|$ is the magnitude of the Darcy velocity and $p'$ is the intrinsic quantity of the pressure.[120] The effective viscosity is $\mu_e$ and is equal to $\mu_e = \frac{\mu}{\phi}$, where $\mu$ is the dynamic viscosity of the blood. $c_f$ is the dimensionless Forchheimer coefficient and $K_s$ is the intrinsic permeability.

*Transformation of Equations and Boundary Conditions*

In the Cartesian coordinate system $(x', y')$, the velocity is $\vec{u'} = \vec{u'}(u', \upsilon')$. We introduce the following dimensionless variables:

$$x = \frac{x'}{l},\ y = \frac{y'}{l},\ u = \frac{u'}{u_0},\ \upsilon = \frac{\upsilon'}{u_0},\ p = \frac{p'}{\rho u_0^2}, \tag{3}$$

where $l$ is a characteristic length and, in our case, is the actual length of the inlet of the idealized aneurysmal geometry and $u_0$ is a characteristic velocity which is equal to the magnitude of the mean velocity of the blood at the inlet. By substitution of the above dimensionless variables (3) into the Cartesian form of the equations (1)-(2), we derive the following coupled dimensionless system of non-linear partial differential equations:

Continuity equation

$$\frac{\partial u}{\partial x} + \frac{\partial \upsilon}{\partial y} = 0 \tag{4}$$

*x*-momentum equation

$$u\frac{\partial u}{\partial x} + \upsilon\frac{\partial u}{\partial y} = -\phi^2\frac{\partial p}{\partial x} + \frac{\phi}{\mathrm{Re}}\left(\frac{\partial^2 u}{\partial x^2} + \frac{\partial^2 u}{\partial y^2}\right) - \frac{\phi^2 \nu l}{K_s u_0}u - \frac{\phi^2 c_f l}{\sqrt{K_s}}u\sqrt{u^2+\upsilon^2} \tag{5}$$

*y*-momentum equation

$$u\frac{\partial \upsilon}{\partial x} + \upsilon\frac{\partial \upsilon}{\partial y} = -\phi^2\frac{\partial p}{\partial y} + \frac{\phi}{\mathrm{Re}}\left(\frac{\partial^2 \upsilon}{\partial x^2} + \frac{\partial^2 \upsilon}{\partial y^2}\right) - \frac{\phi^2 \nu l}{K_s u_0}\upsilon - \frac{\phi^2 c_f l}{\sqrt{K_s}}\upsilon\sqrt{u^2+\upsilon^2} \tag{6}$$

The origin of the coordinate system was placed in the midpoint of the inlet as is shown in

Figure 9. The Reynolds number (Re) is defined by the relationship $\mathrm{Re}=\frac{u_0 l}{\nu}$, where $\nu$ is the kinematic viscosity of the blood.

In the AAA lumen region, there is no solid matrix to obstruct the blood flow defining porosity equal to $\phi$=1. In this way, the Brinkman-Forchheimer equations are converted to the two-dimensional, steady, incompressible Navier-Stokes equations. In the ILT region where porosity is 0< $\phi$<1, the additional terms in the right-hand side of equations (5)-(6) are preserved and the rest are modified. Specifically, the pressure gradient is now multiplied by the square of porosity, the second term is the Brinkman term, the third is the Darcy term and the last is the Forchheimer term. A detailed analysis of the significance of the various terms can be found in the study of Nield.[121]

We assume that velocity at the entrance has a parabolic profile and that fully-developed flow is achieved at the outlets (Figure 9). In this way, the dimensionless boundary conditions are:

- at the inlet: $$u(y)=1-\left(\frac{y}{0.5}\right)^2,\ \upsilon=0,\ -0.5\le y\le 0.5 \quad (7)$$
- at all solid boundaries(wall): $u$=$\upsilon$=0 (no-slip condition) (8)
- at the outlets: $$\frac{\partial u}{\partial x}=\frac{\partial \upsilon}{\partial x}=0,\ p=0 \quad (9)$$

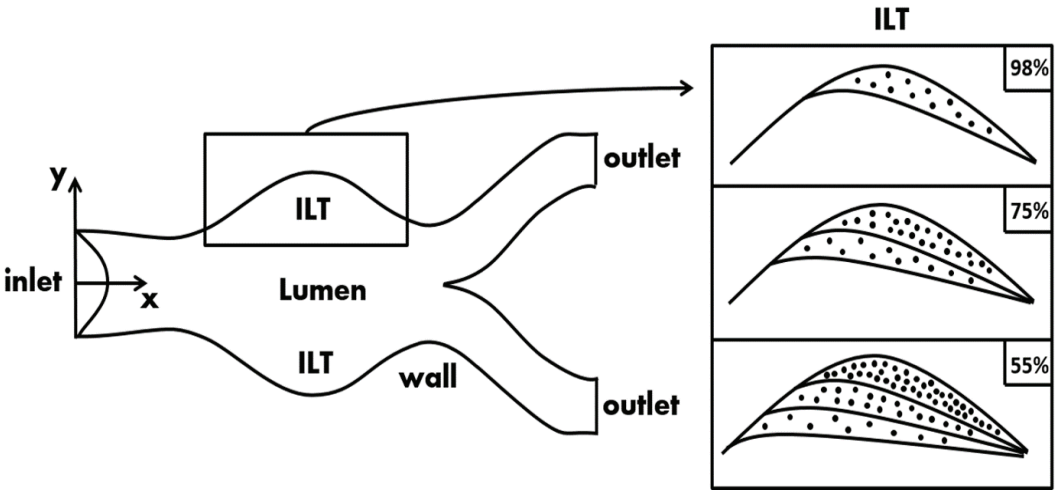


*Figure 9. Two-dimensional idealized aneurysmal geometry and sketch of the ILT formation in three different instances with mean porosity of 98%, 75% and 55% respectively.*

***Numerical solution***

The strong form of the equations (4)-(6) is defined in the above section alongside with the definition of the appropriate boundary conditions (7)-(9). For the numerical solution of the system of non-linear partial differential equations, we utilized the Galerkin Weighted Residual method.[122,123] In the Galerkin approach, the equations are weighted with appropriate weighting functions and the sum of the integrals of the resulting residual equations over each element is equated to zero,

$$\sum_{1}^{n^e} \int_{A^e} wR dA^e = 0, \tag{10}$$

where, $w$ is a weighting function, $R$ is the residual differential equation, $A^e$ denotes the area of each element and $n^e$ is the total number of elements. We also need a definition of the spatial variation of the variables $u$, $\upsilon$ and $p$. The flow domain is divided into quadrilateral elements and the computational grid is demonstrated in Figure 10. The spatial variation is described analytically by appropriate bilinear shape functions, $N_i$, for the velocity components $u$ and $\upsilon$, and linear, $M_i$, for the pressure.

$$u = \sum_{i=1}^{n} N_i u_i,\ \upsilon = \sum_{i=1}^{n} N_i \upsilon_i,\ p = \sum_{i=1}^{m} M_i p_i,\ n = 8,\ m = 4. \tag{11}$$

By substitution of the above definitions (11) into the equations that are drawn from the utilization of the Galerkin Weighted Residual method (10) we derive the weak formulation of the equations (12)-(14). The application of Green's theorem reduces the differential order of the equations. The final algebraic system is:

Continuity equation

$$\sum_{1}^{n^e} \left[ \sum_{j=1}^{n} \int_{A^e} M_i \left( \frac{\partial N_j}{\partial x} u_j + \frac{\partial N_j}{\partial y} \upsilon_j \right) dA^e \right] = 0 \tag{12}$$

$x$-momentum equation

$$\sum_{1}^{n^e} \left[ \sum_{j=1}^{n} \sum_{l=1}^{m} \int_{A^e} \left[ N_i \left( \tilde{u} \frac{\partial N_j}{\partial x} u_j + \tilde{\upsilon} \frac{\partial N_j}{\partial y} u_j + \phi^2 \frac{\partial M_l}{\partial x} p_l + \frac{\phi^2 \nu l}{K_s u_0} N_j u_j + \frac{\phi^2 c_f l}{\sqrt{K_s}} N_j u_j \sqrt{\tilde{u}^2 + \tilde{\upsilon}^2} \right) \right. \right. \tag{13}$$
$$\left. \left. + \frac{\phi}{\mathrm{Re}} \left( \frac{\partial N_i}{\partial x} \frac{\partial N_j}{\partial x} u_j + \frac{\partial N_i}{\partial y} \frac{\partial N_j}{\partial y} u_j \right) \right] dA^e - \frac{\phi}{\mathrm{Re}} \int_{\Gamma_q} N_i \left( \frac{\partial u_j}{\partial n} \right)^{\Gamma_q} d\Gamma \right] = 0$$

*y*-momentum equation

$$\sum_{1}^{n^e}\left[\sum_{j=1}^{n}\sum_{l=1}^{m}\int_{A^e}\left[N_i\left(\tilde{u}\frac{\partial N_j}{\partial x}\upsilon_j+\tilde{\upsilon}\frac{\partial N_j}{\partial y}\upsilon_j+\phi^2\frac{\partial M_l}{\partial y}p_l+\frac{\phi^2\nu l}{K_s u_0}N_j\upsilon_j+\frac{\phi^2 c_f l}{\sqrt{K_s}}N_j\upsilon_j\sqrt{\tilde{u}^2+\tilde{\upsilon}^2}\right)\right.\right. \quad (14)$$
$$\left.\left.+\frac{\phi}{\mathrm{Re}}\left(\frac{\partial N_i}{\partial x}\frac{\partial N_j}{\partial x}\upsilon_j+\frac{\partial N_i}{\partial y}\frac{\partial N_j}{\partial y}\upsilon_j\right)\right]dA^e-\frac{\phi}{\mathrm{Re}}\int_{\Gamma_q}N_i\left(\frac{\partial \upsilon_j}{\partial n}\right)^{\Gamma_q}d\Gamma\right]=0,$$

where $\Gamma_q$ denotes the boundary where flux is defined. $\tilde{u}$ and $\tilde{\upsilon}$ are assumed to be constants when formulating the matrices. The equations are defined in the global ($x$, $y$) coordinate system but are transferred to a local ($\xi$, $\eta$) one making the methodology applicable in complex geometries. It is necessary that a direct relationship exists between discrete variables and the global coordinate location.[124] The first order variations with respect to the global coordinates must also be expressed in local terms and this can be achieved by the expressions of the form,

$$\begin{Bmatrix}\frac{\partial N_i}{\partial \xi}\\ \\ \frac{\partial N_i}{\partial \eta}\end{Bmatrix}=\begin{bmatrix}\frac{\partial x}{\partial \xi} & \frac{\partial y}{\partial \xi}\\ \\ \frac{\partial x}{\partial \eta} & \frac{\partial y}{\partial \eta}\end{bmatrix}\begin{Bmatrix}\frac{\partial N_i}{\partial x}\\ \\ \frac{\partial N_i}{\partial y}\end{Bmatrix}=J\begin{Bmatrix}\frac{\partial N_i}{\partial x}\\ \\ \frac{\partial N_i}{\partial y}\end{Bmatrix}, \quad (15)$$

where $J$ is the Jacobian of the transformation and can be evaluated explicitly since the local variation in $x$ and $y$ can be defined. Inverting $J$ to find the global variation in the shape function, we can re-write,

$$\begin{Bmatrix}\frac{\partial N_i}{\partial x}\\ \\ \frac{\partial N_i}{\partial y}\end{Bmatrix}=J^{-1}\begin{Bmatrix}\frac{\partial N_i}{\partial \xi}\\ \\ \frac{\partial N_i}{\partial \eta}\end{Bmatrix} \quad (16)$$

The inverse of the Jacobian can be found by using standard matrix inversion techniques,

$$J^{-1} = \begin{bmatrix} \frac{\partial \xi}{\partial x} & \frac{\partial \eta}{\partial x} \\ \\ \frac{\partial \xi}{\partial y} & \frac{\partial \eta}{\partial y} \end{bmatrix} = \frac{1}{\det J} \begin{bmatrix} \frac{\partial y}{\partial \eta} & \frac{\partial y}{\partial \xi} \\ \\ -\frac{\partial x}{\partial \eta} & \frac{\partial x}{\partial \xi} \end{bmatrix}, \det J = \frac{\partial x}{\partial \xi}\frac{\partial y}{\partial \eta} - \frac{\partial x}{\partial \eta}\frac{\partial y}{\partial \xi} > 0. \quad (17)$$

The only further transformation required is,

$$dxdy = \det J d\xi d\eta, \quad (18)$$

where det$J$ is the determinant of $J$ with the assumption that it is non-zero and positive and $x_\xi$, $x_\eta$, $y_\xi$, $y_\eta$ are the metrics of the transformation. The above procedure is thoroughly described by Somayaji et al.[125] for integration with the Finite Volume method but is also applicable in the current study. Gauss-Legendre quadrature is used for the numerical evaluation of the integrals in (12)-(14). After the formation of the element matrices, these are assembled into a global fluid matrix which is solved using a Gaussian elimination technique.[126]

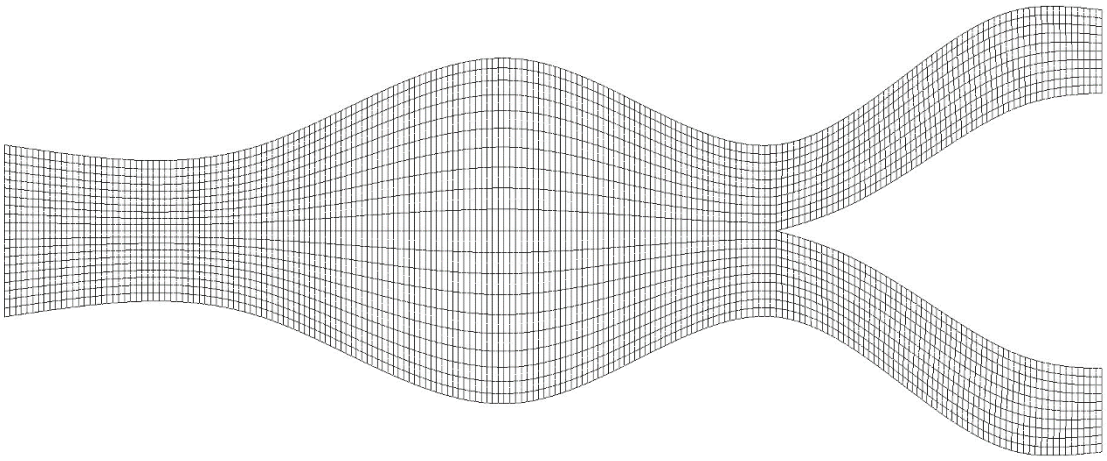

*Figure 10. Structured computational grid of the idealized abdominal aortic aneurysm composed of finite elements.*

Finally, we denote that mesh convergence has been optimized so that the results are not depended on the size of the grid. Specifically, we calculated the Root Mean Square (RMS) in the section where the aortic wall is dilated as the development of ILT and the existence of vortices could potentially make the accuracy of the results vulnerable. So, based on a grid of 12.000 elements we are demonstrating the % RMS error for a grid of 6.000, 3.000 and 1.500 elements respectively. The % RMS error generated by the utilized grid of 6.000 elements is

less than 1% proving that we have achieved grid independence, Table 1.

*Table 1. Grid independence study.*

| Grid size | RMS % |
|---|---|
| **1500** | 2.51 |
| **3000** | 1.09 |
| **6000** | 0.71 |
| **12000** | - |

***Results***

The development of thrombus is mainly based on the aggregation of activated platelets and the entrapment of erythrocytes.[118] Wufsus et al.[106] correlated the fibrin and platelet density with the permeability of an evolving blood clot. In our case, the porous medium that simulates the ILT structure is characterized by their proposed range of porosity and permeability. Specifically, porosity belongs in a range of $0.45<\phi<0.98$ and intrinsic permeability in a range of $1.5E\text{-}10<K_s<1.2E\text{-}7 m^2$. Reynolds number was set to Re=300, describing a mean value during the dynamic cardiac cycle.[127] The Forchheimer coefficient was set to, $c_f$=0.1. [120]

Initially, we considered a case of an AAA with fully dilated aortic wall but without ILT developing in the dilatation region. We modeled blood flow inside the aneurysm by setting, $\phi$=1 in every region of the idealized geometry, Figure 9. In this way, we didn't incorporate the frictional resistance due to the porous medium which represents the ILT structure. The rationale behind the developing of blood flow in an AAA without ILT was to use the results for comparison purposes. Subsequently, we activated the porous medium in the ILT region but kept $\phi$=1, in the AAA lumen region to preserve the unobstructed blood flow. We performed consecutive simulations employing increasingly smaller values of porosity and permeability according to the predefined range.

The case of AAA without ILT showed that, in the dilatation region, a vortex is developing occupying the greater portion of the aneurysmal bulge. Figure 11 demonstrates the effect of the macroscale ILT formation on the blood streamlines through different stages between its onset and its final, more compact, form. It is evident that the vortex is slowly diminishing while moving towards the neck of AAA with permeability gradually reducing which means

that the ILT is getting more compact. For a permeability range of 3E-10<$K_s$<1.2E-7$m^2$, the vortex is not altered significantly but surpassing a crucial value of, $K_s \approx$ 3E-10$m^2$, the vortex is restricted to the zone proximal to neck and completely vanishes while ILT structure acquires more condensed formation. The restriction of the vortices shows in a mechanical way that the ILT is gradually developing and seem to justify the utilization of porous media theory in the ILT modeling.

The examination of the velocity results showed that blood flow in the AAA lumen region accelerates with reducing permeability. Figure 12 demonstrates the velocity profiles in the lumen and the dilated region for an AAA case without ILT and two cases with ILT. Mean velocity increases by 9.9% and maximum velocity increases by 17.1% comparing the AAA case without ILT and the case with a fully compact ILT ($\phi$ =0.45, $K_s$=1.5E-10$m^2$). The results indicate that blood velocities in the aneurysmal cavity are getting nullified while ILT is getting more compact.

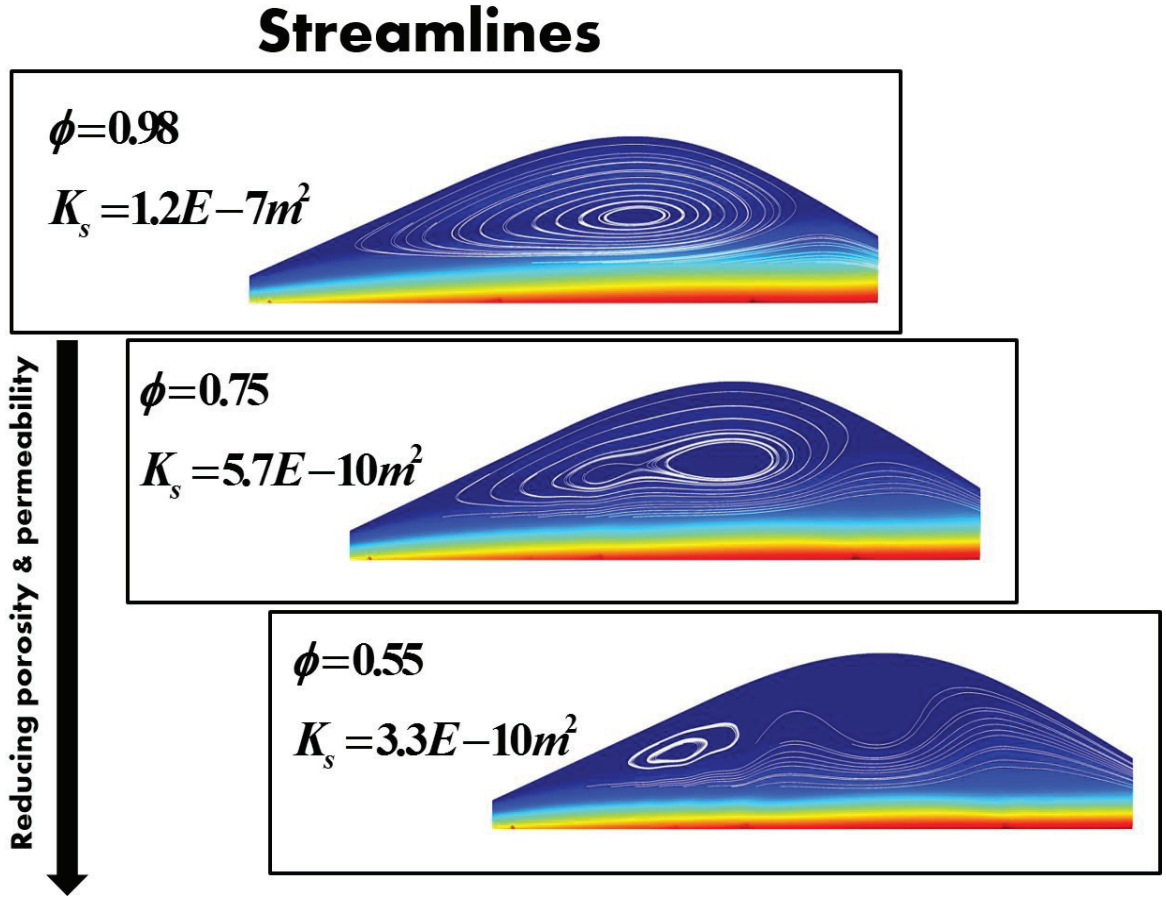


*Figure 11. Contours of the magnitude of the velocity and visualization of blood streamlines in ILT to demonstrate the impact of reducing intrinsic permeability, $K_s$, on the vortex.*

Pressure results in the aneurysmal bulge seem to be of great interest. Maximum pressure decreases by 7.17% and mean pressure decreases by 5.62% inside the dilated region comparing the case of AAA without ILT and the case of a compact ILT ($\phi$ =0.45, $K_s$=1.5E-10$m^2$), Figure 13. An interpretation could be that the gradual formation of the ILT is having a cushioning effect with possible extensions to the aneurysmal expansion rate and the rupture risk. On the other hand, results indicated that in the ILT zone close to the neck of the aneurysm, pressure is increased by 9.87%. So, the ILT development seems to relocate the position where the maximum pressure is observed from the region distal to the region proximal to neck.

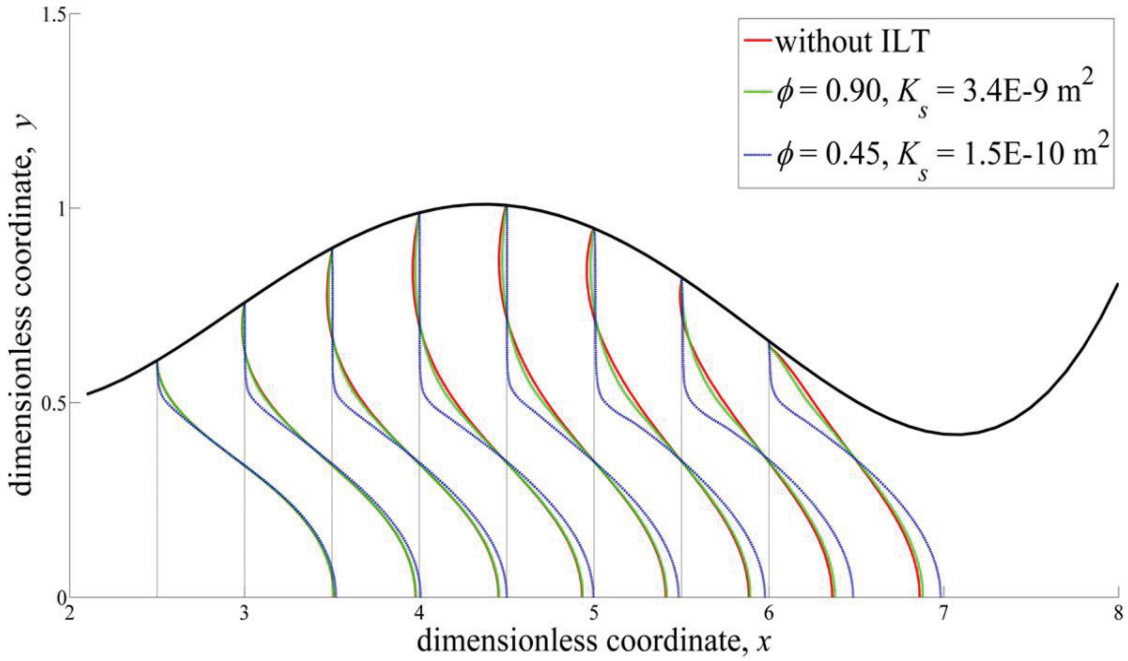


*Figure 12. u-velocity profiles at x-direction in the axisymmetric dilatation region for different values of intrinsic permeability, $K_s$.*

### *Discussion*

Many researchers develop models of AAAs focusing on biomechanical properties like the potential rupture site and not necessarily with the microscopic subprocesses taking place in the ILT structure. Different ILT modeling approaches, however, might predict different values of the biomechanical properties.[113] Modeling ILT as an elastic material limits the interaction of blood - ILT on their interface by using the computed lumen pressure as a boundary condition for a solid mechanics analysis of ILT.[81,128] This approach does not engage the fluid flow through ILT which was also a goal for Ashton et al.[129] On the other

hand, studies describing ILT as a poroelastic material neglect to report the fluid behavior, e.g. recirculation zones, and focus their attention to the pressure distribution in the poroelastic material.[112,113] Generally, modeling thrombus as a porous medium through which pressure is transmitted seems to be more representative than modeling it as a solid structure, as initially proposed by several researchers.[105,106,130] Furthermore, there is a lack of a computational approach that incorporates a macroscale at least description of the ILT formation.

The interaction of biochemical and biomechanical properties is a significant factor leading to the genesis and development of ILT. Many computational studies of hemodynamic flow in idealized or patient-specific aneurysmal geometries suggest that disturbed hemodynamics, like vortical structures, are developing and propagating inside the AAA cavity during the cardiac cycle. [80,131,132] The recirculations set up a viable mechanism that can explain the formation and growth of the ILT, according to several researchers.[77,79-81,133] Specifically, recirculations are favorable regions to platelet activation where the high shear stresses may be active for long enough. The activated platelets adhere at regions of low wall shear stresses posing the foundation of the lesion.[79] The luminal blood flow feeds the fresh fibrin-dominated matrix with new blood cells. The volume increase of ILT is also correlated with the enhanced blood particles residence time inside vortical structures, as explained by Basciano et al.[133] The ongoing deposition and entrapment of blood constituents, mainly eryrthrocytes, inside the fibrin mesh leads to a reduction of the vortices and a parallel decrease of the ILT fibrin structure permeability during time. The results provided by our model showed that the vortices inside AAA bulge are gradually diminishing and stop developing after a crucial value of permeability. A comparison of our results with the processes that are believed to lead to ILT initiation and development justify the utilization of the porous media theory. Similar results regarding the ILT formation are also indicated from histological investigations.

There is a debate whether the presence of ILT offers protection to the AAA as Thubrikar explains.[134] Schurink et al.[135] and Hans et al.[136] claim that there is no significant differentiation between lumen pressure and pressure within the ILT which can be explained by the fact that ILT is permeable to fluids. However, a question of great significance is which are the differences of blood pressure in AAAs cases with ILT under development and without ILT at all? An answer to this question could explain whys AAAs without ILT seem to be more prone to rupture.[118] Our analysis showed that mean pressure is reducing through

the ILT establishment procedure. So, by a fluid mechanics point of view, we can speculate that the aneurysm is more protected under the presence of ILT. On the other hand, very interesting is the fact that pressure in the zone proximal to the neck is increasing. It seems that while ILT is getting more condensed, a rupture event might take place in the upper region of the aneurysm, closer to the neck. This finding might be important as Li et al.[137] suggest that highest value of wall stress does not occur strictly at the maximum AAA diameter but more likely in its neck or shoulder. The induction of disturbed hemodynamic flow may cause changes in the neck and shoulder regions as predicted by Wilson et al.[138]

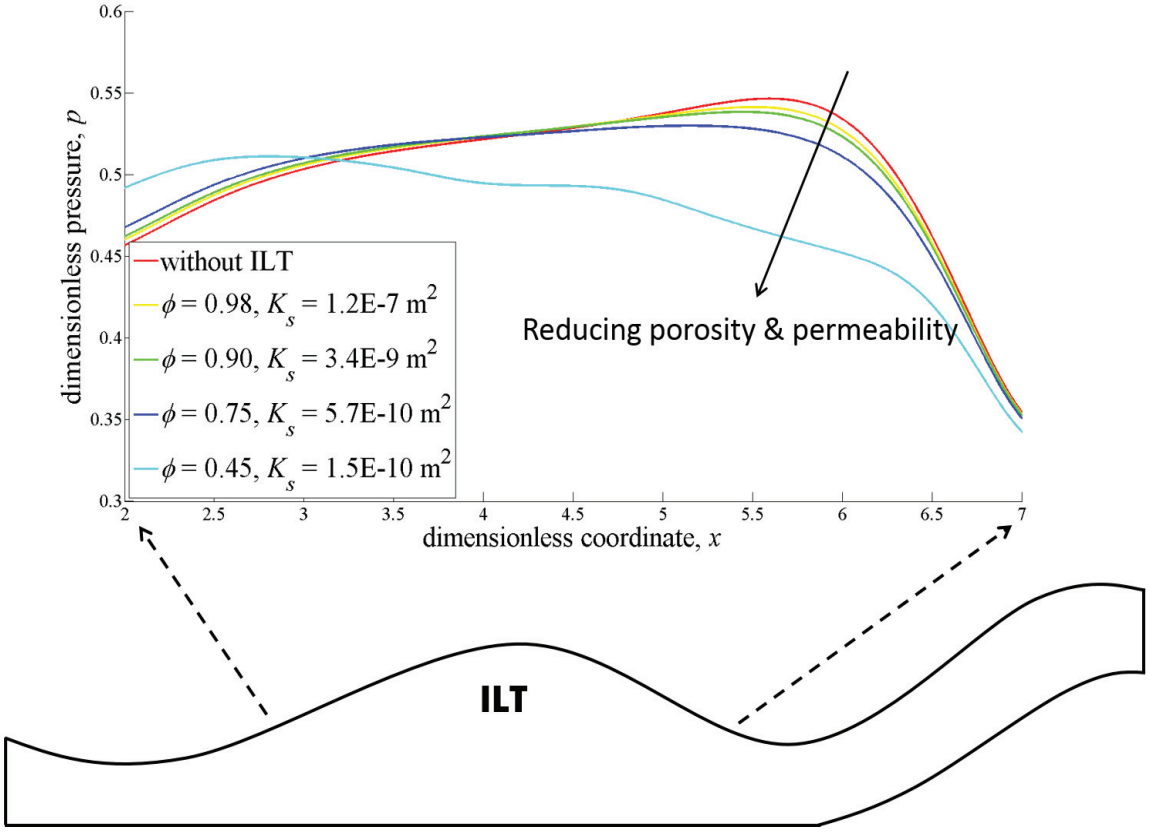


*Figure 13. Dimensionless pressure, p, distributions in ILT.*

The results suggest probable clinical implications that more studies are required to confirm them. The decreasing ILT permeability values, i.e. the modeling of the gradual ILT formation, resulted in the decrease of blood pressure in the ILT structure. Pressure reduces significantly compared to the AAA case without ILT. On the other hand, it is highly possible that the degradation of the AAA wall, and eventually its rupture, may have its source in the ILT. So, the emergence and formation of the ILT may decelerate but eventually may induce a rupture event.

The permeability of ILT is inhomogeneous based on the different layers observed in that

structure (luminal, medial and abluminal). In our computations, we utilized a mean value of porosity and permeability over the ILT, like Polzer et al.[112] Moreover, the mathematical model does not engage the interaction of the porous medium (ILT) with the aortic wall. Other mechanisms, such as the gradual wall weakening that usually accompanies AAA and ILT formation are not included in the current study. Advanced three-dimensional fluid structure interaction modeling of blood flow through a porous medium (ILT) is a future aim for our group.

***Conclusions***

The conventional approach to model ILT is as an elastic structure. The disadvantage is that in this way the interaction of blood flow with the ILT is limited to the surface of ILT. The type of modeling affects the calculations, with the possibility that the numerical simulations predict a different mechanical response of ILT than the actual one occurring in vivo. Histological analyses have shown that ILT is permeable, especially in the initial phases of its formation. Based on the literature, we introduced a type of ILT modeling with attached permeability and porosity properties enabling a macroscale simulation of ILT thickening procedure. Our simulations predict the development of a recirculation zone that is restricted to the shoulder of the aneurysm while ILT is thickening, exactly as described theoretically in the literature. The pressure at the surface of the ILT decreases during its initiation, formation and maturation offering probably protection to the aneurysm. A clinical implication suggested by the study is that an aneurysm might be more prone to rupture when ILT is fresh contrary to when ILT is mature.

## CHAPTER 2

### Physiological vs Postoperative Blood Flow

The deployment of an EG likely alters the hemodynamics, which might adversely affect its performance.[139] The clinical significance of the altered hemodynamics needs to be evaluated, with the inclusion of the largest possible number of patients. A step in this process is the comparison of physiological and endovascular repaired blood flow, which is pursued by the current study. [89,140] Combining computational fluid dynamics (CFD) with patient-specific models and statistics, we attempted to define the flow characteristics that deviate significantly from their physiological values after EVAR. The hemodynamic performance of the Endurant® (Medtronic, Santa Rosa, CA, USA) stent-graft system is explored.

*Table 2. Basic geometrical characteristics of the AAAs and specifications of the corresponding EGs in mm.*

| Patient | Age | Lumen diameter | AAA diameter | Main body diameter | Right limb diameter | Left limb diameter |
|---|---|---|---|---|---|---|
| **EN1** | 80 | 37 | 51 | 25 | 16 | 16 |
| **EN2** | 61 | 32 | 52 | 25 | 16 | 16 |
| **EN3** | 75 | 45 | 64 | 28 | 16 | 16 |
| **EN4** | 79 | 43 | 58 | 25 | 20 | 16 |
| **EN5** | 76 | 35 | 53 | 28 | 20 | 16 |
| **EN6** | 75 | 39 | 56 | 36 | 16 | 16 |
| **EN7** | 60 | 39 | 50 | 32 | 20 | 20 |
| **EN8** | 86 | 32 | 51 | 36 | 16 | 20 |
| **EN9** | 68 | 33 | 50 | 25 | 20 | 20 |
| **EN10** | 79 | 42 | 50 | 25 | 20 | 16 |

***Methods***

The computed tomography (CT) scans of ten (10) male patients were obtained before and one month after EVAR by a 16-slices CT system with intravenous injection of contrast agent (0.75-2.0 mm slice thickness, 120KVp, 366 mA). The patients had been suffering from AAA and underwent implantation of an Endurant stent graft system at the University Hospital of Ioannina, Greece. The volume rendering of the AAAs pre- and post-operatively are demonstrated in Figure 14 preoperatively and in Figure 15 postoperatively. The basic geometrical characteristics of the AAAs preoperatively and the specifications of the corresponding EGs are summarized in Table 2. The five healthy abdominal aortas derived

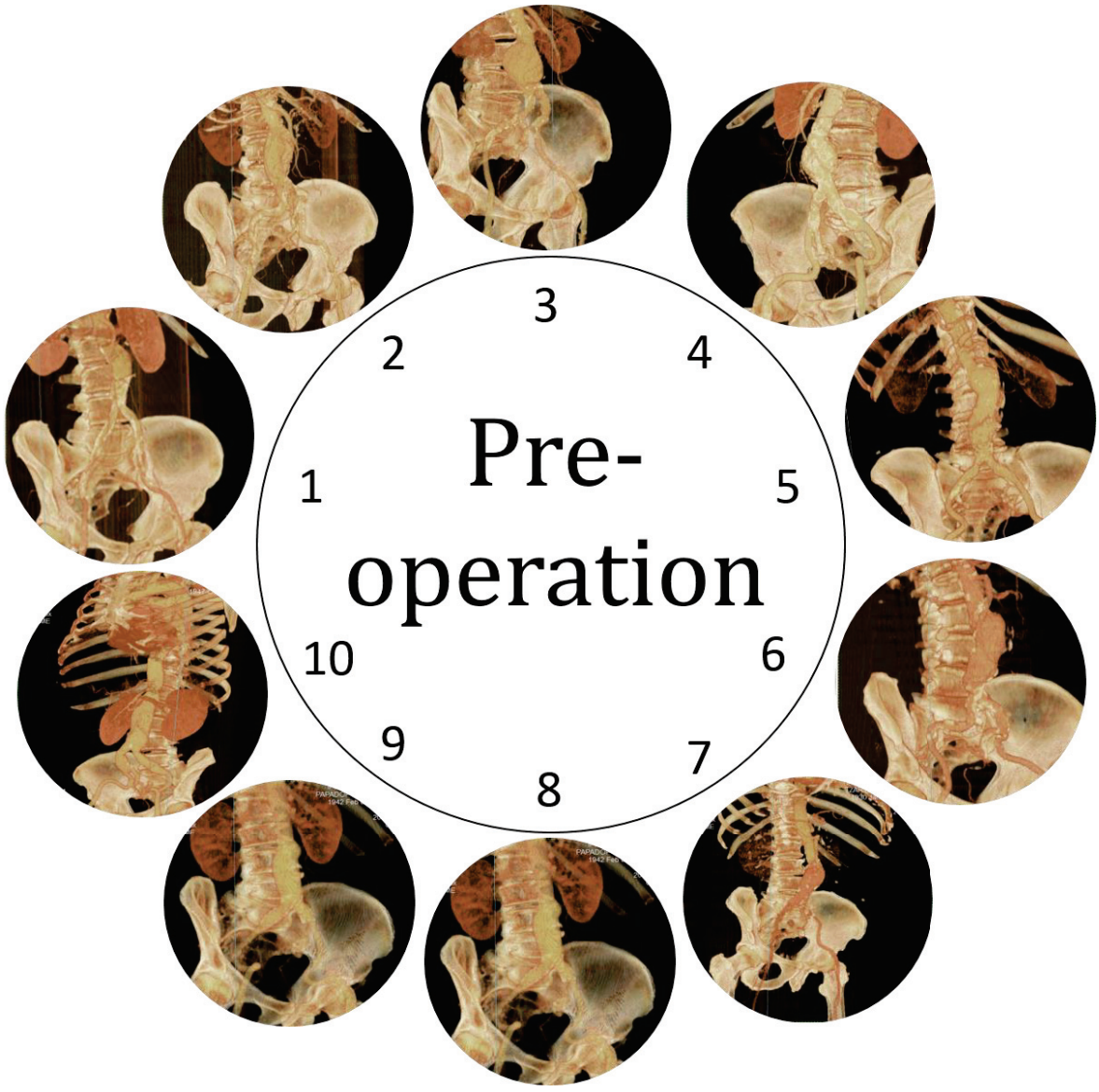


*Figure 14. 3D representation of the AAAs that patients involved in the study had been sufferimg from.*

from male patients that had no sign of aneurysmal disease and underwent CT angiography for an irrelevant reason. Their maximum infrarenal diameter was around 20mm in all cases. The current work has been approved by the ethical committee of the University of Ioannina, and the participants gave written consent for further utilization of their imaging data.

*Modeling*

The geometrical coordinates of the healthy, aneurysmal and repaired abdominal aortas and common iliac arteries were extracted from the CT scans.[141] The parallel two-dimensional DICOM images were converted into three-dimensional models using the image processing and reconstruction software Mimics (Materialise, Leuven, Belgium). The models of the Endurant and Excluder endografts, as positioned in the corresponding AAAs, are displayed for all cases in Figure 16. The models were restricted to the EG interior space (no extension to the suprarenal abdominal aorta or the native iliac arteries) while the preoperative and control models (healthy aortas) included only the lumen between the renal arteries and the iliac bifurcation. Smaller arteries, such as the lumbar and the inferior mesenteric, were not taken into account. The three-dimensional geometries were meshed with tetrahedral elements by the software package ICEM CFD (Ansys Inc., Canonsburg, PA). The meshes consisted of 0.35 to 1.1 million cells. For selected cases, mesh independence tests were carried out. The size of the mesh was successively increased until pressure and velocity were altered less than 2% between the tests.[142] The proper time step size was determined respectively.[78]

The numerical simulations were performed in the software package Ansys Fluent (Ansys Inc., Canonsburg, PA). Blood was considered as a Newtonian fluid with density, $\rho$=1050 Kg/m$^3$and kinematic viscosity, $\nu$ =3.2×10$^{-6}$ m$^2$/s. The unsteady and incompressible blood flow is governed by the coupled non-linear system of continuity and Navier-Stokes partial differential equations:

$$\nabla \cdot \mathbf{u} = 0,$$
$$\frac{\partial \mathbf{u}}{\partial t} + (\mathbf{u} \cdot \nabla)\mathbf{u} - \nu \nabla^2 \mathbf{u} + \frac{1}{\rho} \nabla P = 0,$$

where $\mathbf{u}$ is the velocity vector, $\nu$ is the kinematic viscosity, $\rho$ is the density and $P$ is the blood pressure.

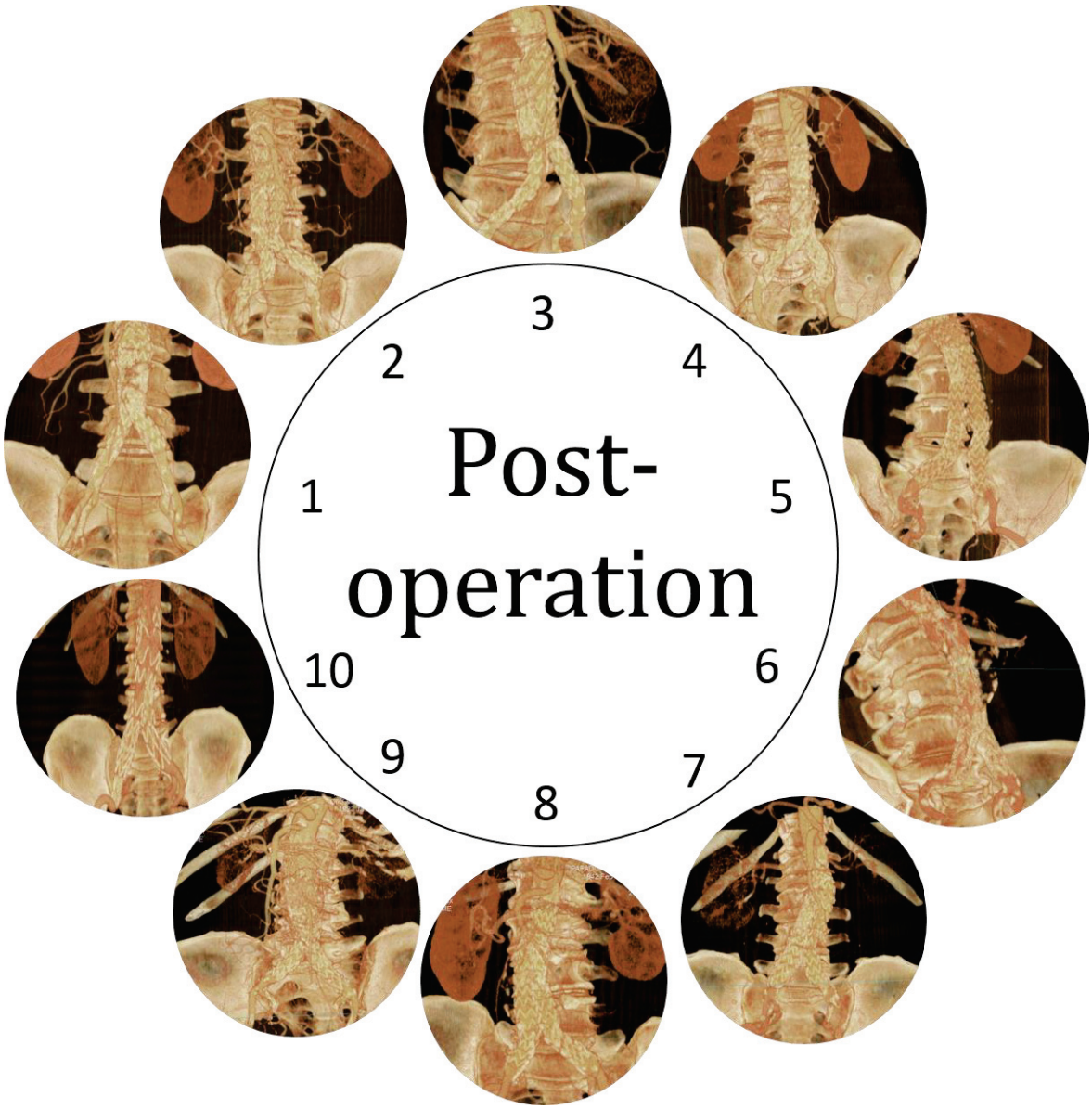


*Figure 15. 3D representation of the stented AAAs one month after EVAR with the Endurant stent-graft system.*

The no-slip condition was applied to the surface of the lumen, following the rigid wall assumption. The boundary conditions at the inlet and the outlets were based on the flow and pressure measurements of Olufsen et al.[143], that were also employed by Xenos et al.[144]. Specifically, at the inlet, a physiological pulse pressure condition was applied in all cases while, at the outlets, the extracted volume output was divided by the variable (among patients) outlet areas, determining the appropriate pulsatile velocity waveforms. Spatially at the outlets, we imposed a parabolic velocity profile that followed the direction of the upstream.

The governing partial differential equations of blood flow are discretized with the Finite

Volume method. The resulting system of algebraic equations is solved in every cell of the mesh. The cardiac cycle was considered to last 0.7s divided into 200 sub-divisions with a fixed time step of $\Delta t = 0.0035s$. A residual error equal to 10-5 determined the achievement of convergence to the solution per time step. The simulations were performed for two cardiac cycles in two Intel Xeon processors (E5645, 2.40GHz, 1 2MB Cache, 5.86GT/s Intel QPI) of a Dell™ Precision™ T7500 workstation. We exclusively utilized the results of the second cardiac cycle avoiding any dynamic disturbances of the numerical solution during the first one. The workflow is summarized in Figure 17.

*Hemodynamic properties and measurement zones*

The properties of blood flow were measured and compared in two regions of interest (ROI): a) the abdominal aorta and b) the iliac arteries. The preoperative models guided the specification of the abdominal and iliac part of the corresponding EG models, as indicated in Figure 18.

The following hemodynamic properties were measured: maximum WSS, pressure drop and maximum velocity at peak systole and mean helicity at mid-diastole. Helicity is a scalar quantity that measures the intensity of helical motion and is defined as the inner product of velocity and vorticity with units of $m/s^2$.[145,146] For the representation of vortical structures, the $\lambda_2$-method was employed. The critical value, $\lambda_{2cr,}$ for the implementation of the method was equal to $-20s^{-2}$, in line with Biasetti et al.[80] According to the method, a vortex develops in a region of the flow around a local minimum pressure. Pressure drop was defined as the difference between the absolute pressure calculated at points intersecting the centerline and the cross-sections that bound the ROI.

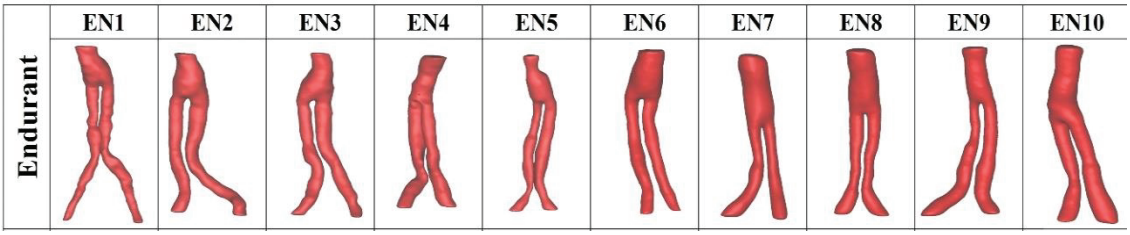


*Figure 16. Models of the Endurant and Excluder models after EVAR that derive from image reconstruction of postoperative CT scans.*

*Statistical analysis*

The hemodynamic data are presented with their mean value (MV) and standard error (SE). The statistical significance of the groups was determined by Student's t-tests, performed in Matlab (MathWorks, Natick, Massachusetts, USA). A value of $p<0.05$ determined statistical significance.

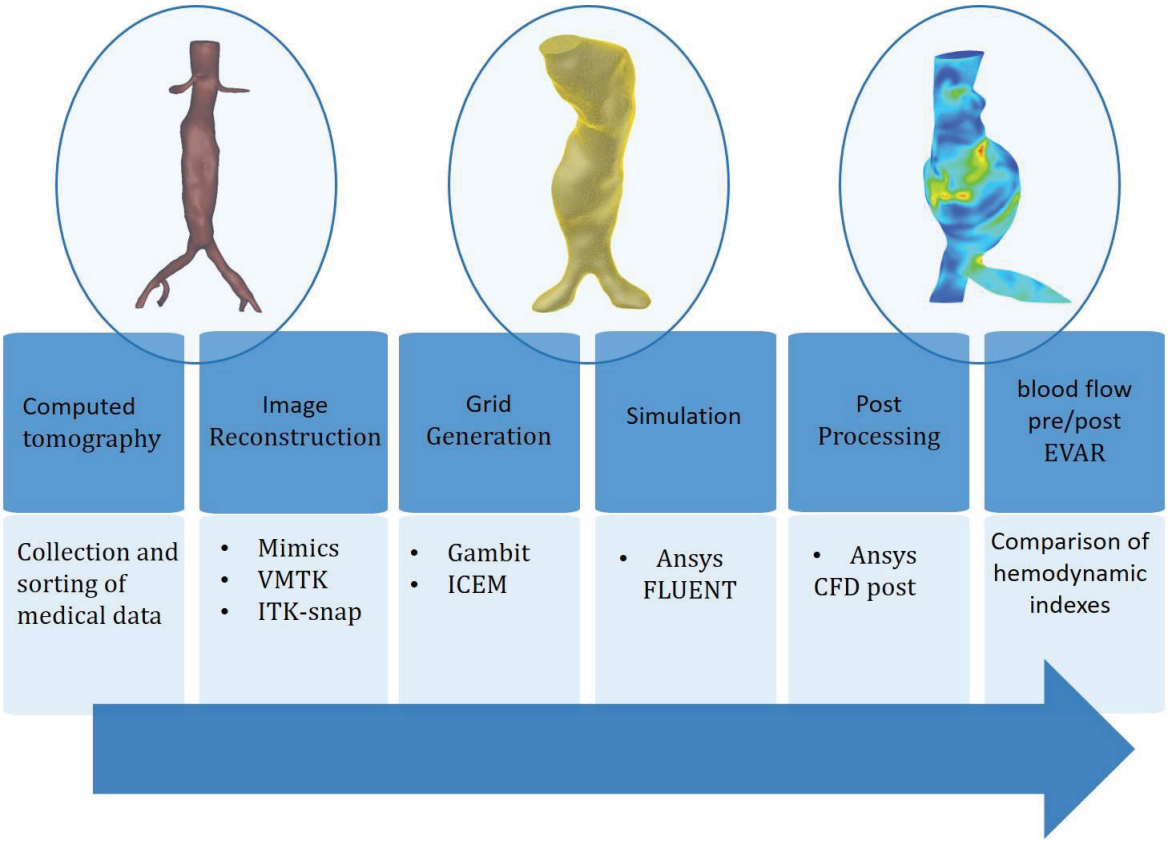


*Figure 17. Graphical representation of the computational workflow that is fed with computed tomography scans and can deliver flow properties in patient-specific AAA geometries.*

## *Results*

*Wall Shear Stress*

The maximum values of WSS at the abdominal aorta and iliac arteries ROI are presented in Figure 19a. Based on the numerical solution, there was an insignificant decrease in maximum WSS at the abdominal part of the EG compared to the physiological value. The calculations however at the iliac part, showed a significant reduction of the maximum postoperative WSS, compared to the physiological value (MV±SE: 8.7±0.5 Pa vs. 16.8±1.4 Pa, $p=0.01$). The contours of WSS, displayed in Figure 20, show that WSS remains high for

the normal cases, whereas lower values with more fluctuations are observed in the stented cases.

*Helicity*

According to the numerical simulations, at the abdominal part of EG, the mean helicity was found to be higher than the normal value, but the variation was not statistically significant, Figure 19b. A concentration of helical structures was observed cephalad to the graft bifurcation, as indicated by the representation of helical structures along with streamlines in indicative stented cases at mid-diastole, Figure 21. At the iliac part of the EG, the intensity of helical flow is close to the physiological measurements, Figure 19b.

*Pressure*

The average postoperative pressure drop, calculated at the abdominal part of the EGs, is lower than the normal value, but the variation was not statistically significant. On the other hand, at the iliac part of the EG, the pressure drop was significantly lower than the average value observed in the physiological iliac arteries (MV±SE: 0.7±0.1 mmHg vs. 2.5±0.4 mmHg, p=0.04). The MV of systolic pressure drop is presented for both groups in Figure 19c. The contours of pressure at peak systole are displayed for representative normal and postoperative cases in Figure 22, indicating the existence of lateral pressure gradients in regions where recirculation zones are located.

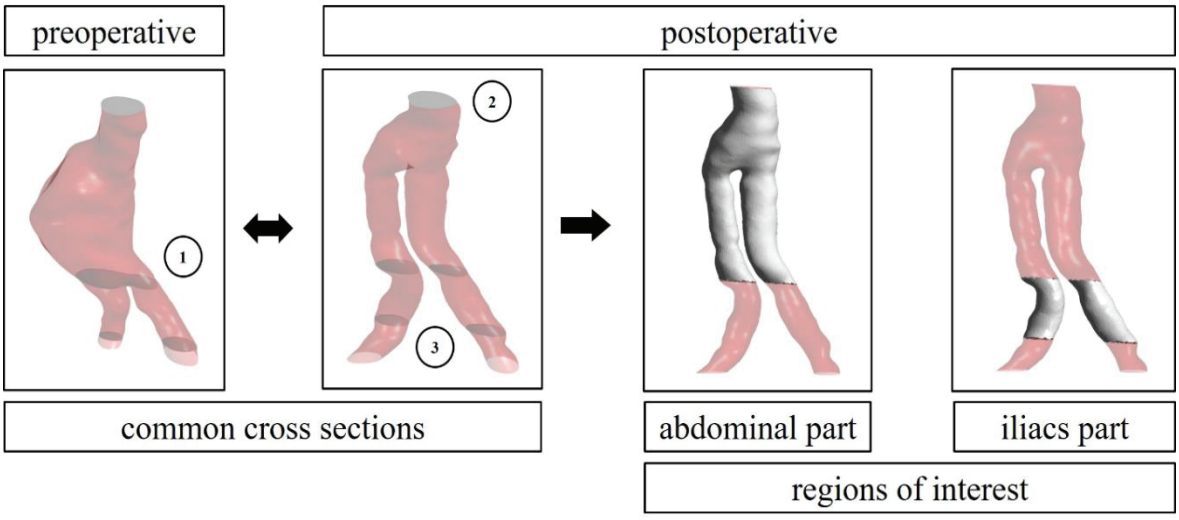


*Figure 18. The specification of ROI in the postoperative models was achieved with the help of the preoperative ones. The cross-section at the aortic bifurcation of a preoperative model is shared with the corresponding postoperative one, separating the regions of the EG that reside in the infrarenal abdominal aorta and iliac arteries.*

*Velocity*

The patient-based simulations revealed that maximum velocity decreases after EVAR. The statistical analysis, however, indicated that the variation between the postoperative and normal values was significant only in the iliac arteries ROI (MV±SE: 0.7±0.02 m/s vs 1.1±0.1 m/s, p=0.04). The average values are presented in the chart of Figure 19d. The streamlines depicted in the left panel of Figure 21, indicate a concentration of recirculation zones prior the EG bifurcation, as mentioned in the helicity results as well.

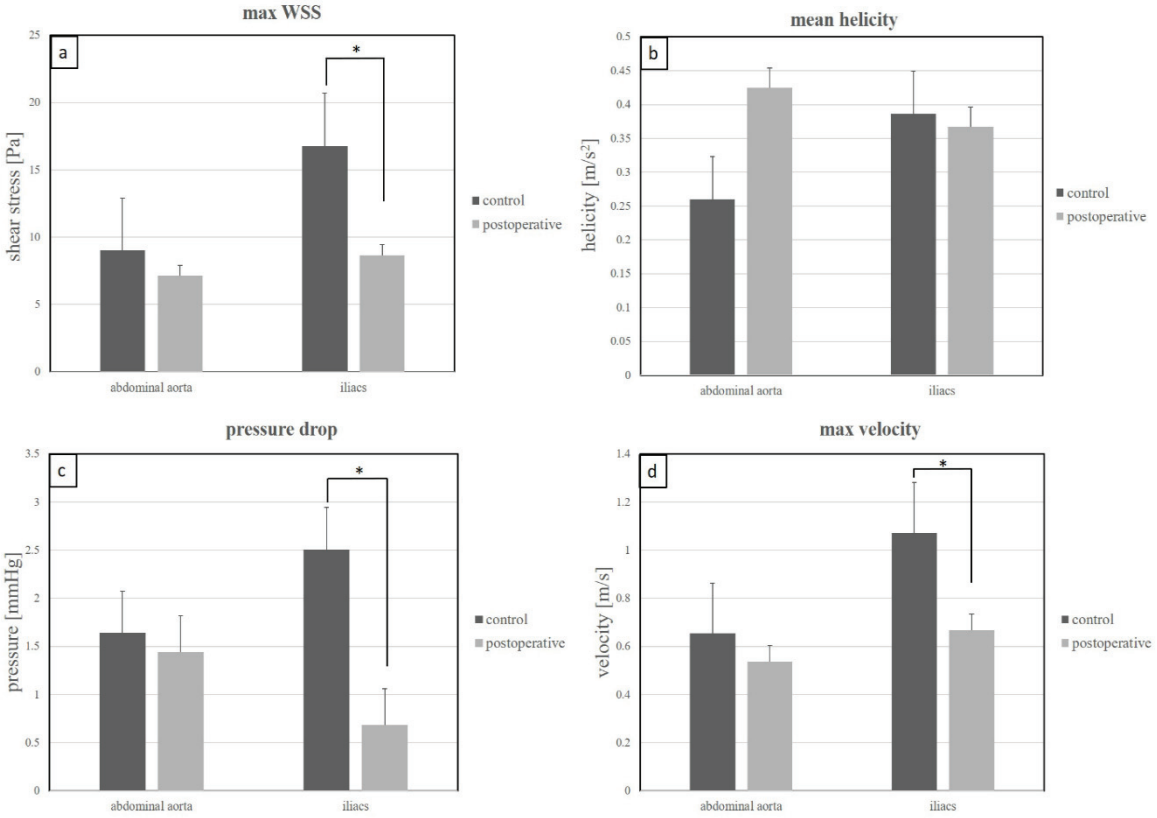


*Figure 19. MV and SE of, a) max WSS, b) mean helicity, c) pressure drop and d) max velocity, calculated in the ROI of the physiological and postoperative cases. The asterisk (*) indicates statistically significant variation (*$p<0.05$*).*

***Discussion***

EVAR is one of the prevailing techniques for dealing with AAAs. Moving towards personalized treatment, a significant milestone is the identification of the hemodynamic impact of commercial EGs. Knowing their hemodynamic features, clinicians could make decisions based on the hemodynamic specifics of each patient. The occurrence of

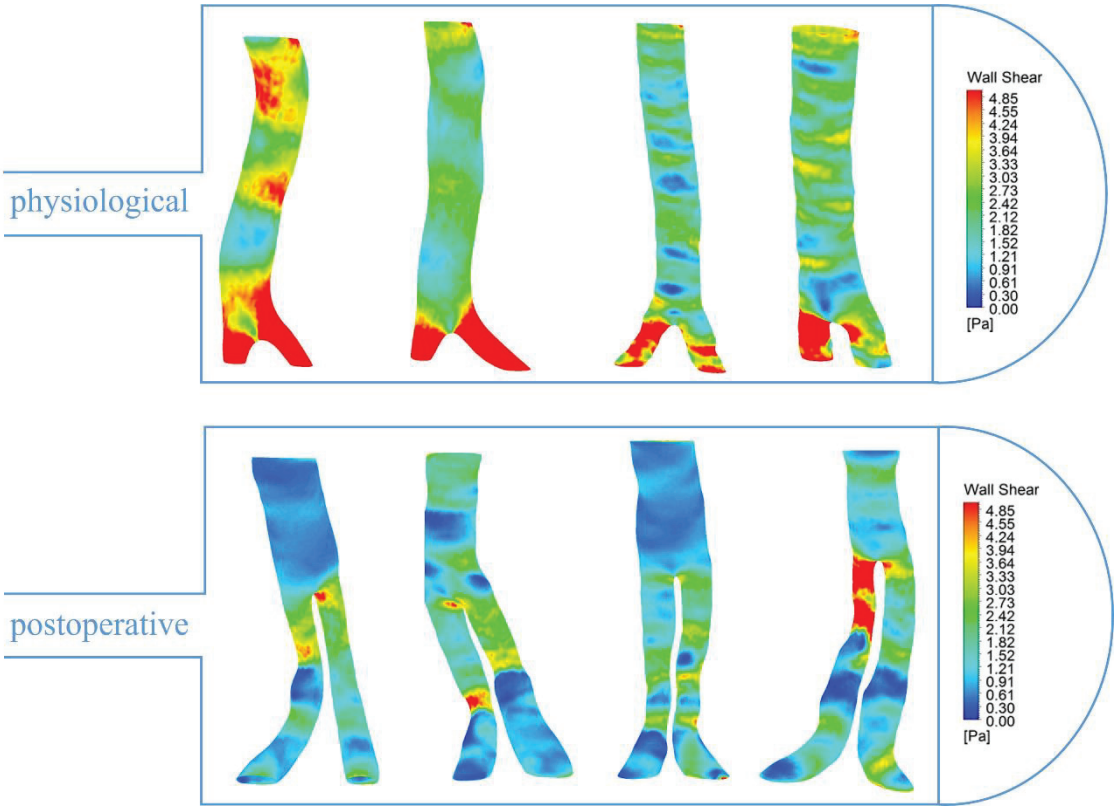


*Figure 20. WSS contours at peak systole for indicative physiological and postoperative cases.*

postoperative complications such as EG migration, endoleaks, limb occlusion, limb thrombosis and repressurization of the sac, might also be associated with the deviation of endovascular repaired from physiological blood flow. To this end, the combination of CFD and medical imaging could unravel underlying processes that experiments are not always able to replicate. The numerical simulations have exponentially increased their impact while being validated by experimental measurements.[83]

Our objective was to test through numerical simulations whether the geometries of endovascular repaired aortas induce significantly altered hemodynamic flow compared to the geometries of healthy aortas. The numerical simulations can be considered as a "computer-generated experiment" that restricts the degrees of freedom to a single parameter,

the complexity of the geometry, justifying the application of common boundary conditions among the cases. The statistical comparison of the hemodynamic indexes could highlight possible disturbances that the lumen remodeling (due to the graft implantation) causes on blood flow. In this direction, Frauenfelder et al.[147] have also taken advantage of CFD

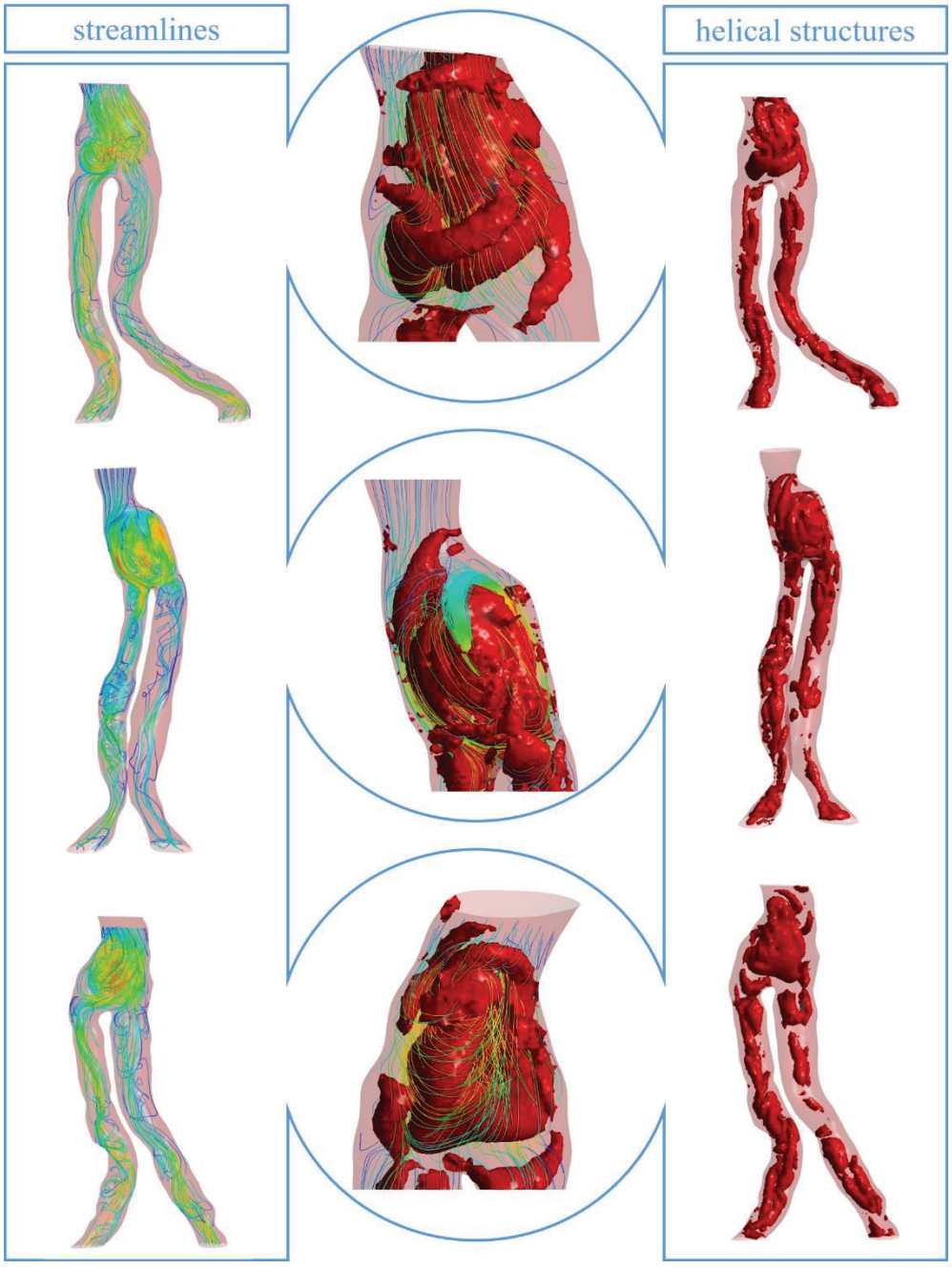


*Figure 21. Streamlines and helical structures at mid-diastole for three representative postoperative cases in the left and right panel respectively. The intense concentration of helical structures and recirculation zones cephalad to the EG bifurcation is depicted in the middle.*

simulations to study blood flow before and after EG implantation. In the present study, we employed additional hemodynamic parameters, performing statistical comparisons between

physiological and postoperative flow data.

The shear stresses, in general, have a rich clinical background. A physiological profile of shear stresses can impede atherogenesis, thrombosis, adhesion of leukocytes, smooth muscle proliferation and endothelial apoptosis.[148] Contrariwise, the parallel action of high and low shear stresses at the aortic wall in connection with irregularities of the lumen geometry, could trigger the activation and consecutively the adhesion of the platelets. The ILT deposition in a major percent of AAAs has been examined through the prism of WSS distribution.[79-81,149] For the context of stented cases, the presence of low shear stresses might lead to in-stent restenosis and possibly limb occlusion that in turn will force the patient to undergo re-intervention.[148] So, the significant deviation of peak shear stresses at the iliac part of the EG is a finding that might have a clinical interpretation, worth to be studied in more depth.

The helical flow, existing in several areas of the arterial and venous systems, has been reported to play an active role in facilitating blood flow transport, suppressing disturbed blood flow, preventing the accumulation of atherogenic low-density lipoproteins on the luminal surfaces of arteries, enhancing oxygen transport from the blood to the arterial wall and reducing the adhesion of blood cells on the arterial surface. For more details, the interested reader could consult the comprehensive review of Liu et. al.[150] The application of $\lambda_2$-method and the estimation of helicity levels offer a quantitative method for the detection of vortical structures. Based on the results, there is an increase of mean helicity in the abdominal part of the EG (but not statistically significant), which might be due to the noticeable concentration of helical structures and recirculation zones before the graft bifurcation.[89] Contrariwise, the measurements indicate that the helical flow is restored in the iliac part, highlighting in this respect the positive reaction of blood flow to the graft implantation.

Pressure drop drives blood flow. Deviation from physiological measurement could lead to disturbed flow. For instance, low pressure drop might be an indicator of the deceleration or even stagnation of blood flow, which has been primarily observed in aneurysmal regions. In our case, the results showed that in the abdominal part of the EG, pressure drop measurements are close to the physiological ones, which is a point in favor of the Endurant® EG. On the other hand, the calculated pressure difference in the iliac part is much lower than the normal one, suggesting that there is room for improvement. A relative conclusion can also be drawn from the velocity measurements, which happen to be lower than the normal ones in the iliac part of the EG as well. Further experimental and clinical studies are

necessary to explore the clinical importance of the present hemodynamic observations.

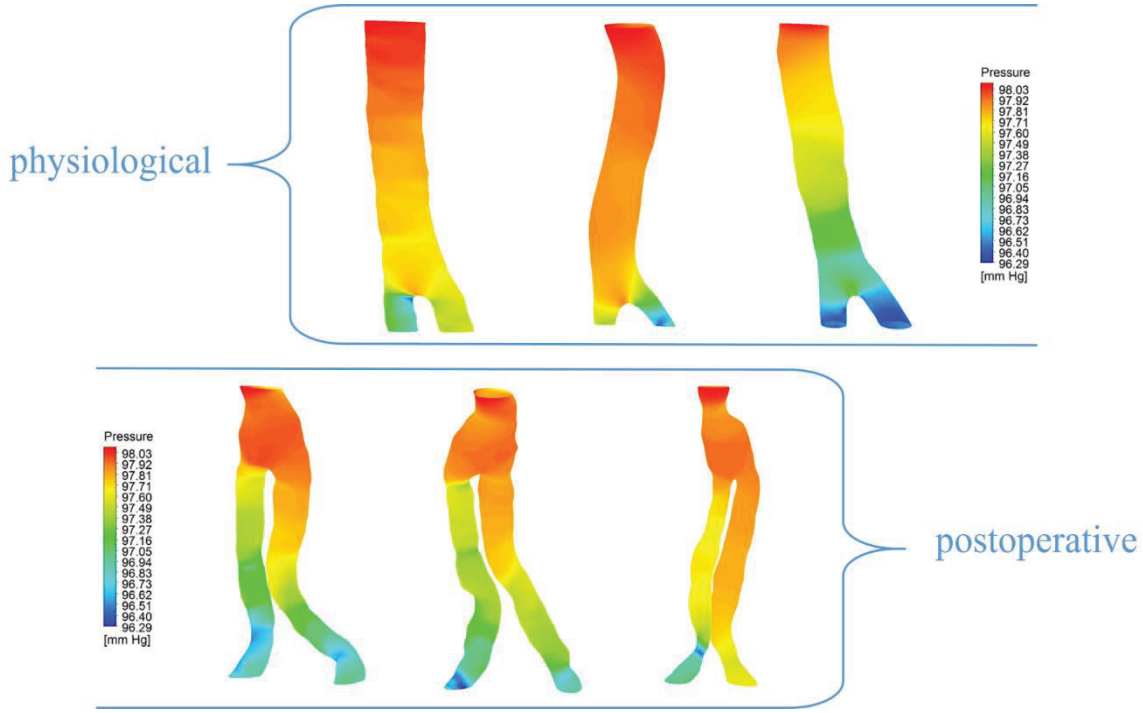


*Figure 22. Pressure contours at peak systole for indicative physiological and postoperative cases. Lateral pressure gradients exist in regions where recirculation zones were detected.*

The elastic properties of the graft material were not taken into account (the surface of the lumen was modeled as rigid). Respectively, the control models did not involve the arterial wall. Even though the patients did not have any sign of insufficient blood supply or unregulated arterial pressure, the application of patient-specific boundary conditions would be more appropriate. Blood could be modeled as a non-Newtonian fluid, separating red blood cells from plasma, which were considered in the current study as a single continuum medium. Finally, the cohort is relatively small (ten patients and five healthy volunteers) limiting our capability to infer undeniable clinical outcomes.

### *Conclusions*

The clinical efficiency of EVAR is proven but it is unknown if blood completely restores to physiological levels. The combination of image reconstructions, CFD and statistics can provide a specific answer to the question from a biomechanical point of view. The applied workflow takes into consideration two factors that are considered to affect the postoperative hemodynamic conditions, the type of the endograft and the patient-specific post-implantation configuration of the endograft. The current study discusses the hemodynamic performance of the Endurant stent-graft system, comparing the postoperative blood flow

indexes to physiological ones, based on a cohort of patients. Blood flow in the part of the Endurant endograft that resides in the pathological infrarenal aorta seems to acquire physiological characteristics while statistical deviations were observed in the iliac limbs. In the main body of Endurant, there is a dense localization of helical structures as proposed by the increased helicity intensity index. The current study paves the way for the more active integration of numerical simulations in the field of endovascular devices. More patients need to be examined to assess clinical implications with more certainty.

## CHAPTER 3

### Endurant vs Excluder

Endurant (Medtronic Vascular, Santa Rosa, CA, USA) and Excluder (W.L. Gore & Associates, Flagstaff, AZ) are reliable EGs with increased levels of safety and effectiveness. Clinicians frequently discuss the role of hemodynamics in the occurrence of complications.[151-153] However, there is not a clear picture about the hemodynamics in the particular EGs. In this Chapter, we defined the flow characteristics that are significantly different between Endurant and Excluder cases. The results derive from twenty patient-based simulations incorporating in the statistical analysis the positioning variability among the EGs. The belief that two EGs with similar commercial specifications probably share common hemodynamic features is questioned.

#### *Methods*

Ten patients with an Endurant EG and ten patients with an Excluder EG were selected from a large cohort. The existence of an infrarenal fusiform AAA, without extension of the disease in the common iliac arteries, had been diagnosed in all cases. The two groups of patients were matched with respect to the following morphological characteristics of the corresponding AAAs: neck length, neck diameter, suprarenal and infrarenal angle, aorta length, right and left iliac length, right and left iliac diameter, neck diameter to right iliac diameter, and neck diameter to left iliac diameter (Table 3). The measurements were carried out in the medical imaging software 3mensio (Pie Medical Imaging BV, Maastricht, The Netherlands).

Endurant and Excluder are both modular bifurcated graft systems with nitinol stents and wires. The former is composed of high-density polyester fabric and the latter of expanded polytetrafluoroethylene. The specifications of the given Endurant and Excluder EGs are reported in Table 4 and 5.

The preoperative and postoperative (one month after surgery) computed tomography (CT) scans had been obtained from a 16-slices CT with intravenous injection of contrast agent (0.75-2.0 mm slice thickness, 120KVp, 366 mA). The protocol and the informed consent were approved by the Institutional Review Board of the University of Ioannina, and all subjects gave informed consent for the use of their screening data.

*Table 3. The morphological characteristics of the AAAs of the patients treated subsequently with Endurant and Excluder endografts (in mm and degrees for angles) were matched between the two groups* (p>0.05)*. The statistical significance was determined with t-tests.*

.

| Anatomical metric | Endurant | Excluder | p-value |
|---|---|---|---|
| Neck length | 20.0±6.0 | 26.6±8.2 | 0.06 |
| Neck diameter | 24.8±3.1 | 22.6±2.1 | 0.09 |
| Infrarenal angle | 21.4±9.0 | 20.5±13.6 | 0.9 |
| Suprarenal angle | 19.5±10.0 | 16.9±8.4 | 0.5 |
| Aorta length | 105.9±16.1 | 117.3±9.3 | 0.07 |
| Right iliac length | 65.9±8.4 | 67.7±16.9 | 0.8 |
| Right iliac diameter | 15.5±2.0 | 13.7±2.0 | 0.06 |
| Neck to right iliac diameter | 1.6±0.3 | 1.7±0.2 | 0.7 |
| Left iliac length | 70.2±9.0 | 70.7±14.7 | 0.9 |
| Left iliac diameter | 14.4±2.2 | 14±2.7 | 0.7 |
| Neck to left iliac diameter | 1.7±0.2 | 1.6±0.2 | 0.4 |

*Modeling*

The two-dimensional DICOM images were converted into three-dimensional models with the software package Mimics (Materialise, Leuven, Belgium). The reconstructions were restricted to the interior of the EG. The surface of the lumen coincides with the surface of the EG postoperatively. However, the thickness or the material properties of the EGs were not taken into account. The three-dimensional geometries were meshed with tetrahedral elements with the software package ICEM (Ansys Inc., Canonsburg, PA). The optimal mesh size was determined by grid independence tests, carried out in regions of expected disturbed flow. Specifically, the mesh was successively being increased until pressure and velocity were altered by less than 2% in the surrounding region of the EG bifurcation.[142]

*Table 4. Geometrical specifications of the implanted Endurant EGs (in mm).*

| Patient | Main body diameter | Right limb diameter | Left limb diameter |
|---|---|---|---|
| EN1 | 25 | 16 | 16 |
| EN2 | 25 | 16 | 16 |
| EN3 | 28 | 16 | 16 |
| EN4 | 25 | 20 | 16 |
| EN5 | 28 | 20 | 16 |
| EN6 | 36 | 16 | 16 |
| EN7 | 32 | 20 | 20 |
| EN8 | 36 | 16 | 20 |
| EN9 | 25 | 20 | 20 |
| EN10 | 25 | 20 | 16 |

The numerical simulations were performed in the software package Ansys Fluent (Ansys Inc., Canonsburg, PA). Blood was considered as a Newtonian fluid with density, $\rho$=1050 Kg/m$^3$, and kinematic viscosity, $\nu = 3.2\times10^{-6}$ m$^2$/s. The no-slip condition was applied to the surface of the EG, following the rigid wall assumption. A physiological pulse pressure condition was employed at the inlet and a physiological flow rate condition was employed at the outlets, as reported by Olufsen et al.[143] A residual error equal to $10^{-5}$ determined the convergence to the solution per time step. A trial simulation showed that two cardiac cycles were sufficient for the elimination of possible dynamic disturbances of the numerical solution.

*Hemodynamic properties and measurement zones*

The following hemodynamic properties were measured: maximum WSS and velocity at peak systole, and mean helicity at mid-diastole. The magnitude of the displacement force was calculated in various time instances throughout the cardiac cycle (the term *magnitude* will be implied in the subsequent references to the displacement force). The displacement force is the combination of pressure and WSS.[20] Helicity is a scalar quantity that measures the

intensity of helical motion, defined as the inner product of velocity and vorticity.[146] For the representation of the helical structures, the $\lambda_2$-method was employed, in accordance with Biasetti et al.[80]

*Table 5. Geometrical specifications of the implanted Excluder EGs (in mm).*

| Patient | Main body diameter | Right limb diameter | Left limb diameter |
|---|---|---|---|
| EX1 | 23 | 16 | 16 |
| EX2 | 28 | 16 | 16 |
| EX3 | 23 | 14 | 14 |
| EX4 | 28 | 14 | 14 |
| EX5 | 28 | 14 | 16 |
| EX6 | 28 | 20 | 20 |
| EX7 | 23 | 20 | 16 |
| EX8 | 23 | 16 | 16 |
| EX9 | 31 | 16 | 16 |
| EX10 | 26 | 14 | 16 |

The hemodynamic properties were evaluated in three regions of interest (ROI): a) part of the main body, 3cm above the EG bifurcation; b) upper part of the limbs, 4cm below the EG bifurcation; and c) lower part of the limbs, 4cm above the ends of the EG (Figure 23). The lengths were defined such that the ROI exist in all cases and do not overlap in each case separately.

*Statistical analysis*

The statistical significance of the hemodynamic variations between the Endurant and Excluder groups was determined by Student's t-tests. The analysis was performed in Matlab (MathWorks, Natick, Massachusetts, USA) and a value of $p<0.05$ was considered to determine statistical significance. The hemodynamic properties are presented with their

mean value (MV) and standard error (SE) for all the ROI in Endurant and Excluder cases in Figure 24.

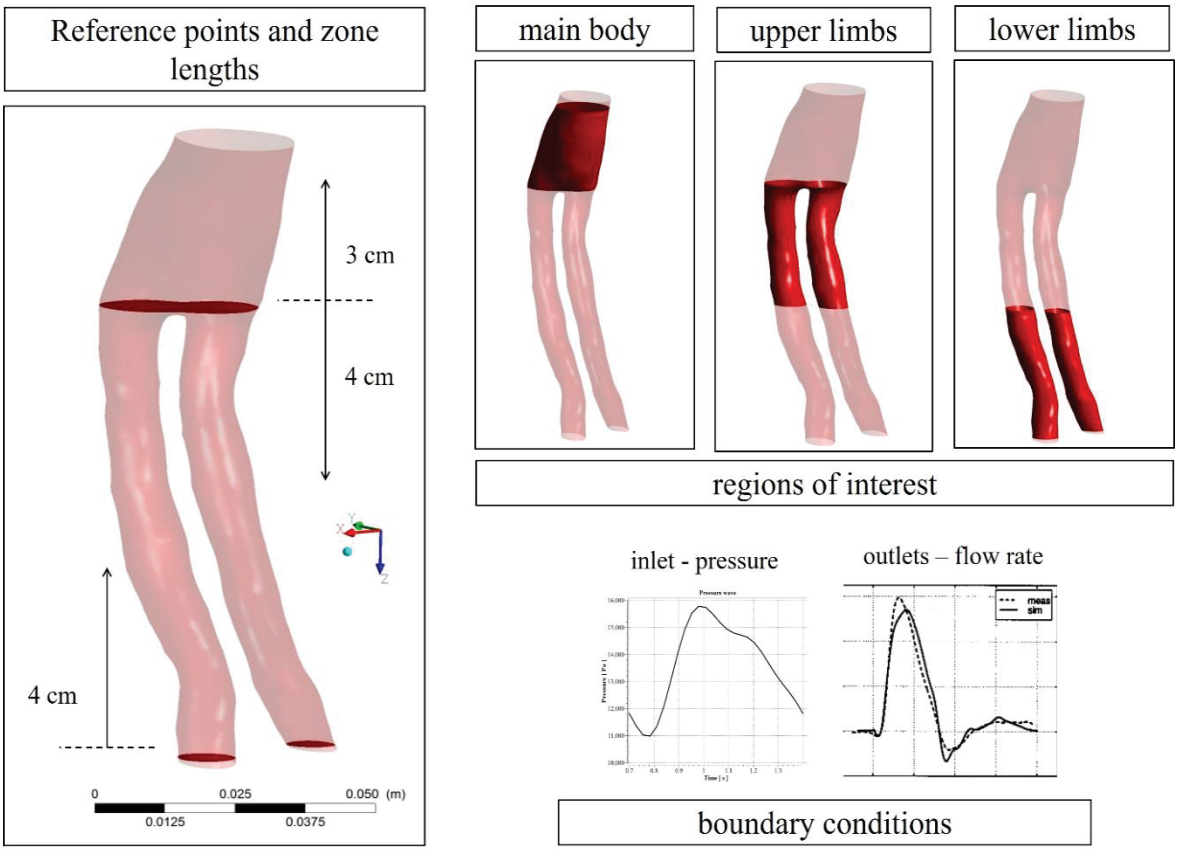


*Figure 23. Schematic definition of the ROI. Part of the main body, 3cm above the bifurcation, the upper part of the limbs, 4cm below the bifurcation and lower part of the limbs, 4cm above the distal end of the EG. Diagrams of pulse pressure and flow rate conditions applied at the inlet and the outlets respectively.*

## ***Results***

### *Wall shear stress*

According to the numerical results, the Excluder generates higher WSS on the main body (MV±SE: 10.8±1.0 Pa vs 4.5±0.2 Pa, p=0.01), the upper part of the limbs (MV±SE: 12.4±0.8 Pa vs 7.3±0.2 Pa, p=0.02) and especially the lower part of the limbs (MV±SE: 17.7±0.5 Pa vs 8±0.5 Pa, p=0.001) compared to Endurant (Figure 24a). The contours of WSS for representative cases highlight the smooth WSS distribution on the Endurant structures (Figure 25). Spatially fluctuating WSS zones were observed below the bifurcation of the Excluder cases, extending along the lower part of the limbs.

*Velocity and helicity*

The variation of maximum blood velocity between Endurant and Excluder cases (Figure 24b) was significant in the main body (MV±SE: 0.4±0.01 m/s vs 0.51±0.01 m/s, p=0.04), the upper part of the limbs (MV±SE: 0.52±0.01 m/s vs 0.68±0.02 m/s, p=0.01) and the lower part of the limbs (MV±SE: 0.66±0.02 m/s vs 1.0±0.02 m/s, p=0.004). The biggest difference of maximum velocity between the two groups occurred in the lower part of the limbs.

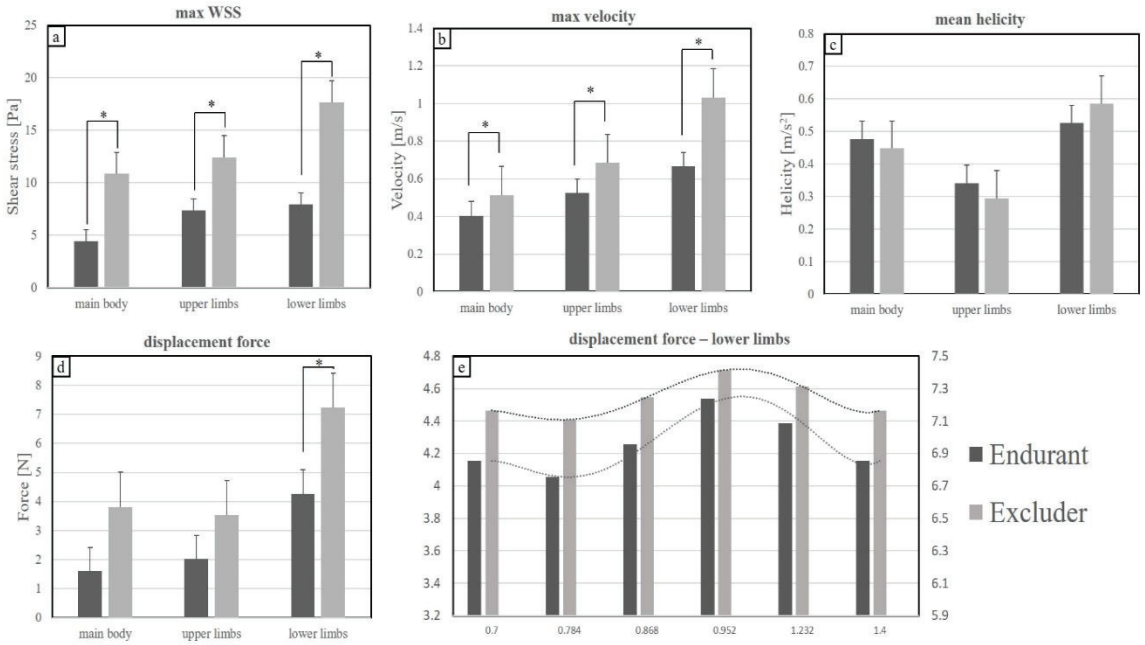


*Figure 24. The mean value and standard error of a) maximum WSS, b) maximum velocity, c) mean helicity and d) displacement forces in all ROI. e) Displacement forces at indicative time instances throughout the cardiac cycle at the lower part of the limbs. The asterisk indicates statistical significance (*$p<0.05$*).*

The projection of velocity in x- and y-direction indicated that there are focal points of secondary flow, mainly in the main body of Endurant and in the limbs of Excluder (Figure 26). The combination of velocity contours and streamlines on a cutting plane for representative Endurant and Excluder cases highlight the development of a larger recirculation zone in the main body of the Endurant compared to the Excluder case, followed by smaller ones in the upper part of the limbs at mid-diastole (Figure 27). The flow in the upper part of the Excluder limbs seems to be more streamlined. At the systolic phase, the flow is streamlined for both EGs.

The intensity of the helical flow is maintained at similar levels in all ROI of Endurant and Excluder cases, as justified by the non-statistically significant variation (Figure 24c).

Helicity was modestly increased in the main body and the upper part of the limbs of Endurant compared to Excluder. The reverse was observed in the lower part of the limbs where Excluder features increased helicity compared to Endurant. The vortical structures that take form in the late systole and propagate during diastole are depicted throughout the cardiac cycle in Figure 28. In the upper part of the Excluder limbs right below the flow divider, there is a zone where helical structures seem to disintegrate but are reintegrated lower at the limbs.

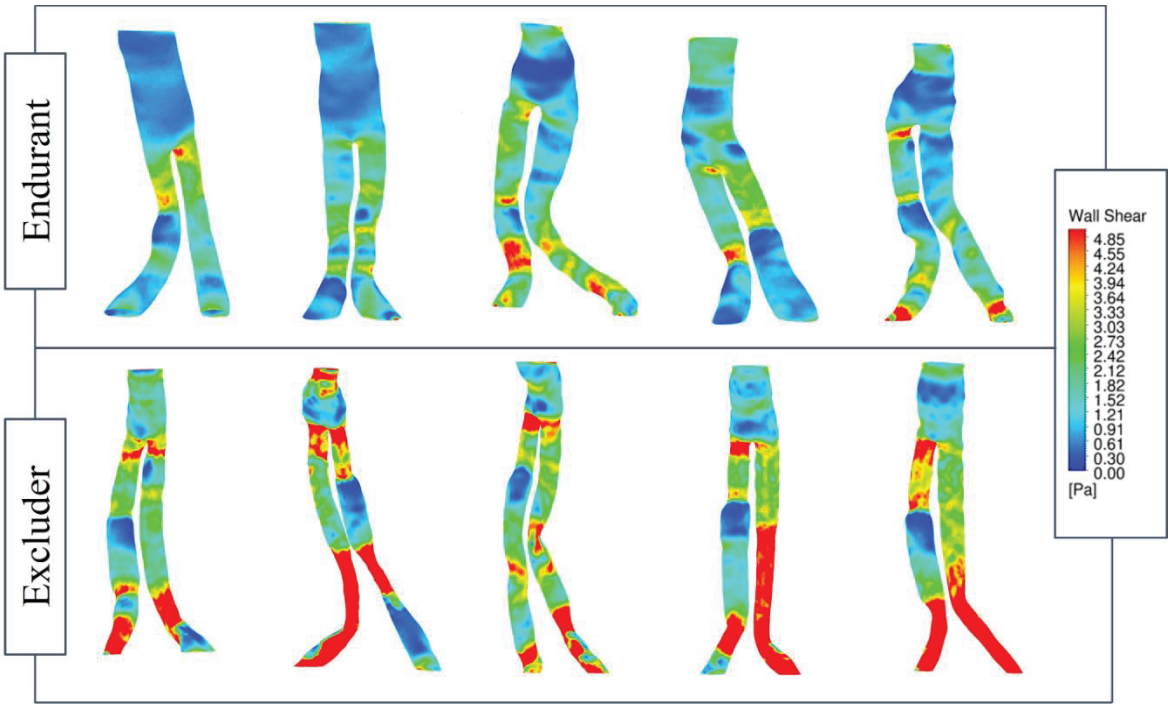


*Figure 25. WSS spatial distribution at peak systole for representative Endurant and Excluder cases.*

*Displacement force*

The variation of the displacement force, acting on Endurant and Excluder models at peak systole, was significant only in the lower part of the limbs (MV±SE: 4.3±1.2 N vs 7.2±0.7 N, p=0.03). For both EGs, the stronger displacement force was found at the lower part of the limbs, compared to the rest ROI (Figure 24d). The displacement force at the lower part of the Endurant and Excluder limbs were calculated in additional time instances throughout the cardiac cycle (Figure 24e), besides peak systole. The results indicated slightly stronger displacement force for the Excluder cases. The variation of displacement force with time, approximated by trend lines for both EGs (Figure 24e), corresponds to the pressure wave during the cardiac cycle (Figure 23).

***Discussion***

The combination of image reconstructions and CFD has boosted the research in the medical field of endovascular therapy.[130] Numerical simulations could assist with minimal resources in identifying the cause of the common complications and in outlining the hemodynamic features of the existing EGs.[5] However, there is a large distance to be covered before a robust numerical tool, qualified for clinical and industrial use, is released. The increase of their reliability can be achieved through validation, escalation of modeling complexity, and close cooperation of engineers and doctors.[86]

In this study, we attempted to delineate the hemodynamic differences between Endurant and Excluder EGs. The two EGs have a similar pre-installation design, but the post-implantation configuration has a direct effect on the blood flow conditions. To this direction,

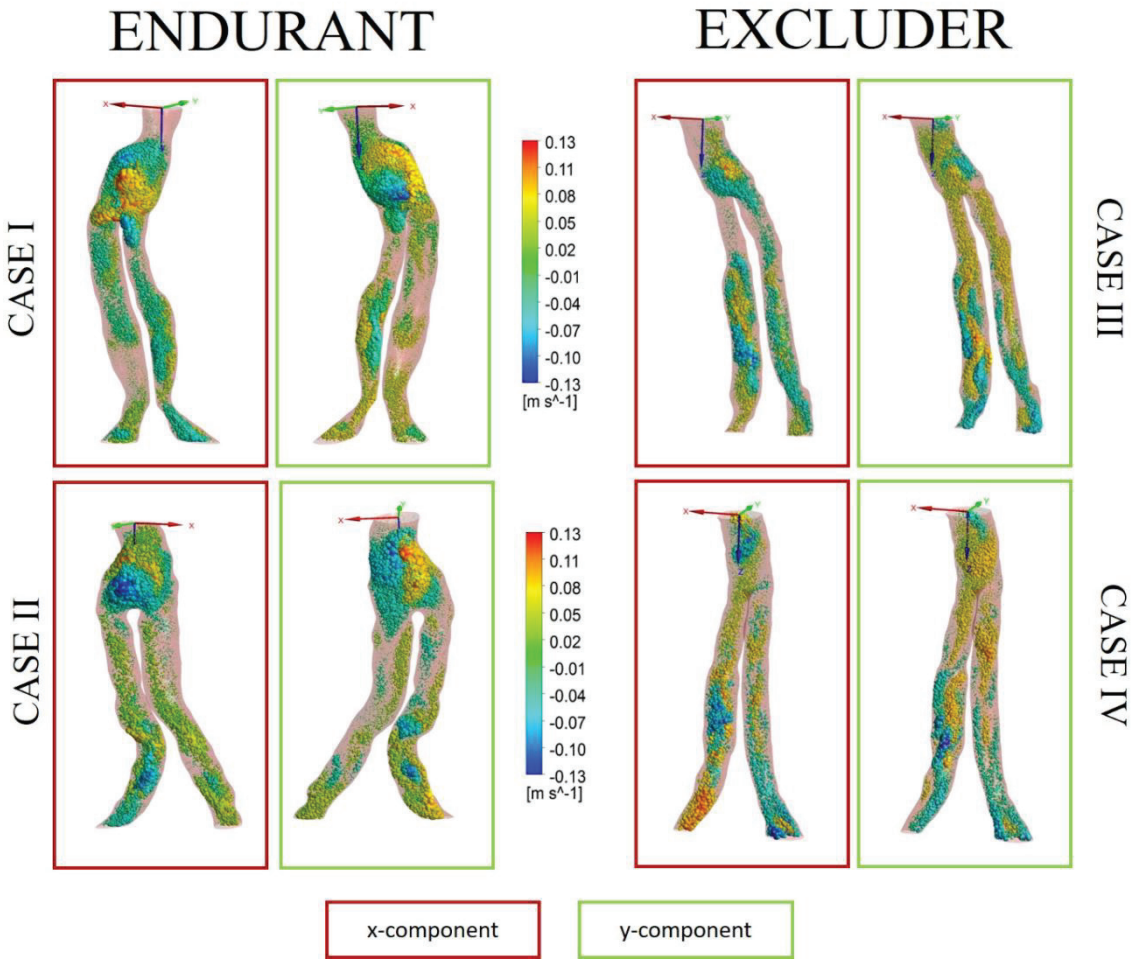


*Figure 26. Focal points of secondary flow at mid-diastole for representative Endurant and Excluder cases. In red boxes, the visualization of the component of velocity in x direction. In green boxes, the visualization of the component of velocity in y-direction. Intense secondary flow in the main body of Endurant and the limbs of Excluder.*

we developed patient-specific models based on postoperative imaging data and not custom models based on commercial characteristics that would not reflect the post-implantation configuration of the EGs. However, an EG adapts to the morphology of the AAA in which it is installed. By taking matched groups with respect to the AAA morphological characteristics, we effectively excluded the effect of AAA morphology and preserved the effect of EG positioning (Table 3). The core idea behind the study was to evaluate the hemodynamic response of two different EGs when installed in similar AAAs.

WSS is suspected of revealing thrombogenicity potential when specific conditions are met. Zones of increased WSS followed by zones of decreased WSS combined with a steep increase of the diameter are considered to promote the initiation of thrombus formation. The platelets might be activated in the former zones and adhere to the local bulge of the latter zones where recirculations possibly develop.[79,94,133] According to the numerical simulations, the Excluder structures reveal such zones (Figure 25), where in one of the two limbs for each representative case, a zone of high (red) WSS succeeds a zone of low (blue) WSS where a local increase of the diameter is apparent. However, it is important to note that the maximum WSS was found to be lower in the Endurant limbs (both upper and lower parts) and that Excluder induces higher blood velocity in all ROI.

The role of helical flow in the human circulatory system, developing primarily in the bigger arteries and veins, is under research. According to the review of Liu et al.[150], helical flow suppresses disturbed blood flow, prevents the accumulation of atherogenic low-density lipoproteins on the luminal surfaces of arteries, enhances oxygen transport from the blood to the arterial wall, and reduces the adhesion of blood cells on the arterial surface. There is, however, evidence of the contrary arising from the migration of red blood cells from the near-wall region, causing a lowering of wall hematocrit.[154] Even though the helicity levels do not vary between Endurant and Excluder, a concentration of helical structures was observed in the main body of Endurant structures, and a reduction of helical structures was observed in the upper part of Excluder limbs (Figure 28).[155] The former observation in connection with the concentration of recirculation zones and the deceleration of blood flow in Endurant was addressed by Nelson et al.[156] as parameters that promote the in-graft accumulation of thrombus.[33] On the other hand, the smaller concentration of recirculation zones in the main body along with the higher velocity, gives the impression that Excluder facilitates blood flow, which might, however, come at the cost of the previous observations, i.e. WSS, forces and helical structures in the upper part of the limbs. Finally, the

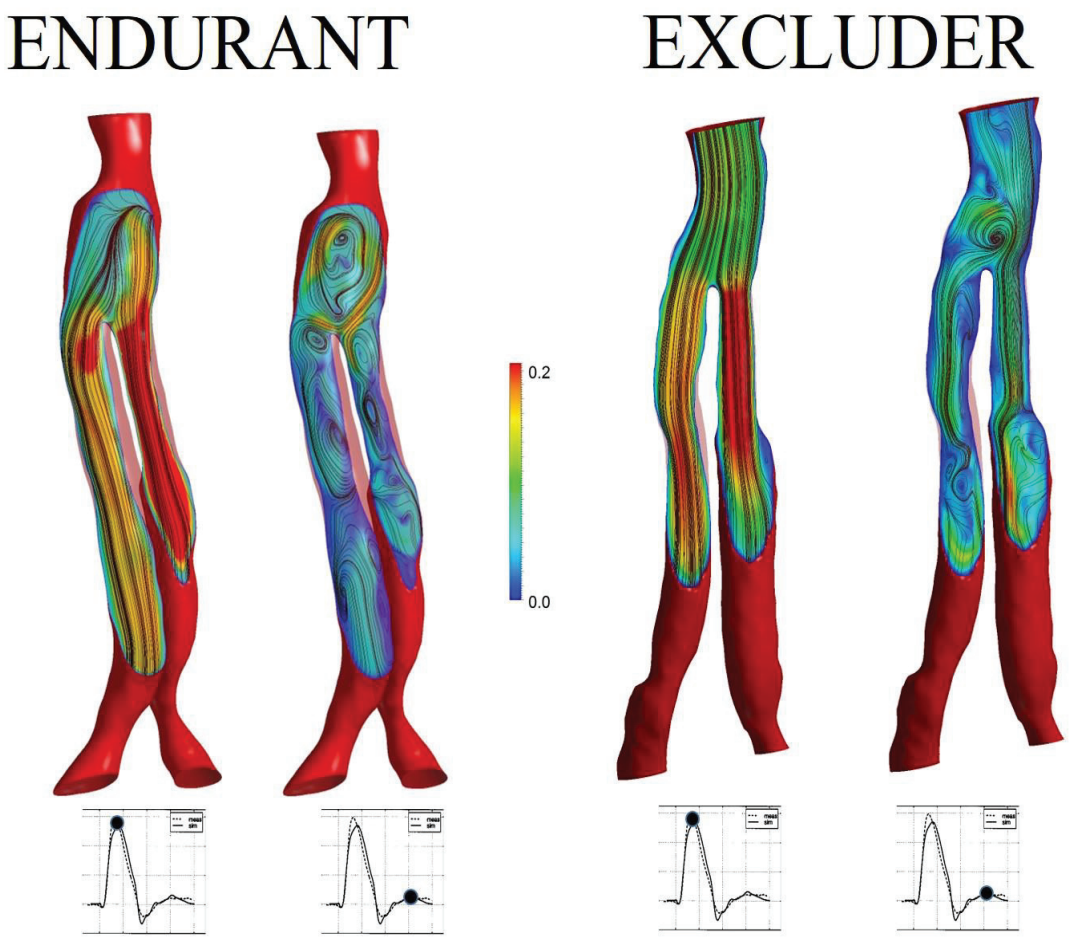


*Figure 27. Contours of velocity magnitude and surface streamlines on a plane for an Endurant and an Excluder case. At peak systole, blood flow is streamlined for both cases. At mid-diastole a larger recirculation zone, followed by smaller ones after the flow division.*

representation of focal points of intense secondary flow (Figure 26) confirms the previous remarks showing that in Endurant, the secondary flow is more intense in the main body while in Excluder, the secondary flow is developing mainly in the limbs.

The displacement forces are possible to predict, EG migration phenomena.[92,93,142,157] In this direction, we reported the forces that apply to the surface of the ROI, comparing them between the Endurant and Excluder postimplantation models. The displacement forces were calculated at peak systole since the forces are essentially the combination of pressure and WSS, the latter being many orders of magnitude smaller than the former. We reported the forces in a dynamic way to show that the forces follow the pressure distribution during the cardiac cycle. The direction of the forces coincided with the direction of the blood mainstream with a minimal deviation between the cases, probably due to the uniformity of the initial morphological characteristics of the aneurysms. Based on the numerical

simulations, the only statistical variation of the forces was observed in the lower part of the limbs that might be of clinical interest.

The current study does not involve the interaction of blood flow with the EG or the arterial wall. The patients did not have any sign of insufficient blood supply, and their arterial pressure was regulated postoperatively. However, the application of patient-based boundary conditions would be preferable. Despite that the Newtonian model is an acceptable approximation of blood flow in large vessels, the non-Newtonian model is more accurate as it captures the dependence of blood viscosity and shear rate. Finally, the sample of patients in this study is relatively small to infer unquestionable clinical implications.

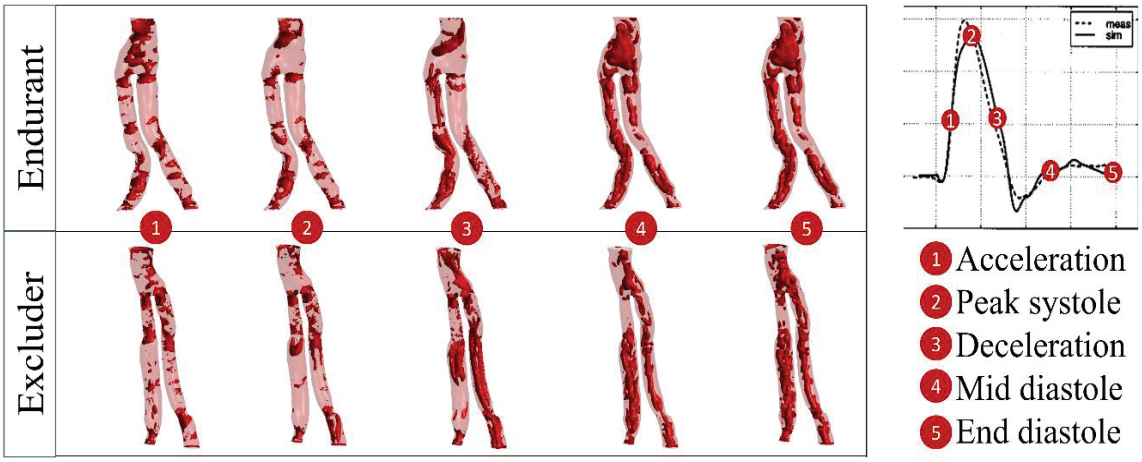


*Figure 28. Evolution of helical structures throughout the cardiac cycle for representative Endurant and Excluder cases. Formation of helical structures during the deceleration phase and propagation during diastole.*

### *Conclusions*

Endurant and Excluder have similar designs; it is, therefore, natural to expect similar flow conditions postoperatively. We introduced a methodology for the identification of hemodynamic differences between EGs, accounting for their positioning variability. There is a lack of a computational study that explores the hemodynamic properties and patterns in the particular EGs. The results showed that the hemodynamic environment might be different, even in similar EGs. Specifically, there were differences mainly in the velocity and WSS and slightly in the displacement forces. The two EGs seem to promote the development of secondary flow and recirculation zones in different regions. The hemodynamic features of the various EGs should be delineated on the way to more personalized treatment.

## CHAPTER 4

### Hemodynamic Performance of AFX and Nellix Endografts

The AFX Endovascular AAA System (Endologix, Inc., Irvine, CA, USA) is the only device that takes advantage of the native aortic bifurcation to achieve fixation. Another unique feature is that the graft is attached to the exterior of the cage with polypropylene sutures only proximally and distally. The graft material, low-porosity ePTFE, is consequently allowed to move independently from the stent cage providing enhanced seal. It is apparent that the AFX endograft introduces mechanical innovations, but its post-implantation hemodynamic performance has not been studied adequately. As the AFX achieves fixation exploiting the native aortic bifurcation, the lumen morphology after the installation of the endograft resembles to a physiological infrarenal aorta, but it is not scientifically proven that the flow conditions are also similar.

The Nellix endograft (Endologix, Inc., Irvine, CA, USA) introduces a novel technology that is different from most commercial endografts. The endovascular sealing technology, which is the formal name of the technology behind Nellix, involves two separately inserted stent-grafts that are supported by polymer-filled endobags (more information are provided in the Introduction section). The Nellix device is a new device and subsequently there no studies in the literature dealing with the hemodynamic environment after the implantation of a Nellix endograft. The postoperative hemodynamics are absolutely related to the morphology of the lumen established as an effect of the endograft lumen remodeling. The numerical simulations can provide a patient-specific picture of the hemodynamics that develop in every cardiac cycle. The optimal value of hemodynamics cannot be explicitly defined but a physiological range of the indexes can be estimated by corresponding numerical simulations in normal infrarenal aortas.

As with the Endurant and Excluder endografts (Chapter 3), there are not computational studies that focus on the hemodynamic aspects of AFX and Nellix endografts after EVAR. The current Chapter deals with the flow conditions in AFX endografts taking into account their post-implantation configuration in the aneurysmal sac of a cohort of patients. The computationally acquired flow properties are statistically compared to normal ones to test the hypothesis that the endografts under research restore blood flow to the physiological levels. The hemodynamic properties and patterns in the endograft structures are visualized to offer a complete picture of the hemodynamics and outline the strong and the weak

hemodynamic points of the particular endografts.

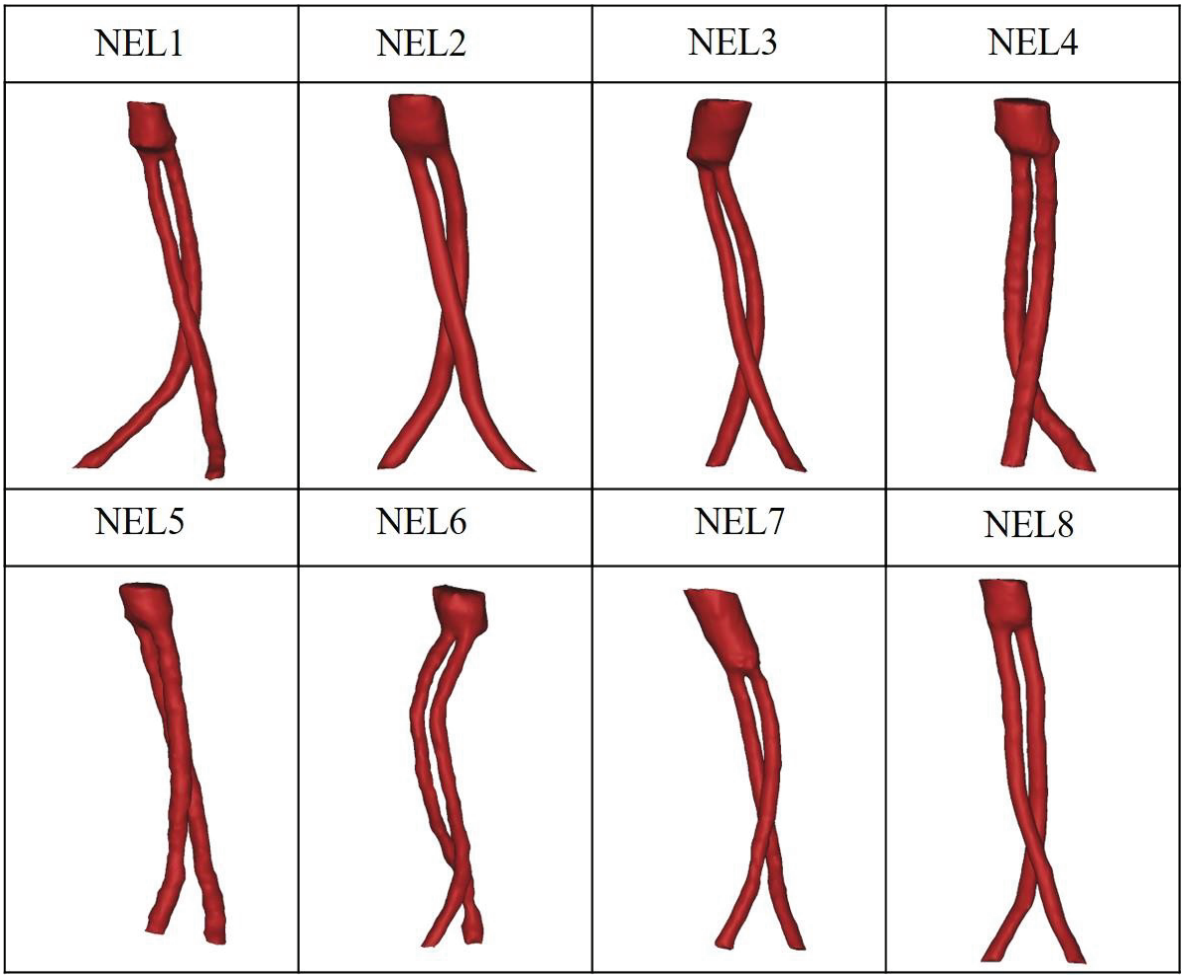


*Figure 29. 3D reconstructed models of all AFX cases. The models reflect the positioning of the endografts in the corresponding aneurysmal sacs.*

***Methods***

The patients were selected retrospectively from a larger cohort so that 8 of the them had been treated with the AFX and 8 of them with the Nellix stent-graft system. The computed tomography (CT) scans of the patients had been obtained before and one month after EVAR by a 16-slices CT system with intravenous injection of contrast agent (0.75-2.0 mm slice thickness, 120KVp, 366 mA) Eligible patients were only those with a fusiform infrarenal AAA. All patients underwent EVAR at the University Hospital of Ioannina.

The morphological characteristics of the AAAs before EVAR were measured with the use of the commercial software 3mensio. The specific anatomical metrics are listed in Table 6 for the patients that were treated with the AFX and in Table 7 for the patients that were

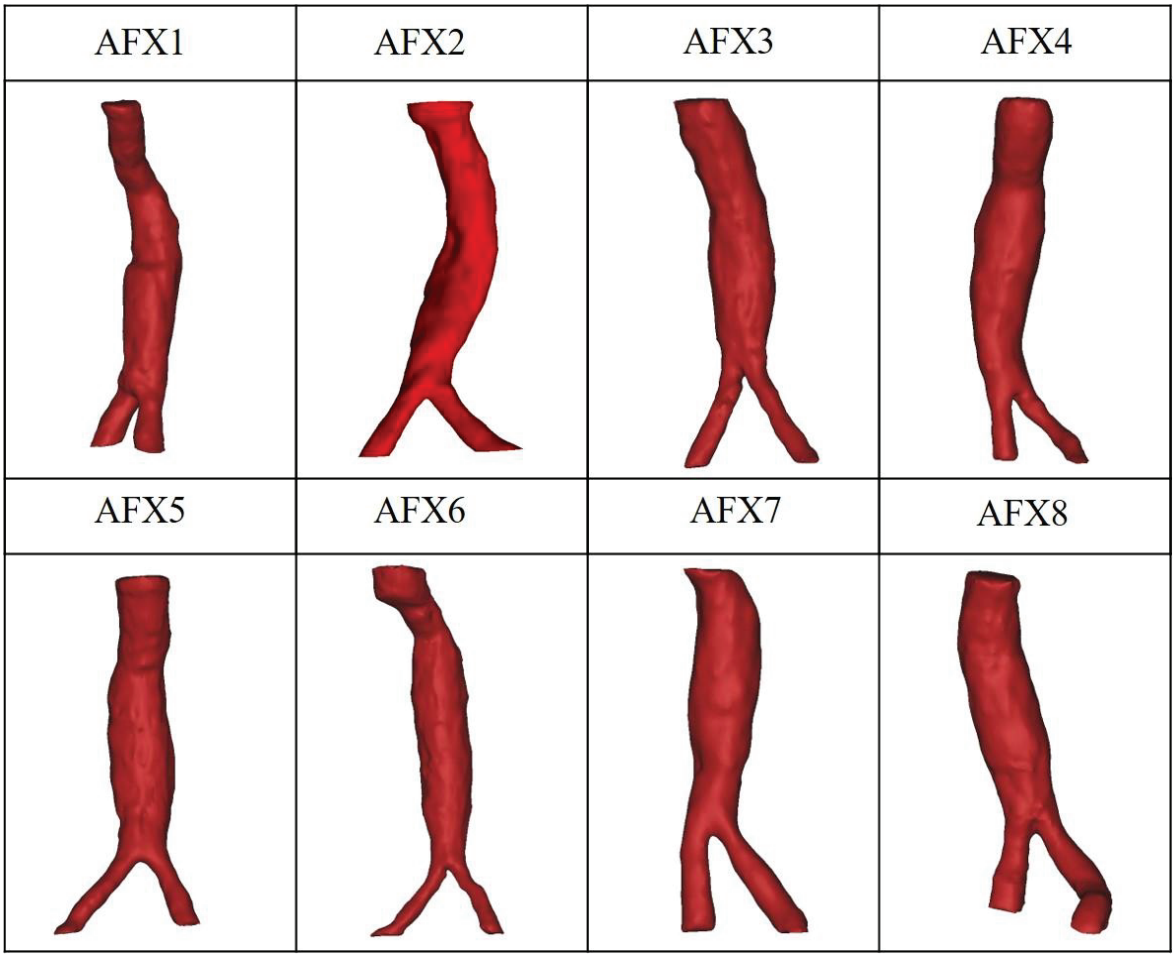


*Figure 30. 3D reconstructed models of all Nellix cases. The models reflect the positioning of the endografts in the corresponding aneurysmal sacs.*

treated with the Nellix endograft. The two groups of patients have matched morphological characteristics of the AAAs, i.e. there was not statistically significant variations between all the anatomical metrics for the two groups as listed in Table 8. The statistical significance was determined with t-tests using the software Matlab. The five (5) physiological infrarenal aortas derive from cases that had a CT scan for irrelevant reason in the University Hospital of Ioannina as well. The normal cases are the same with the ones used in the comparison of physiological and postoperative hemodynamic properties with the use of Endurant endografts in that case (Chapter 2).

The specifications of the AFX endografts that were deemed appropriate for each case by the supervising clinician are summarized in Table 9. There are no varying specifications for the Nellix cases as Nellix has an immutable design (there is only one diameter size available for the stent-grafts, 10mm). The normal cases are the same with the ones employed in Chapter 2.

*Table 6. Preoperative anatomical metrics of the AAAs (in mm and degrees for angles) treated with the AFX stent-graft system.*

| patient | neck length | neck diameter | infrarenal angle | suprarenal angle | right iliac diameter | left iliac diameter |
|---|---|---|---|---|---|---|
| AFX1 | 45.00 | 20.7 | 46.0 | 24.1 | 15.7 | 16.3 |
| AFX2 | 29.00 | 24.2 | 32.8 | 14.2 | 14.0 | 14.6 |
| AFX3 | 32.00 | 24.4 | 29.2 | 10.8 | 12.1 | 13.5 |
| AFX4 | 22.00 | 24.6 | 46.3 | 50.8 | 15.9 | 17.4 |
| AFX5 | 36.00 | 23.6 | 9.7 | 13.5 | 12.1 | 13.2 |
| AFX6 | 20.00 | 22.9 | 25.7 | 6.7 | 11.3 | 11.5 |
| AFX7 | 18.00 | 21.3 | 18.8 | 20.3 | 12.9 | 14.0 |
| AFX8 | 19.00 | 24.3 | 26.1 | 22.5 | 12.6 | 12.1 |

*Modelling*

The two-dimensional DICOM images were converted into three-dimensional models with the software package Mimics (Materialise, Leuven, Belgium). Briefly, a mask is applied in the consecutive slices of the CT axial view. The mask designates the region of interest that the user wants included in the three-dimensional model after the reconstruction. The reconstructions extended from (below) the renal aortas to the distal ends of the endograft thus the models reflect the positioning of the endografts in the aneurysmal sacs. The surface of a model coincides with the graft of the EG. However, the thickness or the material properties of the stent-graft materials were not taken into account which would require a more complex fluid-structure interaction approach that accounts both for hemodynamics and solid mechanics. The three-dimensional geometries were meshed with tetrahedral elements with the software package ICEM CFD (Ansys Inc., Canonsburg, PA). The optimal mesh size was determined by grid independence tests, carried out in regions of expected disturbed flow.

Specifically, the mesh was successively being increased until pressure and velocity were altered by less than 2% in the surrounding area of the EG bifurcation.[142]

The numerical simulations were performed in the software package Ansys Fluent (Ansys Inc., Canonsburg, PA). Blood was considered as a Newtonian fluid with density, $\rho$=1050 Kg/m$^3$, and kinematic viscosity, $\nu = 3.2\times10^{-6}$ m$^2$/s. The no-slip condition was applied to the surface of the EG, following the rigid wall assumption. A physiological pulse pressure condition was applied at the inlet and a physiological flow rate condition was applied at the outlets, as reported by Olufsen et al.[143] A residual error equal to $10^{-5}$ determined the convergence to the solution per time step. A trial simulation showed that two cardiac cycles were sufficient for the elimination of possible dynamic disturbances of the numerical solution.

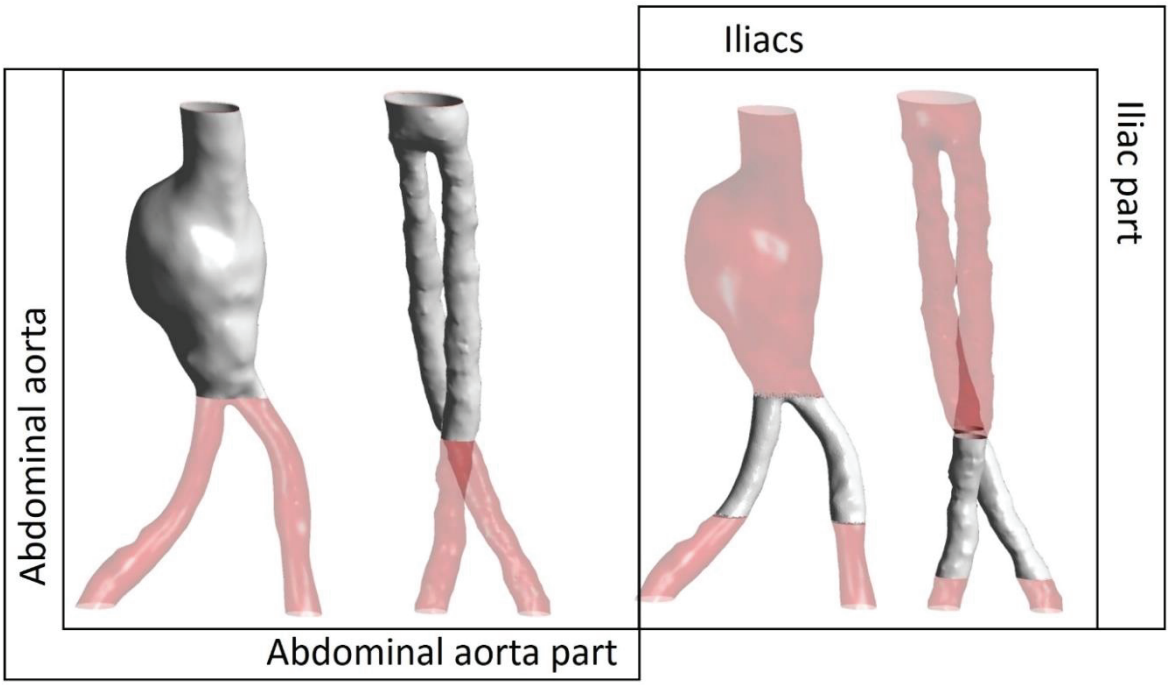


*Figure 31. Definition of the control regions in Nellix cases guided by the preoperative models to distinguish the parts of endografts relying in the infrarenal abdominal aorta and iliac arteries.*

*Measurement zones*

The simulations provide a wealth of hemodynamic data and the post-processing is carried out in the software CFD-Post (Ansys Inc., Canonsburg, PA). The software provides the capability of drawing hemodynamic zones within the control and endograft models and calculate mean or maximum values of hemodynamic properties locally. For the needs of the current study, the endograft models where divided into two regions of interest (ROI): 1) the

part of the endograft that resides in the abdominal aorta below the renal arteries and 2) the part of the endograft that lies in

*Table 7. Preoperative anatomical metrics of the AAAs (in mm and degrees for angles) treated with the Nellix stent-graft system.*

| patient | neck length | neck diameter | infrarenal angle | suprarenal angle | right iliac diameter | left iliac diameter |
|---|---|---|---|---|---|---|
| NEL1 | 13.00 | 20.4 | 41.6 | 8.8 | 16.6 | 12.2 |
| NEL2 | 23.00 | 22.4 | 14.7 | 25.4 | 13.7 | 15.7 |
| NEL3 | 33.10 | 28.0 | 44.1 | 35.5 | 16.5 | 16.5 |
| NEL 4 | 31.10 | 20.9 | 18.5 | 33.1 | 10.9 | 11.1 |
| NEL5 | 35.10 | 23.2 | 16.8 | 35.9 | 13.4 | 12.5 |
| NEL6 | 46.10 | 26.1 | 50.3 | 45.6 | 13.1 | 12.7 |
| NEL7 | 30.00 | 21.9 | 8.5 | 8.5 | 15.3 | 16.1 |
| NEL8 | 11.00 | 23.6 | 11.1 | 15.3 | 10.9 | 9.3 |

the iliac arteries. In this way, the calculated flow properties after EVAR are comparable to the ones measured in the physiological infrarenal aortas and part of the iliac arteries. Regarding AFX, the design of the endograft designates the ROI automatically as it is positioned on the native aortic bifurcation to achieve greater fixity. The control regions in the Nellix systems are not as distinct as in AFX cases so the reconstruction of the corresponding preoperative CT scans was employed to define the extent of the control regions in Nellix cases. Figure 31 shows the control regions in a Nellix case.

*Hemodynamic properties*

The following hemodynamic properties were measured: maximum WSS, pressure drop and maximum velocity at peak systole and mean helicity at mid-diastole. Helicity is a scalar quantity that measures the intensity of helical motion and is defined as the inner product of

velocity and vorticity with units of $m/s^2$.[145,146] For the representation of vortical structures, the $\lambda_2$-method was employed. The critical value, $\lambda_{2cr}$, for the implementation of the method was equal to $-20s^{-2}$, in line with Biasetti et al.[81] According to the method, a vortex develops in a region of the flow around a local minimum pressure. Pressure drop was defined as the difference between the absolute pressure calculated at points intersecting the centreline and the cross-sections that bound the ROI.

*Table 8. The morphological characteristics of the AAAs treated with AFX and Nellix endografts (in mm and degrees for angles) were matched (*p>0.05*).*

| **Anatomical metric** | **AFX** | **Nellix** | **p-value** |
|---|---|---|---|
| Neck length | 27.6±9.6 | 27.8±11.7 | 0.9 |
| Neck diameter | 23.2±1.9 | 23.3±2.6 | 0.9 |
| Infrarenal angle | 29.3±12.5 | 25.7±16.7 | 0.6 |
| Suprarenal angle | 20.4±13.6 | 26.0±13.8 | 0.4 |
| Aorta length | 112.7±16.6 | 115.6±16.5 | 0.7 |
| Right iliac length | 58.6±9.6 | 65.6±11.5 | 0.2 |
| Right iliac diameter | 13.3±1.7 | 13.8±2.2 | 0.6 |
| Neck to right iliac diameter | 1.8±0.3 | 1.7±0.3 | 0.7 |
| Left iliac length | 62.6±7.3 | 62.2±18.1 | 0.9 |
| Left iliac diameter | 14.1±2.0 | 13.2±2.6 | 0.5 |
| Neck to left iliac diameter | 1.7±0.3 | 1.8±0.4 | 0.8 |

*Statistical analysis*

The statistical significance of the hemodynamic variations between the control, AFX and Nellix groups were determined by ANOVA tests. The analysis was performed in Matlab (MathWorks, Natick, Massachusetts, USA) and a value of $p<0.05$ was considered to determine statistical significance. The hemodynamic properties are presented with their

mean value (MV) and standard error (SE) for all the ROI in Endurant and Excluder cases in Figure 32.

***Results***

*Pressure drop*

According to the numerical simulations, mean pressure drop in the physiological infrarenal abdominal aortas was higher compared to the pressure drop in the corresponding parts of AFX and Nellix endografts, Figure 32a. The same applies to the iliac arteries control regions as well. Nellix induces slightly higher pressure drop than AFX in both ROI. However, the variations were not found to be statistically significant.

*Table 9. Geometrical specifications of the AFX endografts (in mm) used to treat the AAA patients, as determined by the clinicians.*

| Patient | Main body diameter | Right limb diameter | Left limb diameter |
|---|---|---|---|
| AFX1 | 25.0 | 16.0 | 16.0 |
| AFX2 | 28.0 | 16.0 | 16.0 |
| AFX3 | 28.0 | 16.0 | 16.0 |
| AFX4 | 28.0 | 16.0 | 20.0 |
| AFX5 | 28.0 | 16.0 | 16.0 |
| AFX6 | 25.0 | 16.0 | 16.0 |
| AFX7 | 25.0 | 16.0 | 16.0 |
| AFX8 | 28.0 | 16.0 | 16.0 |

*Velocity*

In the main body / abdominal aorta (part) control region, Nellix seems to induce slightly higher velocity compared to the physiological and AFX cases. Nellix preserves higher velocity than AFX but the physiological iliac arteries outperform both endograft groups with respect to the induced blood velocity. The velocity results maintain largely the same trend with the pressure drop measurements, but the variations were also not statistically

significant, Figure 32b. To acquire a better understanding of the velocity field, the focal points of secondary flow, i.e. the components of velocity in *x*- and y-directions, are displayed for typical Nellix cases in Figure 33 and for AFX cases in Figure 34. It seems that postoperative configuration of Nellix structures promote a streamlined field of secondary flow along the stent-grafts while in AFX structures, it appears that the focal points are largely concentrated in the upper part of the endograft while before the bifurcation, blood doesn't appear to engage in recirculating paths. It should be noted that the screenshots of secondary flow are captured at mid-diastole where recirculations are expected to develop due to the deceleration experienced by blood at the specific time instance of the cardiac cycle.

*Wall Shear Stress*

Regarding max WSS, the results from the numerical simulations are notified in the chart of Figure 32b. Higher WSS in the abdominal aorta ROI was observed in the Nellix cases, while AFX seems to induce the lowest and the physiological value lies between the two endograft groups. In the iliacs ROI, the physiological value seems surpasses the measurements carried out both in AFX and Nellix cases. The variations between the groups were not statistically significant both in the abdominal and the iliac ROI. The contours of WSS are visualized at peak systole for Nellix and AFX cases in Figure 35. It is apparent that WSS is low on the upper part of AFX post-implantation structures and increases at the lower part, before and after the bifurcations. Regarding Nellix, the profile of WSS maintains uniformity along the stent-grafts, while before the entrance of blood in the endograft, WSS takes its lower magnitude.

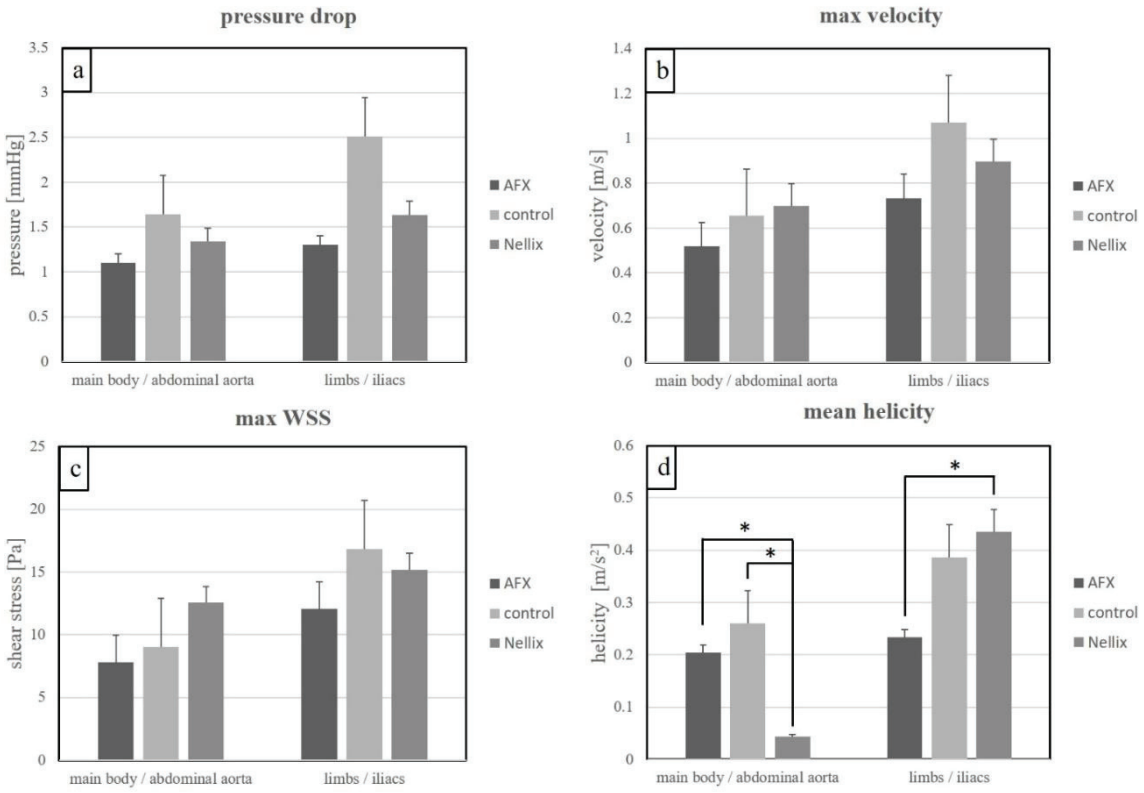


*Figure 32. The MV and SE of a) pressure drop, b) maximum velocity, c) maximum WSS d) mean helicity in all ROI for AFX, control and Nellix cases. The asterisk indicates statistical significance (*$p<0.05$*).*

*Helicity*

The helicity results, obtained from the numerical simulations, are summarized in Figure 32d. The results indicate that Nellix cases were associated with the lowest value of helicity at the abdominal aorta part of the endograft, significantly lower than AFX (MV±SE: 0.04±0.0075 $m/s^2$ vs 0.2±0.02 m/s, p=0.02) and physiological cases (MV±SE: 0.04±0.0075 $m/s^2$ vs 0.26±0.03 m/s, p=0.02). At the limbs/iliacs ROI, the highest mean helicity value of blood flow occurred in the Nellix cases. The variation of helicity levels between AFX and Nellix was statistically significant in the parts of the endografts residing in the corresponding iliac arteries (MV±SE: 0.23±0.008 $m/s^2$ vs 0.44±0.01 m/s, p=0.01), while the physiological value stands between AFX and Nellix mean helicity values, without statistically significant variations. The Figure 36 for AFX cases and the Figure 37 for a Nellix case, display the evolution of helical structures at various key time-instances throughout the cardiac cycle, namely the acceleration, peak-systole, deceleration, mid-diastole and end-diastole phases. It is apparent that the helical structures are mainly localized in the upper part of the AFX structures in agreement with the localization of secondary flow and the low WSS occurring

at the specific part. On the other hand, it seems that flow is not helical before the entrance of blood in the Nellix endograft. The helical patterns at the deceleration, mid-diastole and end-diastole phases, preserve a uniform profile along the whole length of the Nellix endograft.

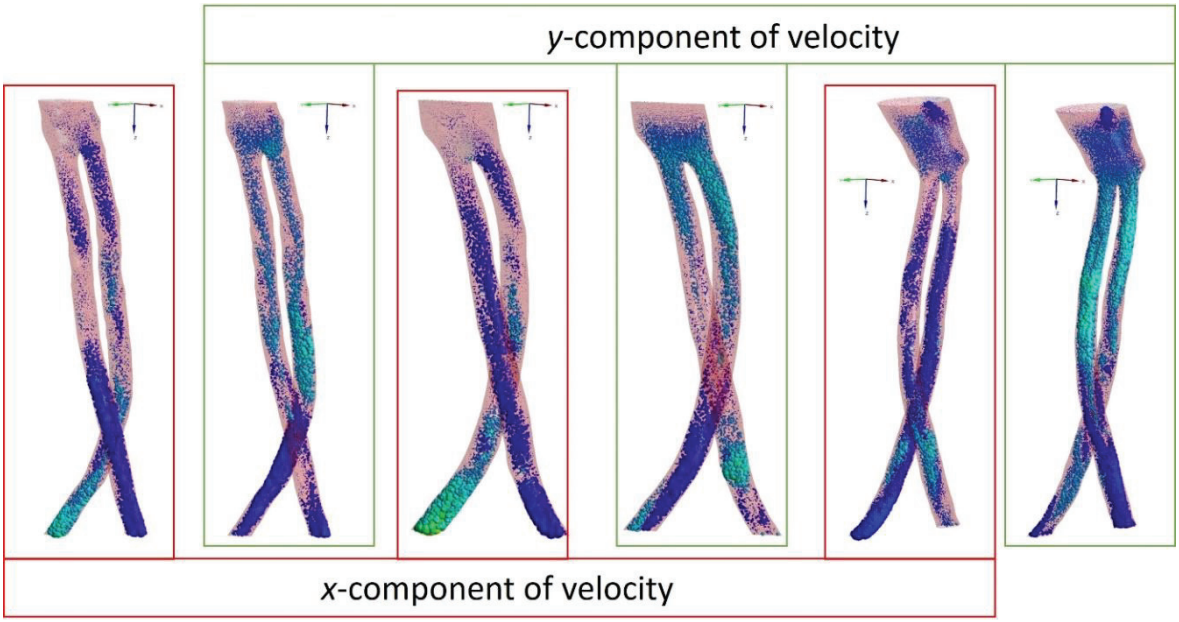


*Figure 33. Focal points of secondary flow at mid-diastole for representative Nellix cases. In red boxes, the visualization of the component of velocity in x direction. In green boxes, the visualization of the component of velocity in y-direction.*

### *Discussion*

In the current study, we focused on two recently available for commercial use endografts, AFX and Nellix, that have more diverse designs that the Endurant and Excluder endografts, employed in the Chapters 2 and 3. AFX and Nellix are the latest iterations of GORE and Endologix respectively. The endograft industries are developing new designs to deal with the long-term device-related complications which are a serious challenge that endovascular therapy is facing in general. The persistence of complications probably limits the clinical benefits that EVAR has over open surgery.[158,159] The short-term clinical outcomes seem to be favorable for both endografts, but there are no long-term data available. More studies are necessary to reach safer conclusions regarding the clinical efficiency of AFX and Nellix.

As the endografts under consideration are new, there are no computational studies in the literature exploring their hemodynamic performance. The current study shares the same methodology with the previous ones, presented in Chapters 2 and 3, at the level of computational modeling, accounting for the post-implantation configuration of the endografts, which is a determinant factor of post-EVAR hemodynamics. The two groups (AFX and Nellix) are matched with respect to the morphological characteristics of the AAAs

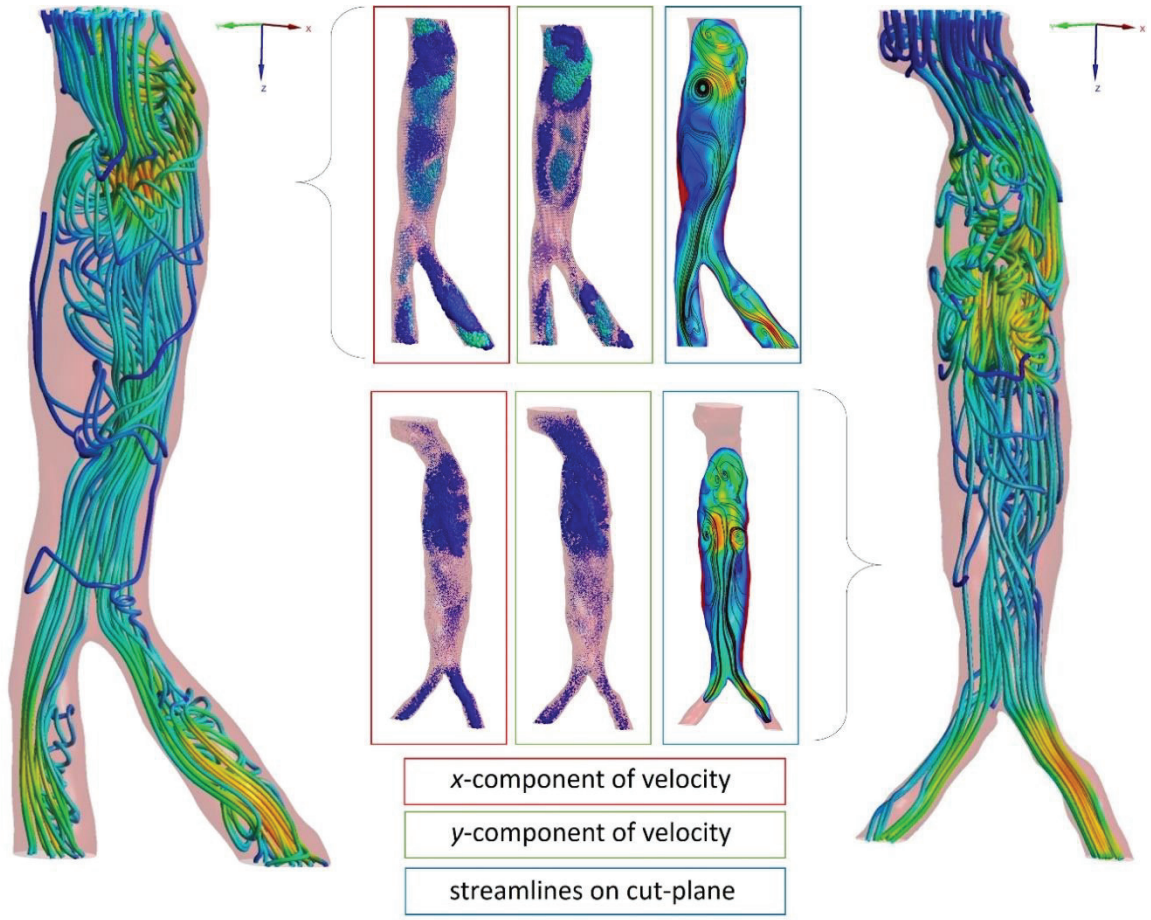


*Figure 34. Velocity streamlines, x-velocity projection (red box), y-velocity projection (green box) and surface streamlines on a cut-plane (blue box) for two (2) representative AFX cases.*

prior to their repair. The patients of each group were chosen such that the morphological variability of the AAAs preoperatively is minimized while the variability of endograft positioning postoperatively is maintained. Our intention was to render the results comparable between the two endografts to give a broader picture of their hemodynamic capabilities. The comparison also includes control data, calculated in physiological infrarenal aortas, to examine if the endografts induce a physiological hemodynamic environment. Despite that the current study cannot infer direct clinical implications, the deviation of a hemodynamic

index from the desired physiological value could be a source of potential clinical instability.

The AFX stent-graft system takes advantage of the native aortic bifurcation achieving stabilization in a physical manner. The postoperative lumen, determined by the post-implantation configuration of the endograft, resembles largely to a physiological infrarenal aorta. However, the resemblance needs to be defined more strictly, in terms of the blood flow restoration levels. The current study was especially designed to provide answers regarding the restoration of blood flow by performing statistical analyses on top of the

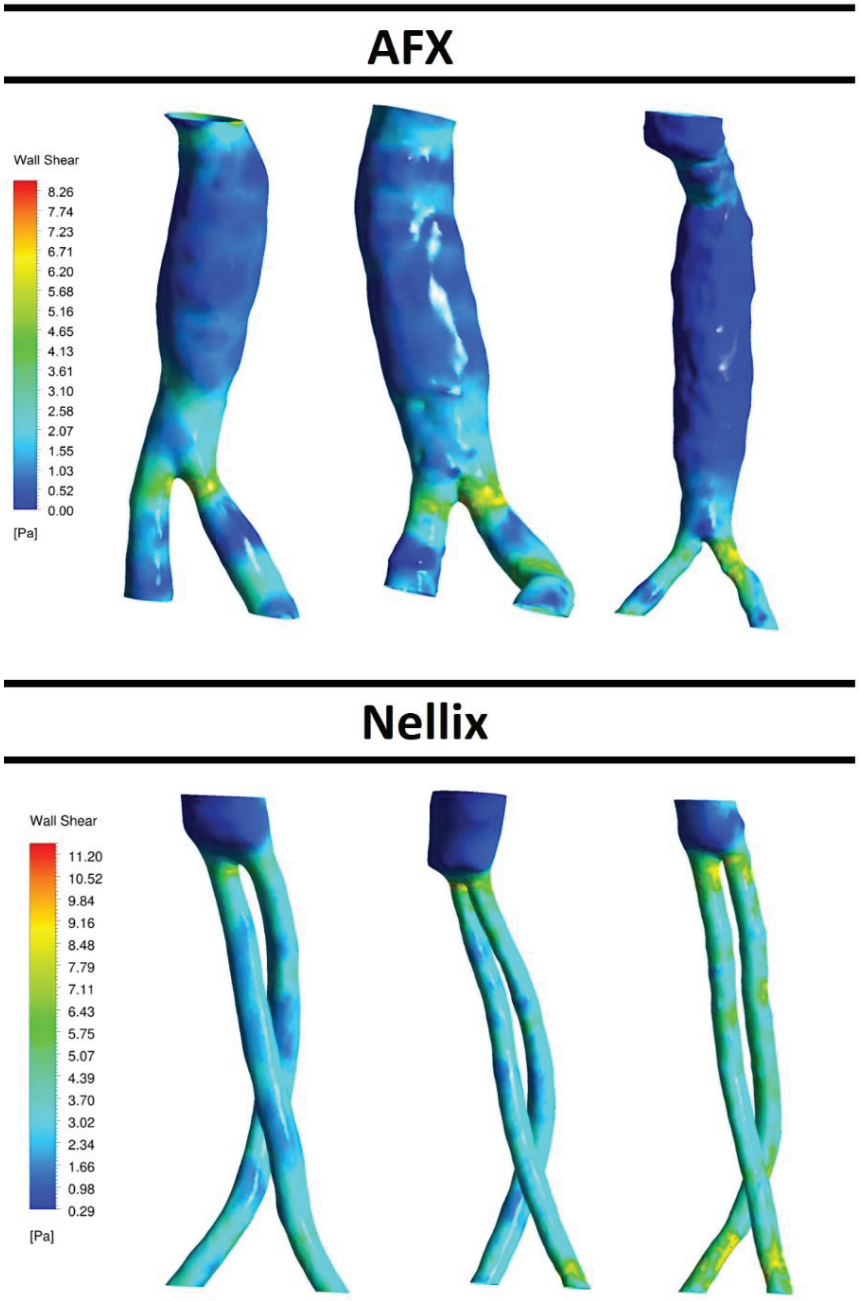


*Figure 35. Contours of WSS for three (3) representative cases for each endograft group (AFX and Nellix) at peak-systole.*

computationally acquired hemodynamic properties. According to the results, the AFX largely restores blood flow to physiological levels as there were no statistically significant variations of pressure drop, velocity and helicity between physiological and AFX cases, Figure 32. On the other hand, it is notable that all calculated properties have lower values than the normal ones in the part of the endograft that resides either in the abdominal aorta or in the iliac arteries, in the part of the endograft that lies in the iliac arteries. Furthermore, the AFX seems to promote the development of secondary flow during diastole at its upper part while in the lower part there was not lateral movement of blood observed in the AFX structures, Figure 34. Both WSS contours (Figure 35) and the localization of helical structures (Figure 36) point to the same direction, i.e. blood seems to engage in recirculating paths at the upper part of the endograft causing a decrease of WSS while the flow is more streamlined in the downstream, accelerating before and after the bifurcation. Despite that the variation of pressure drop was not statistically significant, its mean value in the iliac arteries ROI than the corresponding value revealing that there are margins of improvement AFX could be performing more efficiently with respect to the handling of blood flow in its limbs.

The use of separate stent-grafts supported by polymer-filled endobags is a novelty introduced by the Nellix endograft. The creative endovascular approach applied by Nellix has attracted the interest of medical community while favorable outcomes are being reported in a recent study.[26] The current study is occupied with the hemodynamic performance of

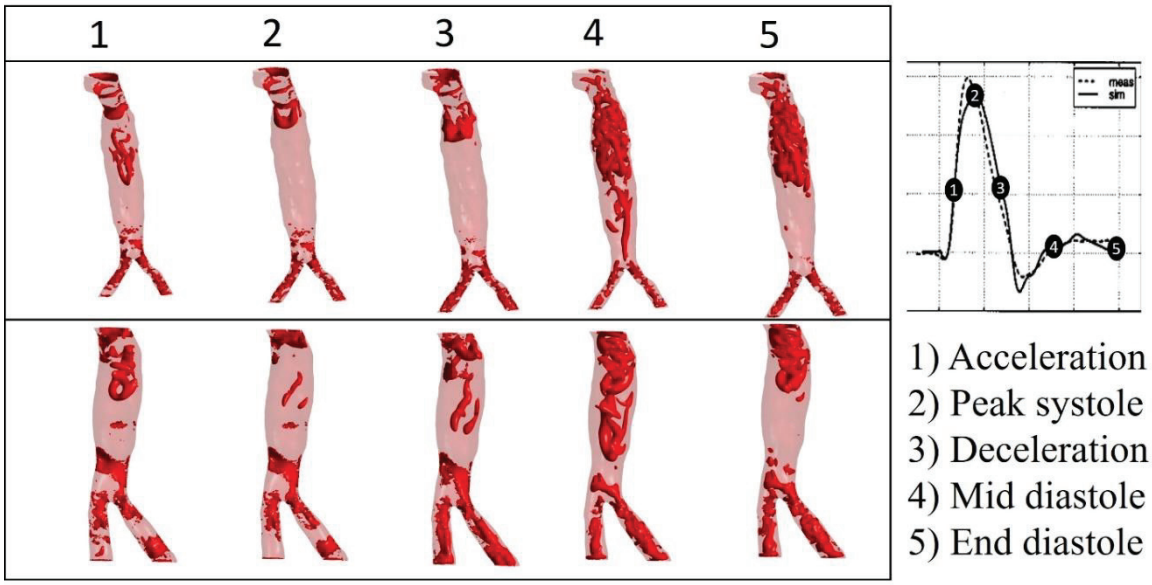


*Figure 36. Evolution of helical structures throughout the cardiac cycle for representative AFX cases. Formation of helical structures during the deceleration phase and propagation during diastole. Concentration of helical structures at the upper part of AFX endograft.*

Nellix using CFD that has not been addressed in the literature. The comparison of the flow properties induced by physiological and Nellix-treated infrarenal aortas can provide detailed results regarding the hemodynamic efficiency of Nellix. Besides mean helicity, the rest calculated flow analytics are not significantly altered compared to the corresponding normal (and therefore desired) ones. Compared to AFX, the numerical simulations showed that the mean values of the Nellix induced flow properties are closer to the mean physiological ones. However, the intensity of helical flow before blood enters the Nellix endograft was significantly different from the mean values calculated in the corresponding infrarenal vascular zone. The helicity value was also significantly lower than the one induced by AFX, a fact that definitely worth further research. It is also notable that in the stent-grafts of Nellix, the helicity value restores to physiological levels with AFX being in this case the endograft that induces the significantly lower helicity value. The spatial distribution of WSS is uniform along Nellix structures, a point clearly in favor of Nellix if the effects of disturbed WSS profiles are taken into consideration. The clinical background of WSS is described in the discussion sections of Chapters 2 and 3, along with the significance of helical flow in the human circulatory system. The representation of helical structures evolution in a Nellix case, Figure 37, shows a uniform development and propagation of helical structures within the stent-grafts of the endovascular device, as a final remark.

The hemodynamic conditions established with the implantation of an endograft are

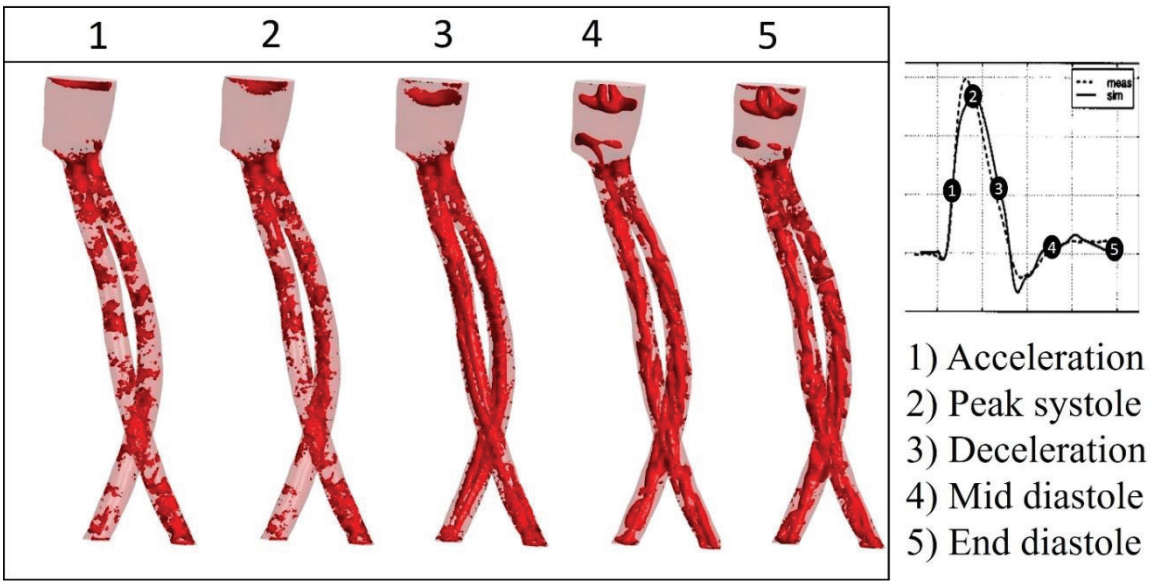


*Figure 37. Evolution of helical structures throughout the cardiac cycle for a representative Nellix case. Streamlined profile of helical structure formation and propagation. Reduced helicity levels before the entrance of the endograft structures.*

experienced by blood in every cardiac cycle and are have therefore special meaning. However, the current computational study cannot infer with certainty clinical implications of a flow property being significantly different from a physiological value. More cases are also required to confirm the trend of the results presented here.

***Conclusions***

The current study addresses the hemodynamic performance of two endografts that have not been adequately studied. Regarding AFX, it seems that the endovascular device achieves absolute restoration of blood flow based on the statistical analysis. However, there are points that need attention such that the development of secondary flow in the upper part of the engraft or the low pressure drop occurring in its limbs. The Nellix endograft seems to be hemodynamic efficient as well, a statement that is agreement with the intuition of vascular surgeons that have experience with the device. According to the simulations, the mean values of most calculated properties are close to the physiological ones. The only concern that seems to have a basis is whether the suppression of helical flow occurring before blood enters the device could potentially have clinical extensions. In any case, more studies are required to address the clinical significance of the flow variations observed between AFX, Nellix and physiological cases.

## FUTURE DIRECTIONS

The potential of the numerical simulations is largely admitted to be unlimited. Our plans involve further exploration of their potential in multiple levels of theory and application. We will move ahead to address as possible the causes that prevent in a global scale the integration of computational simulations in the clinical practice, such as validation issues or the extent of the clinical datasets that are examined computationally. To this direction, we are planning to deploy more advanced computational models that will incorporate both blood flow and arterial wall in unified studies. In our plans, there are also studies that will compare in-vivo and computationally acquired blood flow properties to explore the most efficient balance of modeling complexity and accurate representation of the in-vivo biomechanical environment. As the cost of commercial software is many times prohibitive, we intend to get familiarized and contribute to available open source software which is cost-free, more customizable, produces accurate results and is powered by very active scientific communities globally.

The medical field of vascular and endovascular surgery is expected to be revolutionized in the future with the introduction of computational applications that will help clinicians in the decision making, inform about the risk of vascular diseases, promote more patient-friendly development of endovascular devices limiting the need for human clinical trials and contribute to the research of vascular diseases in general. From our side, we plan to explore the efficiency of novel endovascular approaches for the treatment of aneurysms with the use of fenestrated or branched stent-graft systems that are customized based on the morphological specifics of the patients. It is certain that we will attempt to expand the applicability of numerical simulations in other vascular areas such as the ascending and descending thoracic aortas, the carotid arteries or even in the brain vasculature.

As it is not long ago that computational tools were introduced in the vascular research, their actual capabilities might remain unexplored in a great extent. It is therefore imperative to combine our efforts and work hard to produce cutting-edge research.

**ΠΕΡΙΛΗΨΗ**

Το ανεύρυσμα κοιλιακής αορτής (ΑΚΑ) ορίζεται ως η διαστολή της κοιλιακής αορτής που υπερβαίνει τη φυσιολογική διάμετρο κατά 50% τουλάχιστον και αποτελεί την πιο κοινή μορφή των αορτικών ανευρυσμάτων. Συνήθως τα ΑΚΑ παραμένουν ασυμπτωματικά μέχρι την εμφάνιση μιας πιθανώς θανατηφόρας επιπλοκής δηλαδή της ρήξης. Η ενδαγγειακή αποκατάσταση ανευρύσματος (ΕΑΑ) αποτελεί αξιόπιστη θεραπεία για την ασθένεια, αποκλείοντας τον ανευρυσματικό σάκο και διοχετεύοντας τη ροή του αίματος μέσα από μόσχευμα, που τοποθετείται ενδαγγειακώς.

Η υπολογιστική ρευστομηχανική (ΥΡ) είναι ένα επιστημονικό πεδίο που εμπλέκεται ενεργά στη μελέτη της ροής του αίματος σε όλο το κυκλοφορικό σύστημα. Οι αριθμητικές προσομοιώσεις της ροής του αίματος προσελκύουν το ενδιαφέρον της ιατρικής κοινότητας λόγω του μη επεμβατικού χαρακτήρα τους, των σχετικά χαμηλών οικονομικών απαιτήσεων τους (σε σύγκριση με τα πειράματα), της ευελιξίας τους και της ποσότητας των αιμοδυναμικών δεικτών υψηλής ανάλυσης, που είναι ικανές να παρέχουν. Οι πρόσφατες τεχνολογικές εξελίξεις επιτρέπουν το συνδυασμό της ΥΡ με δεδομένα ιατρικής απεικόνισης, επεκτείνοντας τις εφαρμογές της ΥΡ σε αγγειακά μοντέλα που βασίζονται σε ασθενείς. Οι ερευνητές χρησιμοποιούν την ΥΡ για να μελετήσουν τις πιθανές επιπτώσεις της αιμοδυναμικής ροής στην παθογένεση, εξέλιξη και ρήξη των ΑΚΑ. Οι εφαρμογές της ΥΡ δεν περιορίζονται στη φυσιολογική ή στην παθολογική ροή του αίματος, αλλά μπορούν να χρησιμοποιηθούν επίσης στα πλαίσια της ΕΑΑ.

Στόχος της παρούσης διατριβής είναι να ερευνήσει τις δυνατότητες των αριθμητικών προσομοιώσεων και να θεμελιώσει την εφαρμογή τους σε φυσιολογικές, προεγχειρητικές και μετεγχειρητικές περιπτώσεις των ΑΚΑ. Στο Κεφάλαιο 1 εισάγεται μια εναλλακτική μοντελοποίηση του ενδοαυλικού θρόμβου (ΕΘ), ο οποίος παρατηρείται σε ένα μεγάλο ποσοστό των ΑΚΑ επηρεάζοντας σημαντικά την εξέλιξή τους. Συγκεκριμένα, ο ΕΘ μοντελοποιείται ως πορώδες μέσο με βαθμιαία μικρότερη διαπερατότητα σύμφωνα με ιστολογικές αναλύσεις εξελισσόμενων δομών ΕΘ. Οι διαφορικές εξισώσεις που περιγράφουν την αλληλεπίδραση της παθολογικής ροής του αίματος με τον εξελισσόμενο ΕΘ διακριτοποιούνται με τη μέθοδο των Πεπερασμένων Στοιχείων και επιλύονται σε ένα μοντέλο ΑΚΑ με τη χρήση λογισμικού που αναπτύχθηκε για τις ανάγκες του προβλήματος. Η ανάλυση των επιπτώσεων του ΕΘ στις συνθήκες της αιματικής ροής σε ΑΚΑ είναι σε συμφωνία με τους εμβιομηχανικούς παράγοντες που προωθούν τη γέννηση και την

ανάπτυξη του ΕΘ.

Η βιβλιογραφία αναφέρει ότι το ποσοστό των επιπλοκών μετά από ΕΑΑ μεταβάλλεται μεταξύ των εμπορικών μοσχευμάτων, ωστόσο υπάρχουν ελάχιστες κλινικές, υπολογιστικές ή πειραματικές μελέτες, που παρέχουν αιμοδυναμικά δεδομένα για τα διάφορα μοσχεύματα χωριστά. Επιπλέον, είναι γνωστό ότι η εμφύτευση ενός μοσχεύματος μεταβάλλει την αιμοδυναμική ροή με πιθανές αρνητικές επιπτώσεις στη λειτουργικότητα της ίδιας της συσκευής, παρόλα αυτά δεν υπάρχει μια συνεπής μεθοδολογία για τον υπολογισμό των συγκεκριμένων μεταβολών των ιδιοτήτων της ροής του αίματος. Στα Κεφάλαια 2,3 και 4 δίνεται απάντηση σε ανοιχτά ερωτήματα σχετικά με την αιμοδυναμική απόδοση της ΕΑΑ και διερευνάται το αιμοδυναμικό προφίλ των διαφόρων εμπορικών μοσχευμάτων με τη χρήση προηγμένων τρισδιάστατων δυναμικών αριθμητικών προσομοιώσεων, που βασίζονται σε ιατρικά δεδομένα. Η μεθοδολογία περιλαμβάνει: 1) τη συλλογή των κατάλληλων ιατρικών υποθέσεων, 2) την αναδόμηση ιατρικών απεικονίσεων από αξονικές τομογραφίες ασθενών για την εξαγωγή της εξατομικευμένης γεωμετρικής αναπαράστασης των αγγειακών δομών προεγχειρητικά και των δομών των μοσχευμάτων μετά από ΕΑΑ, 3) τη δημιουργία αριθμητικών πλεγμάτων ώστε να καταστεί δυνατή η εξαγωγή υψηλής ανάλυσης αιμοδυναμικών ιδιοτήτων, 4) την εκτέλεση αριθμητικών προσομοιώσεων YP, 5) την επεξεργασία των αποτελεσμάτων με έμφαση στις περιοχές ενδιαφέροντος εντός των μοντέλων, 6) την οπτικοποίηση των αιμοδυναμικών ιδιοτήτων και μοτίβων και 7) τη στατιστική ανάλυση για να προσδιοριστεί η σημασία των μεταβολών των αιμοδυναμικών ιδιοτήτων.

Η ΕΑΑ έχει ευνοϊκά βραχυχρόνια αποτελέσματα και αποδεδειγμένη κλινική αποτελεσματικότητα, αλλά δεν έχει μελετηθεί επαρκώς αν η ροή του αίματος αποκαθίσταται πλήρως μετά από την εμφύτευση ενός μοσχεύματος. Στο Κεφάλαιο 2 μελετάμε τις μεταβολές της αιματικής ροής σε υγιείς και ενδοαγγειακώς επισκευασμένες υπονεφρικές αορτές. Στο Κεφάλαιο 3 εφαρμόζουμε τη μεθοδολογία που αναπτύχθηκε για να εξετάσουμε την υπόθεση, ότι δύο (2) μοσχεύματα με παρόμοιο σχεδιασμό, το Endurant και το Excluder, επάγουν παρόμοιο αιμοδυναμικό περιβάλλον μετά από ΕΑΑ. Η μεθοδολογία λαμβάνει υπόψη τον παράγοντα που καθορίζει σε μεγάλο βαθμό τις μετεγχειρητικές αιμοδυναμικές συνθήκες δηλαδή τη θέση των μοσχευμάτων στο σάκο του ανευρύσματος. Τέλος, στο Κεφάλαιο 4, αναλύουμε την αιμοδυναμική απόδοση δύο (2) μοσχευμάτων με ιδιαίτερο σχεδιασμό, του AFX που εκμεταλλεύεται την εγγενή αορτική διακλάδωση για να επιτύχει τη σταθεροποίηση και του Nellix που η λειτουργία του βασίζεται στην καινοτόμα

ενδαγγειακή τεχνολογία στεγανοποίησης ανευρυσμάτων (EVAS).

Οι υπολογιστικές προσομοιώσεις θεωρούνται ο τρίτος πυλώνας της έρευνας μεταξύ θεωρίας και πειράματος. Στο πεδίο της αγγειοχειρουργικής οι προσομοιώσεις δεν έχουν εισαχθεί ακόμα στην κλινική πράξη. Ωστόσο, πολλές κλινικές και βιομηχανικές εφαρμογές των υπολογιστικών προσομοιώσεων αναμένεται να είναι διαθέσιμες για διευρυμένη χρήση στο εγγύς μέλλον.

# NUMERICAL SIMULATIONS OF BLOOD FLOW EFFECTS UNDER THE PRESENCE OF ABDOMINAL AORTIC ANEURYSM

ANASTASIOS A. RAPTIS

## ABSTRACT

Abdominal aortic aneurysms (AAAs) are defined as a localized dilatation of the abdominal aorta featuring diameter at least 50% larger than the normal one. AAAs usually remain asymptomatic until the occurrence of a possibly catastrophic complication, i.e. the rupture. Endovascular aneurysm repair (EVAR) offers a reliable treatment for the disease by excluding the aneurysmal sac and redirecting blood flow through an endovascularly deployed stent-graft system.

Computational fluid dynamics (CFD) is a scientific field involved actively in the study of blood flow throughout the circulatory system. The numerical simulations of blood flow have attracted the interest of the medical community due to their non-invasive character, relatively low resource demands (compared to experiments), their flexibility and the quantity of high-resolution flow analytics that are capable of providing. Recent technological advancements have enabled the combination of CFD with medical imaging data, extending the applicability of CFD to patient-specific vascular models. Researchers are using CFD to unravel possible implications of hemodynamic flow in the pathogenesis, evolvement and rupture of AAAs. The applications of CFD are not limited to physiological or pathological blood flow but can be employed in the context of EVAR as well.

The aim of the current thesis was to explore the capabilities of numerical simulations and set up applications in physiological, preoperative and postoperative AAA cases. Chapter 1 introduces an alternative modeling of intraluminal thrombus (ILT) which is apparent in most AAAs and has a crucial role in their growth. Specifically, ILT is modeled as a porous medium with gradually smaller permeability following histological analyses of evolving ILT structures. The differential equations that describe the interaction of pathological blood flow with a growing ILT are discretized with the Finite Element method and solved by an in-house numerical code in an AAA model. The analysis gives an estimate of the ILT effects

on the flow conditions in AAAs that is in agreement with the biomechanical factors that according to the literature promote ILT initiation and growth.

The literature states that the percentage of post-EVAR complications is variable among the commercial endografts. However there are only a few clinical, computational or experimental studies, providing hemodynamic data in an endograft-specific manner. Additionally, it is known that the implantation of an endograft alters hemodynamics with possible adverse effects on the functionality of the device itself, but there is not a consistent methodology to calculate the blood flow variations specifically. Chapters 2,3 and 4 are attempting to answer open questions regarding the hemodynamic efficiency of EVAR and unravel the hemodynamic profile of various commercial endografts using advanced dynamic three-dimensional numerical simulations coupled with patient-specific medical data. The methodology involves: 1) the collection of suitable medical cases, 2) reconstruction of computed tomography data to acquire the geometrical representation of patient-specific AAAs or endograft structures, 3) generation of numerical grids to enable capturing high-resolution hemodynamic analytics, 4) performance of numerical simulations using CFD, 5) post-processing of the results focusing on regions of interest within the models, 6) visualization of hemodynamic properties and patterns and 7) statistical analysis to determine the significance of the flow variations.

EVAR has favorable short-term outcomes and proven clinical efficiency but it has not been studied adequately if blood flow completely restores to physiological levels after the deployment of an endograft. In Chapter 2, we attempted to define the flow variations in healthy and endovascularly repaired infrarenal aortas. In Chapter 3, we applied the developed workflow to test the hypothesis that two (2) endografts with similar designs, Endurant and Excluder, induce similar hemodynamic environments after EVAR. The applied methodology accounts for the determinant factor of postoperative hemodynamics, i.e. the position of the endograft in the aneurysmal sac. Lastly, in Chapter 4, we analyze the hemodynamic performance of two (2) endografts with more diverse designs, AFX that exploits the native aortic bifurcation to achieve fixation and Nellix, whose function is based on the novel endovascular aneurysm sealing technology.

The computational simulations are considered as the third research pylon between theory and experiment. In the field of vascular surgery, simulations have not been yet introduced in clinical practice. However, many clinical and industrial applications of the computational simulations are expected to be available for broader use in the near future.

## REFERENCES


1. Davies AH, Brophy CM, eds. Vascular surgery. Springer Science & Business Media; 2006.

2. Ashton HA, Buxton MJ, Day NE, et al. The Multicentre Aneurysm Screening Study (MASS) into the effect of abdominal aortic aneurysm screening on mortality in men: a randomised controlled trial. The Lancet 2002;360:1531-9.

3. Norman PE, Jamrozik K, Lawrence-Brown MM, et al. Population based randomised controlled trial on impact of screening on mortality from abdominal aortic aneurysm. BMJ 2004;329:1259.

4. Vardulaki KA, Walker NM, Day NE, et al. Quantifying the risks of hypertension, age, sex and smoking in patients with abdominal aortic aneurysm. Brit J Surg 2000;87:195-200.

5. Anjum A, Powell JT. Is the incidence of abdominal aortic aneurysm declining in the 21st century? Mortality and hospital admissions for England & Wales and Scotland. Eur J Vasc Endovasc Surg 2012;43:191-66.

6. Wassef M, Baxter BT, Chisholm RL, et al. Pathogenesis of abdominal aortic aneurysms: a multidisciplinary research program supported by the National Heart, Lung, and Blood Institute. J Vasc Surg 2001;34:730-8.

7. Lederle FA, Johnson GR, Wilson SE, et al. Prevalence and associations of abdominal aortic aneurysm detected through screening. Ann Intern Med 1997;126:441-9.

8. Choke E, Cockerill G, Wilson WR, et al. A review of biological factors implicated in abdominal aortic aneurysm rupture. Eur J Vasc Endovasc Surg 2005;30:227-44.

9. Participants TUSAT. Mortality results for randomised controlled trial of early elective surgery or ultrasonographic surveillance for small abdominal aortic aneurysms. The Lancet 1998;352:1649-55.

10. Parodi JC, Palmaz JC, Barone HD. Transfemoral intraluminal graft implantation for abdominal aortic aneurysms. Ann Vasc Surg 1991;5:491-9.

11. Moore WS. The role of endovascular grafting technique in the treatment of infrarenal abdominal aortic aneurysm. Vascular 1995;3:109-14.

12. Greenhalgh RM, Brown LC, Powell JT, et al. Endovascular versus open repair of abdominal aortic aneurysm. N Engl J Med 2010;362:1863-71.

13. Katz DJ, Stanley JC, Zelenock GB. Operative mortality rates for intact and ruptured abdominal aortic aneurysms in Michigan: an eleven-year statewide experience. J Vasc Surg 1994;19:804-17.

14. Johnston KW. Non-ruptured abdominal aortic aneurysm: six-year follow-up results from the multicenter prospective Canadian aneurysm study. J Vasc Surg 1994;20:163-70.

15. Beard JD, Gaines PA, Loftus I, eds. Vascular and endovascular surgery: companion to specialist surgical practice. Elsevier Health Sciences; 2013.

16. Wolf YG, Fogarty TJ, Olcott CI, et al. Endovascular repair of abdominal aortic aneurysms: eligibility rate and impact on the rate of open repair. J Vasc Surg 2000;32:519-23.

17. Arko FR, Filis KA, Seidel SA, et al. How many patients with infrarenal aneurysms are candidates for endovascular repair? The northern California experience. J Endovasc Ther 2004;11:33-40.

18. Dillavou ED, Muluk SC, Rhee RY, et al. Does hostile neck anatomy preclude successful endovascular aortic aneurysm repair? J Vasc Surg 2003;38:657-63.

19. Toor SM, Sazonov I, Luckraz H, et al. Aortic aneurysms: OSR, EVAR, stent-grafts, migration and endoleak—current state of the art and analysis. In: Franz T, ed. Cardiovascular and cardiac therapeutic devices. Springer Berlin Heidelberg; 2013:63-92.

20. Eckroth-Bernard K, Garvin R, Ryer E. Current status of endovascular devices to treat abdominal aortic aneurysms. Biomed Eng Comput Biol 2013;5:25-32.

21. Simons P, van Overhagen H, Nawijn A, et al. Endovascular aneurysm repair with a bifurcated endovascular graft at a primary referral center: Influence of experience, age, gender, and aneurysm size on suitability. J Vasc Surg 2003;38:758-61.

22. Makaroun MS, Tuchek M, Massop D, et al. One year outcomes of the United States regulatory trial of the Endurant Stent Graft System. J Vasc Surg 2011;54:601-8.

23. Peterson BG, Matsumura JS, Brewster DC, et al. Five-year report of a multicenter controlled clinical trial of open versus endovascular treatment of abdominal aortic aneurysms. J Vasc Surg 2007;45:885-90.

24. Desai M, Eaton-Evans J, Hillery C, et al. AAA stent-grafts: past problems and future prospects. Ann Biomed Eng 2010;38:1259-75.

25. Buck DB, van Herwaarden JA, Schermerhom ML, et al. Endovascular treatment of abdominal aortic aneurysms. Nat Rev Cardiol 2014;11:112-23.

26. Krievins DK, Holden A, Savlovskis J, et al. EVAR using the Nellix sac-anchoring endoprosthesis: treatment of favourable and adverse anatomy. Eur J Vasc Endovasc Surg 2011;42:38-46.

27. Tonnessen BH, Sternbergh WC, Money SR. Mid- and long-term device migration after endovascular abdominal aortic aneurysm repair: a comparison of AneuRx and Zenith endografts. J Vasc Surg 2005;42:392-401.

28. Sternbergh WC, Money SR, Greenberg RK, et al. Influence of endograft oversizing on device migration, endoleak, aneurysm shrinkage, and aortic neck dilation: results from the Zenith Multicenter Trial. J Vasc Surg 2004;39:20-6.

29. Zarins CK, Bloch DA, Crabtree T, et al. Stent graft migration after endovascular aneurysm repair: importance of proximal fixation. J Vasc Surg 2003;38:1264-72.

30. Benharash P, Lee JT, Abilez OJ, et al. Iliac fixation inhibits migration of both suprarenal and infrarenal aortic endografts. J Vasc Surg 2007;45:250-7.

31. Heikkinen MA, Alsac JM, Arko FR, et al. The importance of iliac fixation in prevention of stent graft migration. J Vasc Surg 2006;43:1130-7.

32. Malas MB, Ohki T, Veith FJ, et al. Absence of proximal neck dilatation and graft migration after endovascular aneurysm repair with balloon-expandable stent-based endografts. J Vasc Surg 2005;42:639-44.

33. Drury D, Michaels JA, Jones L, et al. Systematic review of recent evidence for the safety and efficacy of elective endovascular repair in the management of infrarenal abdominal aortic aneurysm. Brit J Surg 2005;92:937-46.

34. Goncalves FB, Rouwet EV, Metz R, et al. Device-specific outcomes after endovascular abdominal aortic aneurysm repair. J Cardiovasc Surg (Torino) 2010;51:515-31.

35. Hobo R, Laheij RJF, Buth J. The influence of aortic cuffs and iliac limb extensions on the outcome of endovascular abdominal aortic aneurysm repair. J Vasc Surg 2007;45:79-85.

36. Kramer SC, Seifarth H, Pamler R, et al. Geometric changes in aortic endografts over a 2-year observation period. J Endovasc Ther 2001;8:34-8.

37. Fransen GAJ, Desgranges P, Laheij RJF, et al. Frequency, predictive factors, and consequences of stent-graft kink following endovascular AAA repair. J Endovasc Ther 2003;10:913-8.

38. Imamura A, Koike Y, Iwaki R, et al. Infrarenal abdominal aortic aneurysm complicated by persistent endotension after endovascular repair: report of a case. Surg Today 2005;35:879-82.

39. Lin PH, Bush RL, Katzman JB, et al. Delayed aortic aneurysm enlargement due to endotension after endovascular abdominal aortic aneurysm repair. J Vasc Surg 2003;38:840-2.

40. Sonesson B, Dias N, Malina M, et al. Intra-aneurysm pressure measurements in successfully excluded abdominal aortic aneurysm after endovascular repair. J Vasc Surg 2003;37:733-8.

41. Dias NV, Ivancev K, Malina M, et al. Intra-aneurysm sac pressure measurements after endovascular aneurysm repair: differences between shrinking, unchanged, and expanding aneurysms with and without endoleaks. J Vasc Surg 2004;39:1229-35.

42. Dias NV, Ivancev K, Malina M, et al. Direct intra-aneurysm sac pressure measurement using tip-pressure sensors: in vivo and in vitro evaluation. J Vasc Surg 2004;40:711-6.

43. Ohki T, Ouriel K, Silveira PG, et al. Initial results of wireless pressure sensing for endovascular aneurysm repair: the APEX trial - acute pressure measurement to confirm aneurysm sac exclusion. J Vasc Surg 2007;45:236-42.

44. Vallabhaneni SR, Gilling-Smith GL, Brennan JA, et al. Can intrasac pressure monitoring reliably predict failure of endovascular aneurysm repair? J Endovasc Ther 2003;10:524-30.

45. Les AS, Shadden SC, Figueroa CA, et al. Quantification of hemodynamics in abdominal aortic aneurysms during rest and exercise using magnetic resonance imaging and computational fluid dynamics. Ann Biomed Eng 2010;38:1288-313.

46. Xenos M, Raptis A. Fluid structure interaction for biomedical applications. J Appl Computat Math 2014;3:1000187.

47. Moireau P, Xiao N, Astorino M, et al. External tissue support and fluid-structure simulation in blood flows. Biomech Model Mechan 2012;11:1-18.

48. Zeinali-Davarani S, Raguin LG, Vorp DA, et al. Identification of in vivo material and geometric parameters of a human aorta: toward patient-specific modeling of abdominal aortic aneurysm. Biomech Model Mechan 2011;10:689-99.

49. Humphrey JD, Holzapfel GA. Mechanics, mechanobiology, and modeling of human abdominal aorta and aneurysms. J Biomech 2012;45:805-14.

50. Humphrey JD, Rajagopal KR. A constrained mixture model for growth and remodeling of soft tissues. Math Mod Meth Appl S 2002;12:407-30.

51. Vorp DA. Biomechanics of abdominal aortic aneurysm. J Biomech 2007;40:1887-902.

52. Geest JPV, Sacks MS, Vorp DA. Age dependency of the biaxial biomechanical behavior of human abdominal aorta. J Biomech Eng 2004;126:815-22.

53. Vande Geest JP, Sacks MS, Vorp DA. The effects of aneurysm on the biaxial mechanical behavior of human abdominal aorta. J Biomech 2006;39:1324-34.

54. Ferruzzi J, Vorp DA, Humphrey JD. On constitutive descriptors of the biaxial mechanical behaviour of human abdominal aorta and aneurysms. J R Soc Interface 2011;8:435-50.

55. Labrosse MR, Beller CJ, Mesana T, et al. Mechanical behavior of human aortas: experiments, material constants and 3-D finite element modeling including residual stress. J Biomech 2009;42:996-1004.

56. Haskett D, Johnson G, Zhou A, et al. Microstructural and biomechanical alterations of the human aorta as a function of age and location. Biomech Model Mechanobiol 2010;9:725-36.

57. Holzapfel GA. Determination of material models for arterial walls from uniaxial extension tests and histological structure. J Theor Biol 2006;238:290-302.

58. Vande Geest JP, Sacks MS, Vorp DA. A planar biaxial constitutive relation for the luminal layer of intra-luminal thrombus in abdominal aortic aneurysms. J Biomech 2006;39:2347-54.

59. Tong J, Cohnert T, Regitnig P, et al. Effects of age on the elastic properties of the intraluminal thrombus and the thrombus-covered wall in abdominal aortic aneurysms: biaxial extension behaviour and material modelling. Eur J Vasc Endovasc Surg 2011;42:207-19.

60. Rodriguez JF, Ruiz C, Doblare M, et al. Mechanical stresses in abdominal aortic aneurysms: influence of diameter, asymmetry, and material anisotropy. J Biomech Eng 2008;130:021023.

61. Li ZY, Jean U, Tang TY, et al. Impact of calcification and intraluminal thrombus on the computed wall stresses of abdominal aortic aneurysm. J Vasc Surg 2008;47:928-35.

62. Gasser TC, Auer M, Labruto F, et al. Biomechanical rupture risk assessment of abdominal aortic aneurysms: model complexity versus predictability of finite element simulations. Eur J Vasc Endovasc Surg 2010;40:176-85.

63. Georgakarakos E, Ioannou CV, Kamarianakis Y, et al. The role of geometric parameters in the prediction of abdominal aortic aneurysm wall stress. Eur J Vasc Endovasc Surg 2010;39:42-8.

64. Maier A, Gee MW, Reeps C, et al. A comparison of diameter, wall stress, and rupture potential index for abdominal aortic aneurysm rupture risk prediction. Ann Biomed Eng;38:3124-34.

65. Maier A, Gee MW, Reeps C, et al. Impact of calcifications on patient-specific wall stress analysis of abdominal aortic aneurysms. Biomech Model Mechan 2010;9:511-21.

66. Raghavan ML, Vorp DA. Toward a biomechanical tool to evaluate rupture potential of abdominal aortic aneurysm: identification of a finite strain constitutive model and evaluation of its applicability. J Biomech 2000;33:475-82.

67. Raghavan ML, Kratzberg J, de Tolosa EM, et al. Regional distribution of wall thickness and failure properties of human abdominal aortic aneurysm. J Biomech 2006;39:3010-6.

68. Wilson JS, Baek S, Humphrey JD. Importance of initial aortic properties on the evolving regional anisotropy, stiffness and wall thickness of human abdominal aortic aneurysms. J R Soc Interface 2012;9:2047-58.

69. Lasheras JC. The biomechanics of arterial aneurysms. Ann Rev Fluid Mech 2007;39:293-319.

70. Humphrey JD, Taylor CA. Intracranial and abdominal aortic aneurysms: similarities, differences, and need for a new class of computational models. Annu Rev Biomed Eng 2008;10:221-46.

71. Finol EA, Keyhani K, Amon CH. The effect of asymmetry in abdominal aortic aneurysms under physiologically realistic pulsatile flow conditions. J Biomech Eng 2003;125:207-17.

72. Deplano V, Knapp Y, Bertrand E, et al. Flow behaviour in an asymmetric compliant experimental model for abdominal aortic aneurysm. J Biomech 2007;40:2406-13.

73. Peattie RA, Riehle TJ, Bluth EI. Pulsatile flow in fusiform models of abdominal aortic aneurysms: Flow fields, velocity patterns and flow-induced wall stresses. J Biomech Eng-Trans ASME 2004;126:438-46.

74. Salsac AV, Sparks SR, Lasheras JC. Hemodynamic changes occurring during the progressive enlargement of abdominal aortic aneurysms. Ann Vasc Surg 2004;18:14-21.

75. Egelhoff CJ, Budwig RS, Elger DF, et al. Model studies of the flow in abdominal aortic aneurysms during resting and exercise conditions. J Biomech 1999;32:1319-29.

76. Finol EA, Amon CH. Flow dynamics in anatomical models of abdominal aortic aneurysms: computational analysis of pulsatile flow. Acta Cient Venez 2003;54:43-9.

77. Xenos M, Bluestein D. Biomechanical aspects of abdominal aortic aneurysm (AAA) and its risk of rupture: fluid structure interaction (FSI) studies. In: McGloughlin T, ed. Biomechanics and mechanobiology of aneurysms. Springer Berlin Heidelberg; 2011:181-220.

78. Xenos M, Labropoulos N, Rambhia S, et al. Progression of abdominal aortic aneurysm towards rupture: refining clinical risk assessment using a fully coupled fluid-structure interaction method. Ann Biomed Eng 2015;43:139-53.

79. Biasetti J, Gasser TC, Auer M, et al. Hemodynamics of the normal aorta compared to fusiform and saccular abdominal aortic aneurysms with emphasis on a potential thrombus formation mechanism. Ann Biomed Eng 2010;38:380-90.

80. Biasetti J, Hussain F, Gasser TC. Blood flow and coherent vortices in the normal and aneurysmatic aortas: a fluid dynamical approach to intraluminal thrombus formation. J R Soc Interface 2011;8:1449-61.

81. Bluestein D, Dumont K, De Beule M, et al. Intraluminal thrombus and risk of rupture in patient specific abdominal aortic aneurysm - FSI modelling. Comput Methods Biomec 2008;12:73-81.

82. Stamatopoulos C, Mathioulakis DS, Papaharilaou Y, et al. Experimental unsteady flow study in a patient-specific abdominal aortic aneurysm model. Exp Fluids 2011;50:1695-709.

83. Kung EO, Les AS, Medina F, et al. In vitro validation of finite-element model of AAA hemodynamics incorporating realistic outlet boundary conditions. J Biomech Eng 2011;133:041003.

84. Suh GY, Les AS, Tenforde AS, et al. Quantification of particle residence time in abdominal aortic aneurysms using magnetic resonance imaging and computational fluid dynamics. Ann Biomed Eng 2011;39:864-83.

85. Suh GY, Les AS, Tenforde AS, et al. Hemodynamic changes quantified in abdominal aortic aneurysms with increasing exercise intensity using MR exercise imaging and image-based computational fluid dynamics. Ann Biomed Eng 2011;39:2186-202.

86. Chung B, Cebral JR. CFD for evaluation and treatment planning of aneurysms: review of proposed clinical uses and their challenges. Ann Biomed Eng 2015;43:122-38.

87. Zarins CK, Taylor CA. Endovascular device design in the future: transformation from trial and error to computational design. J Endovasc Ther 2009;16:12-21.

88. Georgakarakos E, Georgiadis GS, Xenakis A, et al. Application of bioengineering modalities in vascular research: evaluating the clinical gain. Vasc Endovasc Surg 2012;46:101-8.

89. Walsh PW, Chin-Quee S, Moore JE. Flow changes in the aorta associated with the deployment of a AAA stent graft. Med Eng Phys 2003;25:299-307.

90. Georgakarakos E, Raptis A, Schoretsanitis N, et al. Studying the interaction of stent-grafts and treated abdominal aortic aneurysms: time to move caudally! J Endovasc Ther 2015;22:413-20.

91. Kwon ST, Rectenwald JE, Baek S. Intrasac pressure changes and vascular remodeling after endovascular repair of abdominal aortic aneurysms: review and biomechanical model simulation. J Biomech Eng 2011;133:011011.

92. Figueroa CA, Taylor CA, Yeh V, et al. Preliminary 3D computational analysis of the relationship between aortic displacement force and direction of endograft movement. J Vasc Surg 2010;51:1488-97.

93. Molony DS, Kavanagh EG, Madhavan P, et al. A computational study of the magnitude and direction of migration forces in patient-specific abdominal aortic aneurysm stent-grafts. Eur J Vasc Endovasc Surg 2010;40:332-9.

94. Polanczyk A, Podyma M, Stefanczyk L, et al. A 3D model of thrombus formation in a stent-graft after implantation in the abdominal aorta. J Biomech 2015;48:425-31.

95. Vardoulis O, Coppens E, Martin B, et al. Impact of aortic grafts on arterial pressure: a computational fluid dynamics study. Eur J Vasc Endovasc Surg 2011;42:704-10.

96. Morris L, Stefanov F, McGloughlin T. Stent graft performance in the treatment of abdominal aortic aneurysms: the influence of compliance and geometry. J Biomech 2013;46:383-95.

97. Molony DS, Callanan A, Morris LG, et al. Geometrical enhancements for abdominal aortic stent-grafts. J Endovasc Ther 2008;15:518-29.

98. Kleinstreuer C, Li Z, Basciano CA, et al. Computational mechanics of nitinol stent grafts. J Biomech 2008;41:2370-8.

99. Kaladji A, Dumenil A, Castro M, et al. Prediction of deformations during endovascular aortic aneurysm repair using finite element simulation. Comput Med Imaging Graph 2013;37:142-9.

100. Anton R, Chen CY, Hung MY, et al. Experimental and computational investigation of the patient-specific abdominal aortic aneurysm pressure field. Comput Methods Biomec 2015;18:981-92.

101. Kung EO, Les AS, Figueroa AC, et al. In vitro validation of finite element analysis of blood flow in deformable models. Ann Biomed Eng 2011;39:1947-60.

102. Propper BW, Abularrage CJ. Long-term safety and efficacy of endovascular abdominal aortic aneurysm repair. Vasc Health Risk Manag, 2013;9:135-41.

103. Van Marrewijk CJ, Leurs LJ, Vallabhaneni SR, et al. Risk-adjusted outcome analysis of endovascular abdominal aortic aneurysm repair in a large population: how do stent-grafts compare? J Endovasc Ther 2005;12:417-29.

104. Hans SS, Jareunpoon O, Balasubramaniam M, et al. Size and location of thrombus in intact and ruptured abdominal aortic aneurysms. J Vasc Surg 2005;41:584-8.

105. Speelman L, Schurink GW, Bosboom EM, et al. The mechanical role of thrombus on the growth rate of an abdominal aortic aneurysm. J Vasc Surg 2010;51:19-26.

106. Wufsus AR, Macera NE, Neeves KB. The hydraulic permeability of blood clots as a function of fibrin and platelet density. Biophys J 2013;104:1812-23.

107. Xu ZL, Kamocka M, Alber M, et al. Computational approaches to studying thrombus development. Arterioscl Throm Vas 2011;31:500-5.

108. Leiderman K, Fogelson AL. Grow with the flow: a spatial-temporal model of platelet deposition and blood coagulation under flow. Math Med Biol 2011;28:47-84.

109. Di Martino E, Mantero S, Inzoli F, et al. Biomechanics of abdominal aortic aneurysm in the presence of endoluminal thrombus: experimental characterisation and structural static computational analysis. Eur J Vasc Endovasc Surg 1998;15:290-9.

110. Wang DH, Makaroun M, Webster MW, et al. Mechanical properties and microstructure of intraluminal thrombus from abdominal aortic aneurysm. J Biomech Eng 2001;123:536-9.

111. Vande Geest JP, Sacks MS, Vorp DA. Age dependency of the biaxial biomechanical behavior of human abdominal aorta. J Biomech Eng 2004;126:815-22.

112. Polzer S, Gasser TC, Markert B, et al. Impact of poroelasticity of intraluminal thrombus on wall stress of abdominal aortic aneurysms. Biomed Eng Online 2012;11:1-13.

113. Toungara M, Geindreau C. Influence of a poro-mechanical modeling of the intra-luminal thrombus and the anisotropy of the arterial wall on the prediction of the abdominal aortic aneurysm rupture. Cardiovasc Eng Technol 2013;4:192-208.

114. Ayyalasomayajula A, Vande Geest JP, Simon BR. Porohyperelastic finite element modeling of abdominal aortic aneurysms. J Biomech Eng-Trans ASME 2010;132:104502.

115. Vande Geest JP, Simon BR, Rigby PH, et al. Coupled porohyperelastic mass transport (PHEXPT) finite element models for soft tissues using ABAQUS. J Biomech Eng-Trans ASME 2011;133:044502.

116. Adolph R, Vorp DA, Steed DL, et al. Cellular content and permeability of intraluminal thrombus in abdominal aortic aneurysm. J Vasc Surg 1997;25:916-26.

117. Raptis A, Xenos M, Dimas S, et al. Effect of macroscale formation of intraluminal thrombus on blood flow in abdominal aortic aneurysms. Comput Methods Biomec 2016;19:84-92.

118. Wilson JS, Virag L, Di Achille P, et al. Biochemomechanics of intraluminal thrombus in abdominal aortic aneurysms. J Biomech Eng-Trans ASME 2013;135:021011.

119. Xu ZL, Christley S, Lioi J, et al. Multiscale model of fibrin accumulation on the blood clot surface and platelet dynamics. In: Asthagiri AR, Arkin AP, eds. Computational methods in cell biology. Academic Press; 2012:367-88.

120. Nield D, Bejan A. Convection in porous media. 2nd ed. Springer Science & Business Media; 1999.

121. Nield DA. Modelling fluid flow and heat transfer in a saturated porous medium. J Appl Math Decis Sci 2000;4:165-73.

122. Fletcher CAJ. Computational techniques for fluid dynamics. 2nd ed. Springer-Verlag; 1991.

123. Raptis A, Xenos M, Tzirtzilakis E, et al. Finite element analysis of magnetohydrodynamic effects on blood flow in an aneurysmal geometry. Phys Fluids 2014;26:101901.

124. Warsi UAZ. Mathematics of space and surface grid generation. In: Thompson FJ, Bahrat S, Weatherill N, eds. Handbook of grid generation. N.W. Boca Raton Florida: CRC Press LLC; 1999:2-1 - 2-45.

125. Somayaji MR, Xenos M, Zhang L, et al. Systematic design of drug delivery therapies. Comput Chem Eng 2008;32:89-98.

126. Taylor C, Hughes TG. Finite element programming of the Navier-Stokes equations. 1st ed. Pineridge Press Ltd.; 1981.

127. Finol EA, Amon CH. Blood flow in abdominal aortic aneurysms: pulsatile flow hemodynamics. J Biomech Eng 2001;123:474-84.

128. Xenos M, Rambhia SH, Alemu Y, et al. Patient-based abdominal aortic aneurysm rupture risk prediction with fluid structure interaction modeling. Ann Biomed Eng 2010;38:3323-37.

129. Ashton JH, Vande Geest JP, Simon BR, et al. Compressive mechanical properties of the intraluminal thrombus in abdominal aortic aneurysms and fibrin-based thrombus mimics. J Biomech 2009;42:197-201.

130. Roy D, Kauffmann C, Delorme S, et al. A literature review of the numerical analysis of abdominal aortic aneurysms treated with endovascular stent grafts. Comput Math Methods Med 2012.

131. O'Rourke MJ, McCullough JP, Kelly S. An investigation of the relationship between hemodynamics and thrombus deposition within patient-specific models of abdominal aortic aneurysm. P I Mech Eng H 2012;226:548-64.

132. Arzani A, Shadden SC. Characterization of the transport topology in patient-specific abdominal aortic aneurysm models. Phys Fluids 2012;24:081901.

133. Basciano C, Kleinstreuer C, Hyun S, et al. A relation between near-wall particle-hemodynamics and onset of thrombus formation in abdominal aortic aneurysms. Ann Biomed Eng 2011;39:2010-26.

134. Thubrikar M. Vascular mechanics and pathology. 1st ed. Springer Science & Business Media; 2007.

135. Schurink GW, van Baalen JM, Visser MJ, et al. Thrombus within an aortic aneurysm does not reduce pressure on the aneurysmal wall. J Vasc Surg 2000;31:501-6.

136. Hans SS, Jareunpoon O, Huang R, et al. Relationship of residual intraluminal to intrathrombotic pressure in a closed aneurysmal sac. J Vasc Surg 2003;37:949-53.

137. Li ZY, Sadat U, Jean U, et al. Association between aneurysm shoulder stress and abdominal aortic aneurysm expansion a longitudinal follow-up study. Circulation 2010;122:1815-22.

138. Wilson JS, Baek S, Humphrey JD. Parametric study of effects of collagen turnover on the natural history of abdominal aortic aneurysms. P Roy Soc A-Math Phy 2013;469:20120556.

139. Chong CK, How TV. Flow patterns in an endovascular stent-graft for abdominal aortic aneurysm repair. J Biomech 2004;37:89-97.

140. Corbett TJ, Callanan A, Morris LG, et al. A review of the in vivo and in vitro biomechanical behavior and performance of postoperative abdominal aortic aneurysms and implanted stent-grafts. J Endovasc Ther 2008;15:468-84.

141. Raptis A, Xenos M, Peroulis M, et al. The impact of endovascular repair of abdominal aortic aneurysms on hemodynamic flow: a comparison of the preoperative and postoperative biomechanical properties. Hellenic Vasc Surg 2014:29-36.

142. Kandail H, Hamady M, Xu XY. Patient-specific analysis of displacement forces acting on fenestrated stent grafts for endovascular aneurysm repair. J Biomech 2014;47:3546-54.

143. Olufsen MS, Peskin CS, Kim WY, et al. Numerical simulation and experimental validation of blood flow in arteries with structured-tree outflow conditions. Ann Biomed Eng 2000;28:1281-99.

144. Xenos M, Karakitsos D, Labropoulos N, et al. Comparative study of flow in right-sided and left-sided aortas: numerical simulations in patient-based models. Comput Methods Biomec 2015;18:414-25.

145. Morbiducci U, Ponzini R, Rizzo G, et al. In vivo quantification of helical blood flow in human aorta by time-resolved three-dimensional cine phase contrast magnetic resonance imaging. Ann Biomed Eng 2009;37:516-31.

146. Morbiducci U, Ponzini R, Rizzo G, et al. Mechanistic insight into the physiological relevance of helical blood flow in the human aorta: an in vivo study. Biomech Model Mechan 2011;10:339-55.

147. Frauenfelder T, Lotfey M, Boehm T, et al. Computational fluid dynamics: hemodynamic changes in abdominal aortic aneurysm after stent-graft implantation. Cardiovasc Intervent Radiol 2006;29:613-23.

148. Papaioannou TG, Stefanadis C. Vascular wall shear stress: basic principles and methods. Hellenic J Cardiol 2005;46:9-15.

149. Boyd AJ, Kuhn DC, Lozowy RJ, et al. Low wall shear stress predominates at sites of abdominal aortic aneurysm rupture. J Vasc Surg 2015;63:1613-9.

150. Liu X, Sun A, Fan Y, et al. Physiological significance of helical flow in the arterial system and its potential clinical applications. Ann Biomed Eng 2015;43:3-15.

151. Pratesi C, Piffaretti G, Pratesi G, et al. ITalian Excluder Registry and results of Gore Excluder endograft for the treatment of elective infrarenal abdominal aortic aneurysms. J Vasc Surg 2014;59:52-7.

152. Maleux G, Claes H, Van Holsbeeck A, et al. Ten years of experience with the GORE EXCLUDER(R) stent-graft for the treatment of aortic and iliac aneurysms: outcomes from a single center study. Cardiovasc Intervent Radiol 2012;35:498-507.

153. Bockler D, Riambau V, Fitridge R, et al. Worldwide experience with the Endurant Stent-graft System: review of the literature. J Cardiovasc Surg (Torino) 2011;52:669-81.

154. Biasetti J, Spazzini P, Hedin U, et al. Synergy between shear-induced migration and secondary flows on red blood cells transport in arteries: considerations on oxygen transport. J R Soc Interface 2014;11:20140403.

155. Stefanov F, McGloughlin T, Delassus P, et al. Hemodynamic variations due to spiral blood flow through four patient-specific bifurcated stent graft configurations for the treatment of abdominal aortic aneurysms. Int J Numer Meth Biomed Eng 2013;29:179-96.

156. Oliveira NFG, Goncalves FMB, Hoeks SE, et al. Clinical outcome and morphologic determinants of mural thrombus in abdominal aortic endografts. J Vasc Surg 2015;61:1391-8.

157. Figueroa CA, Taylor CA, Yeh V, et al. Effect of curvature on displacement forces acting on aortic endografts: a 3-dimensional computational analysis. J Endovasc Ther 2009;16:284-94.

158. Welborn MB, McDaniel HB, Johnson RC, et al. Clinical outcome of an extended proximal seal zone with the AFX endovascular aortic aneurysm system. J Vasc Surg 2014;60:876-83.

159. Bartoli MA, Thevenin B, Sarlon G, et al. Secondary procedures after infrarenal abdominal aortic aneurysms endovascular repair with second-generation endografts. Ann Vasc Surg 2012;26:166-74.